Mineral chemistry of magnetite from magnetite-apatite mineralization and their host rocks: Examples from Kiruna, Sweden and El Laco, Chile

Shannon G. Broughm

A thesis submitted to the Department of Earth Sciences in partial fulfillment of the requirements for the degree of Master of Science.

Memorial University of Newfoundland

Abstract

Magnetite-apatite deposits, sometimes referred to as Kiruna-type deposits, are major producers of iron ore that dominantly consist of the mineral magnetite (nominally $[Fe^{2+}Fe^{3+}{}_2]O_4$). It remains unclear whether magnetite-apatite deposits are of hydrothermal or magmatic origin, or a combination of those two processes, and this has been a subject of debate for over a century. Magnetite is sensitive to the physicochemical conditions in which it crystallizes (such as element availability, temperature, pH, fO_2, and fS_2) and may contain distinct trace element concentrations depending on the growing environment. These properties make magnetite potentially a useful geochemical indicator for understanding the genesis of magnetite-apatite mineralization.

The samples used in this study are from precisely known geographic locations and geologic environments in the world class districts of Kiruna and the Atacama Desert and their associated, sometimes hydrothermally altered, host rocks. Trace element analyses results of magnetite from the Kiruna area in the Norrbotten region of northern Sweden, and the El Laco and Láscar volcanoes in the Atacama Desert of northeastern Chile, were evaluated using mineral deposit-type and magmatic vs. hydrothermally derived magnetite discrimination diagrams.

The objectives of this study are to critically evaluate the practical use and limitations of these discrimination diagrams with the goal of determining if the trace element chemistry of magnetite can be used to resolve if magnetite-apatite deposits form in a hydrothermal or magmatic environment, or a combination of those two processes.

The results of this study reveal that the magnetite from Kiruna have relatively low trace element concentrations and are homogeneous. There is little chemical variation

between the ore, the hydrothermally altered host rocks, and related igneous intrusives from Kiruna, which may be a result of pervasive post-formation alteration due to extensive metasomatism and later greenschist facies metamorphism that has affected the region. Distinct chemical variations do exist, however, in the magnetite at El Laco between magnetite from the Laco Sur magnetite-apatite ore and host andesite, and a dacite sample from the nearby Láscar volcano. Accessory magnetite from the host andesite and Láscar dacite volcanic rocks have relatively high trace element concentrations, typical of magnetite crystallizing from a melt and; with overall trace element concentrations higher than the magnetite-apatite ore, or the Kiruna magnetites. The Laco Sur ore magnetite has low overall low trace element concentrations and displays growth zoning defined by incompatible elements (Si, Ca), compatible elements (Mg, Al, and Mn), LILE (Sr) and HFSE (Y, Nb, Ce and Th) with each element displaying similar geochemical trends. While the trace element concentrations of the ore magnetite at Laco Sur has cores that are enriched in incompatible element; similar to magnetite that is known to have formed from hydrothermal fluids (such as magnetite from iron-rich skarns), the trace element zoning patterns suggests that the magnetite crystallized from a volatile-rich iron-oxide melt.

Acknowledgments

I would like to thank those who funded this research, the Natural Sciences and Engineering Research Council of Canada (NSERC) discovery grant to John M. Hanchar. The contribution of Fernando Tornos has been funded by the project SEIDI 2014 CGL2014-55949-R.

Thanks to Luossavaara-Kiirunavaara Aktiebolag (LKAB) and Compañía Minera del Pacífico (CMP) for help in logistics, and permission to sample and granting access to the mine sites.

I want to express my gratitude to my supervisor John M. Hanchar for giving me the opportunity to pursue this research and for providing valued feedback throughout.

A special thanks goes to Fernando Tornos and Anne Westhues who both provided me with critical feedback throughout my research, especially during the compilation of my manuscript. Thank you to Steve Piercey for being on my committee during this project, allowing me to use the petrographic microscope in his research lab, and for having good taste in music.

Thanks to Samuel Attersley for his magnetite data from El Laco, which made this study vastly more interesting.

Many thanks to all my friends in Newfoundland (especially my office mate and best friend Sarah Turner) who provided me with emotional support, and food, during trying times while pursuing my M.Sc. degree.

Thank you to my family for believing in my success and financial contributions when ends could not be met.

Table of Contents

List of Figures

List of Appendices

List of Abbreviations

Mag	Magnetite
fO_2	Oxygen fugacity
fS_2	Sulfur fugacity
CVZ	Central Volcanic Zone
EPMA	Electron probe microanalyzer
LA-ICPMS	Laser ablation-inductively coupled plasma mass spectrometer
LOD	Level of detection
SEM	Scanning electron microscope
BSE	Back-scattered electron imaging
EDS	Energy dispersive spectroscopy

Chapter 1: Introduction to the Research

Introduction

Genetic models for the formation of Kiruna-type magnetite-apatite deposits have been debated for over a century (e.g., Geijer, 1910; Geijer, 1919; Parák, 1975; Frietsch, 1978; Nyström and Henríquez, 1994; Bergman et al., 2001). The relationship between the host rock emplacement to their subsequent hydrothermal alteration and mineralization to form magnetite-apatite deposits remains controversial (Hitzman et al., 1992; Williams et al., 2005; Groves et al., 2010). Additional research is necessary in order to obtain a better understanding of the processes involved in forming magnetite-apatite deposits (Groves et al., 2010).

In a broad sense, there are two genetic models to describe how magnetite-apatite deposits formed in favor today, with a third model that involves a combination of the first two models: 1) Originating from immiscible iron-rich melts that separated from a silicate melt and were emplaced at subvolcanic levels or erupted and cooled at the surface (e.g., Henríquez and Martin, 1978; Nyström and Henríquez, 1994; Naslund et al., 2002; Nyström et al., 2008; Martinsson, 2016); 2) Metasomatic replacement of the host rocks by hydrothermal fluids (e.g., Hitzman et al., 1992; Rhodes and Oreskes, 1999; Sillitoe and Burrows, 2002; Edfelt et al., 2005; Groves et al., 2010; Valley et al., 2011; Dare et al., 2015; Westhues et al., in press); and 3) a magmatic-hydrothermal combination of these two models (e.g., Knipping et al., 2015; Tornos et al., 2016). A sedimentary-exhalative origin was suggested by Parák (1975) but was not widely accepted (Frietsch, 1978; Nyström et al., 2008).

In this study, the trace element chemistry of magnetite was examined in situ from world-class magnetite-apatite localities of Kiruna in Sweden and El Laco of the Atacama Desert in Chile. The samples used in this study are from precisely known geographic locations and geologic environments. In Kiruna, magnetite grains were analyzed from the magnetite-apatite mineralization, footwall, hanging wall and spatially related felsic intrusive rocks. At El Laco, magnetite grains from the magnetite-apatite mineralization and host andesite rocks were analyzed. Magnetite from the volcanic rocks of the Láscar volcano nearby to El Laco, which does not have any known occurrences of magnetite-apatite mineralization, was also analyzed to compare with the andesite magnetite at El Laco. The magnetite trace element analyses results were evaluated using mineral deposit-type and magmatic vs. hydrothermally derived magnetite discrimination diagrams.

Research Statement

The present study was undertaken to bring insight into the controversial origin of magnetite-apatite deposits through interpretation of the geochemical signatures of magnetite. For this type of study, magnetite (nominally $[Fe^{2+}Fe^{3+}{}_2]O_4$) was investigated because it has the following characteristics: 1) widespread occurrence in relevant deposit types and host rock assemblages; 2) can accommodate a broad range of minor and trace elements in its structure; and 3) is relatively resistant to weathering (i.e., mechanical and chemical surface processes), which potentially makes it an ideal provenance indicator for mineral exploration and useful for genetic studies of ore deposits (Lindsley, 1991; Grigsby, 1990; Dupuis and Beaudoin, 2011; Dare et al., 2014; Nadoll et al., 2014).

Magnetite is a member of the spinel group of minerals, which have a cubic close-packing structure with tetrahedral (A) and octahedral (B) sites in coordination with oxygen anions. The magnetite crystal has the stoichiometry AB_2O_4, where A= Fe^{2+} and B= Fe^{3+} (Buddington and Lindsley, 1964; Lindsley, 1976). A variety of lithophile and siderophile elements with similar ionic radii to Fe^{2+} and Fe^{3+} substitute into magnetite, though in certain favorable physicochemical conditions chalcophile and other elements can also be incorporated (Nadoll et al., 2014).

Empirical discrimination plots have been proposed illustrating that magnetite from magnetite-apatite deposits contain distinct trace element chemical compositions compared to magnetite from other deposit types, such as banded iron formations (BIF), IOCG, porphyry Cu and Fe-Ti-V deposits (e.g., Loberg & Horndahl, 1983; Dupuis and Beaudoin, 2011; Dare et al., 2014), as well as magnetite from unaltered volcanic rocks at El Laco (e.g., Dare et al., 2015). Dare et al. (2015) proposed that the distinct trace elements signatures of the magnetite from the magnetite-apatite ores at El Laco are explained by replacement of the andesite host rocks through precipitation of magnetite from Fe-rich fluids. The present study uses newly obtained data for magnetite trace element geochemistry to assess the general practical use and limitations of the proposed empirical magnetite discrimination diagrams; and whether they can be utilized in interpreting the mineralization style and ore genesis of magnetite-apatite deposits.

The magnetite trace element chemistry was determined through in situ spot analysis using a laser ablation inductively coupled mass spectrometer (LA-ICPMS). The LA-ICPMS data were reduced with Iolite software (Paton et al., 2011) using Fe (wt%)

concentrations that were determined by an electron probe micro-analyzer (EPMA) from the same areas of the grains.

Research Questions

Questions we address in this study include: 1) how useful are empirical magnetite discrimination diagrams in determining the type of mineral deposit of the magnetite?; 2) how useful are empirical magnetite discrimination diagrams in determining whether magnetite has formed magmatically or hydrothermally?; and 3) Can the trace element chemistry and textures of magnetite help shed light on the long-debated subject of how magnetite-apatite deposits form?

Project Overview

The findings from this research have been presented as a manuscript found in Chapter 2 of this thesis. The manuscript has been submitted to the journal *Mineralium Deposita*.

Appendix I contains the complete sample list with details regarding GPS coordinates, underground level (Kiirunavaara mine), Elevation (El Laco volcano), rock type, mineralogy and textures of the magnetite. The location of these samples are shown in Figure 1 of Chapter 2.

Appendix II contains summarized methods for EPMA and LA-ICPMS analysis of the magnetite.

Appendix III contains the average (mean) results for EPMA and LA-ICPMS analysis.

Appendix VI contains individual EPMA analysis for iron concentrations for each sample. EPMA spot locations can be found in Appendix VI.

Appendix V contains LA-ICPMS data for each individual analysis. The Fe concentrations are presented here as the average of three or less EPMA analysis points in the vicinity of the corresponding LA-ICPMS spots; these values are also presented in Appendix IV. LA-ICPMS spot locations can be found in Appendix VI.

Appendix VI shows BSE images of the magnetite grains that were analyzed with the LA-ICPMS and EPMA spot locations for each sample.

Appendix VII contains LA-ICPMS and EPMA data for the Mudtank, Balmat, and Bushveld magnetite that were analyzed as secondary standards. Exact spot locations are not provided, as these magnetite grains were not analyzed in situ.

Appendix VIII contains LA-ICPMS spot analysis results for the primary standard reference material BCR-2G glass during the Kiruna and El Laco analysis runs and the Memorial University of Newfoundland long-term average for comparison. See Figure 2 in Chapter 2 for visual results of this data.

Co-authorship Statement

Each step of this thesis (i.e., the research proposal, practical aspects of the research, data analysis, and initial preparation of the manuscript) was primarily done by the author of this thesis, Shannon G. Broughm. The manuscript preparation, in Chapter 2, into its submitted form was a collaborative effort with the co-authors of the manuscript, however, the author of this thesis wrote the original draft of the manuscript.

References

Bergman S, Kubler L and Martinsson O (2001) Description of regional geological and geophysical maps of northern Norrbotten County (east of the Caledonian Orogen). Sveriges Geologiska Undersokning 56:110

Buddington AF and Lindsley DG (1964) Iron-titanium oxide minerals and synthetic equivalents. J Petrol 5(2):310-357

Dare SAS, Barnes S-J, Beaudoin G, Méric J, Boutroy E and Potvin-Doucet C (2014) Trace elements in magnetite as petrogenetic indicators. Miner Deposita 49:785-796

Dare SAS, Barnes S-J and Beaudoin G (2015) Did the massive magnetite "lava flows" of El Laco (Chile) form by magmatic or hydrothermal processes? New contraints from magnetite composition by LA-ICPMS. Miner Deposita 50:607-617

Dupuis C and Beaudoin G (2011) Discriminant diagrams for iron oxide trace element fingerprinting of mineral deposit types. Miner Deposita 46:319-335.

Edfelt A, Armstrong RN, Smith M and Martinsson O (2005) Alteration paragenesis and mineral chemistry of the Tjarrojakka apatite-rion and Cu (-Au) occurrences, Kiruna area, northern Sweden. Miner Deposita 40:409-434

Frietsch R (1978) On the magmatic origin of iron ores of the Kiruna type. Econ Geol 73:478-485

Geijer P (1910) Igneous rocks and iron ores of Kiirunavaara, Luossavaara and Tuollavaara. Scientific and practical researches in Lapland arranged by the Luossavaara-Kiirunavaara Aktiebolag - Geology of the Kiruna district, 2: Stockholm, p. 278

Geijer P (1919) Recent developments at Kiruna, SGU, C 288, p. 23

Grigsby JD (1990) Detrital magnetite as a provenance indicator. Journal of Sedimentary Petrology 60(6):940-951

Groves DI, Bierlein FP, Meinert LD and Hitzman MW (2010) Iron oxide copper-gold (IOCG) through earths history: implications for origin, lithospheric setting, and distinction from other epigenic iron oxide deposits. Econ Geol 105:641-654

Henríquez F and Martin RF (1978) Crystal growth textures in magnetite flows and feeder dykes, El Laco, Chile, Can Miner 16:581-589

Hitzman MW, Oreskes N and Einaudi MT (1992) Geological Characteristics and Tectonic Setting of Proterozoic Iron-Oxide (Cu-U-Au-Ree) Deposits. Precambrian Research 58:241-287

Knipping JL, Bilenker LD, Simon AC, Reich M, Barra F, Deditius AP, Wälle M, Heinrich CA, Holtz F and Munizaga R (2015) Trace elements in magnetite from massive iron oxide-apatite deposits indicate a combined formation by igneous and magmatic-hydrothermal processes. Geochim Cosmochim Acta 171:15-38

Lindsley DH (1976) The crystal chemistry and structure of oxide minerals as exemplified by the Fe-Ti oxides. In Oxide minerals. Mineralogical Society of America, Short Course Notes 3:L-1 to L-60

Lindsley DH (1991) Oxide minerals: petrologic and magnetic significance. Reviews in Mineralogy, Volume 25, Stony Brook, New York, USA

Martinsson O, Billström K, Broman C, Weihed P and Wanhainen C (2016) Metallogeny of the northern Norrbotten ore province, northern fennoscandian shield with emphasis on IOCG and apatite-iron ore deposits. Ore Geology Reviews. doi: 10.1016/j.oregeorev.2016.02.011

Nadoll P, Angerer T, Mauk JL, French D and Walshe J (2014) The chemistry of hydrothermal magnetite: a review. Ore Geology Reviews 61:1-32

Naslund HR, Henríquez FJ, Nyström JO, Vivallo W and Dobbs F (2002) Magmatic iron ores and associated mineralization: examples from the Chilean High Andes and Coastal Cordillera; in

Porter, T.M. (Ed.), Hydrothermal Iron Oxide Copper-Gold & Related Deposits: A Global Perspective, PGC Publishing, Adelaide, 2:207-226

Nyström JO and Henríquez F (1994) Magmatic features of iron ores of the Kiruna type in Chile and Sweden; ore textures and magnetite geochemistry. Econ Geol 89:820-839

Nyström JO, Billström K, Henríquez F, Fallick AE and Naslund H R (2008) Oxygen isotope composition of magnetite in iron ores of the Kiruna type in Chile and Sweden. Gff 130:177-188

Paton C, Hellstrom J, Paul B, Woodhead J and Hergt J (2011) Iolite: Freeware for the visualisation and processing of mass spectrometric data. Journal of Analytical Atomic Spectrometry 26:2508-2518. doi: 10.1039/c1ja10172b

Parák T (1975) Kiruna iron ores are not 'intrusive-magmatic ores of the Kiruna type'. Econ Geol 70:1242-1258

Rhodes AL and Oreskes N (1999) Oxygen isotope composition of magnetite deposits at El Laco, Chile: evidence of formation from isotopically heavy fluids. Soc of Econ Geol, Spec Pub 7:333-351

Sillitoe RH and Burrows DR (2002) New field evidence bearing on the origin of the el laco magnetite deposit, northern Chile. Econ Geol 97:1101-1109

Tornos F, Velasco F and Hanchar JM (2016) Iron oxide melts, magmatic magnetite and superheated magmatic-hydrothermal systems: the El Laco deposit, Chile. Geology 44:427-430; doi: 10.1130/G37705.1

Valley PM, Hanchar JM, Whitehouse MJ (2011) New insights on the evolution of the Lyon mountain granite and associated Kiruna-type magnetite-apatite deposits, Adirondack Mountains, New York State. Geosphere 7:357-389

Westhues A, Hanchar JM, Whitehouse MJ, Martinsson O (2016) New constraints on the timing of host rock emplacement, hydrothermal alteration and iron oxide apatite mineralization in and around Kiruna, Norrbotten region, northern Sweden. In press in Econ Geol

Williams PJ, Hedenquist JW, Barton MD, Johnson DA, Fontbote L, de Haller A, Mark G, Oliver NHS, Marschik R, Thompson JFH, Goldfarb RJ, Richards JP (2005) Iron oxide copper-gold deposits; geology, space-time distribution, and possible modes of origin. Econ Geol 100:371-405

Chapter 2:

Mineral chemistry of magnetite from magnetite-apatite mineralization and their host rocks: Examples from Kiruna, Sweden and El Laco, Chile

Shannon G. Broughm[1], John M. Hanchar[1*], Fernando Tornos[2],

Anne Westhues[1], Samuel Attersley[1]

[1]Department of Earth Sciences, Memorial University of Newfoundland

St. John's, NL A1B 3X5 Canada

[2]Centro de Astrobiología (CSIC-INTA), Ctra. Ajalvir, km 4.5

28850 Torrejón de Ardoz, Madrid, Spain

Revised manuscript submitted to *Mineralium Deposita* on December 27th, 2016

Abstract

Interpretation of the mineralizing environment of magnetite-apatite deposits remains controversial with theories that include a hydrothermal or magmatic origin, or a combination of those two processes. To address this controversy, we have analyzed the trace element content of magnetite from precisely known geographic locations and geologic environments from the Precambrian magnetite-apatite ore and host rocks in Kiruna, Sweden, and the Pliocene-Holocene El Laco volcano in the Atacama Desert of Chile. Magnetite samples from Kiruna have low trace element concentrations with little chemical variation between the ore, host, and related intrusive rocks. Magnetite from andesite at El Laco, and dacite from the nearby Láscar volcano, has high trace element concentrations typical of magmatic magnetite. El Laco ore magnetite have low trace element concentrations and displays growth zoning in incompatible elements (Si, Ca, and Ce), compatible elements (Mg, Al, and Mn), LILE (Sr) and HFSE (Y, Nb, and Th). The El Laco ore magnetite are similar in composition to magnetite that has been previously interpreted to have crystallized from hydrothermal fluids; however, there is a significant difference in the internal zoning patterns. At El Laco each zoned element is either enriched or depleted in the same layers, suggesting the magnetite crystallized from a volatile-rich iron-oxide melt. In general, the composition of magnetite from these two deposits plot in very wide fields that are not restricted to the proposed fields in published discriminant diagrams. This suggests that the use of these diagrams and genetic models based on them should be used with caution.

Keywords Magnetite, magnetite-apatite deposits, Kiruna-type deposits, El Laco, magmatic-hydrothermal

Introduction

Genetic models for the formation of Kiruna-type magnetite-apatite deposits have been discussed and debated for over a century (e.g., Geijer, 1910, 1919; Parák, 1975; Frietsch, 1978; Nyström and Henríquez, 1994; Bergman et al., 2001). How these deposits relate to their adjacent host rocks and the relationship of the ore mineralization with hydrothermal alteration remains controversial (Hitzman et al., 1992; Williams et al., 2005; Groves et al., 2010). Additional research is necessary in order to obtain a better understanding of the processes involved in forming these deposits and how they relate, if at all, to other types of ore deposits (e.g., Fe-Ti oxide, iron oxide copper gold [IOCG], porphyry copper, skarn, volcanogenic massive sulfide [VMS]) (Williams et al., 2005; Dupuis and Beaudoin, 2011; Nadoll et al., 2014). In the present study, the trace element chemistry of magnetite from perhaps the two most representative, and well known, magnetite-apatite deposits, and their respective host rocks, was determined. The first is from Kiruna in the Norrbotten region of northern Sweden, and the second is from El Laco in the Atacama Desert region of northern Chile. In the case of the Kiirunavaara deposit in Kiruna, magnetite from two related intrusive rocks were also analyzed. For El Laco, magnetite was also analyzed from the nearby Làscar volcano. The aim is to determine whether the trace element chemistry of magnetite can be used to aid in settling the dispute on the processes involved in magnetite-apatite mineralization, e.g., hydrothermal, or magmatic, or a combination of these two processes. All of the samples used in this study are from precisely known geographic locations and geologic environments allowing a spatial analysis of the magnetite textures and associated minerals together with their trace element compositions.

Magnetite-apatite deposits can have high ore grades (up to 65% Fe) and large sizes (e.g., ~2500 million tons [Mt] of iron has been mined in Kiruna with 644 Mt proven and probable reserves [Bergman et al., 2001; LKAB, 2015] and ~730 Mt of iron ore at El Laco [Mario Rojo, Compañia Minera del Pacifico, 2015 pers. comm.]) making them attractive targets for mining. Magnetite-apatite deposits are the most important ore deposits in the Norrbotten region of northern Sweden (Bergman et al., 2001). The earliest studies on magnetite-apatite ores were focused on Kiruna (e.g., Geijer, 1910, 1935; Parák, 1975; Frietsch, 1978) where the expression "Kiruna-type" deposit was adopted for this class of low-Ti magnetite, apatite-rich iron ore (e.g., Hildebrand, 1986; Mücke and Younessi, 1994). Some later studies focused on the magnetite-apatite ores at El Laco in the Atacama Desert region of northern Chile, a much younger deposit, which is often considered a modern and shallow (i.e., Pliocene-Holocene) equivalent of the magnetite-apatite deposits found at Kiruna (e.g., Park, 1961; Nyström and Henríquez, 1994; Nyström et al., 2008).

Magnetite-apatite deposits are sometimes included as an end-member in the IOCG class of deposits (e.g., Hitzman et al., 1992; Barton and Johnson, 1996; Hitzman, 2000; Sillitoe, 2003). Both magnetite-apatite and IOCG deposits contain large volumes of distinctly low-Ti iron oxides within rocks that have undergone extensive alkali-calcic metasomatism by hydrothermal fluids. Magnetite-apatite deposits do not contain economic concentrations of Cu or Au and almost exclusively contain massive magnetite or both magnetite and hematite, while IOCG deposits may also contain iron-rich silicate phases (Parák, 1975; William et al., 2005; Groves et al., 2010). In some locations, magnetite-apatite deposits and IOCG deposits occur spatially, but usually not temporally,

associated with each other; though, whether there is a genetic relationship between the formation of magnetite-apatite and IOCG deposits remains unresolved (e.g., Groves et al., 2010).

There are two genetic models, and a third that is a combination of the first two, for the formation of magnetite-apatite deposits today: 1) Crystallization from iron-rich melts that were immiscible from a parental silicate melt and were emplaced at different depths or erupted and crystallized at the surface (e.g., Henríquez and Martin, 1978; Nyström and Henríquez, 1994; Naslund et al., 2002; Alva-Valdivia et al., 2003; Nyström et al., 2008; Martinsson, 2016); crystallization was accompanied by the exsolution of large amounts of magmatic-hydrothermal fluids (Tornos et al., 2016); 2) Replacement of the host rocks by iron-rich hydrothermal fluids (e.g., Hitzman et al., 1992; Rhodes and Oreskes, 1999; Hitzman, 2000; Sillitoe and Burrows, 2002; Edfelt et al., 2005; Groves et al., 2010; Valley et al., 2011; Dare et al., 2015); and 3) a magmatic-hydrothermal genesis with an early generation of phenocrysts of magnetite that separated and floated from a crystallizing andesite melt and later were overgrown by hydrothermal magnetite (e.g., Knipping et al., 2015). A sedimentary-exhalative origin was suggested by Parák (1975) but was not widely accepted (Frietsch, 1978; Nyström et al., 2008) and will not be discussed further.

Field observations and geochemical data for magnetite-apatite deposits are arguably compatible with both magmatic and hydrothermal origins (Hitzman et al., 1992; Nyström and Henríquez, 1994; Naslund et al., 2002). Field evidence at the El Laco ore bodies that strongly supports an ultimate magmatic origin for the mineralization, i.e., direct crystallization from an iron-rich melt, includes distinct magnetite volcanic flow

structures, vesicles in the magnetite ore veins with chilled margins that crosscut the host andesite, as well as the presence of degassing tubes similar to textures observed in basaltic flows (Henríquez and Martin, 1978; Nyström and Henríquez, 1994; Naslund et al., 2002; Henríquez 2003; Tornos et al., 2016).

Arguments that support a hydrothermal (metasomatic) origin at El Laco include the presence of, sometimes jigsaw-like, breccias in which the magnetite supports fragments of altered host andesite blocks; a feature that is explained by open-space filling of ascending hydrothermal fluids (Sillitoe and Burrows, 2002). Brecciated contacts between the ore and hydrothermally altered host rocks are fairly common at other magnetite-apatite deposits (e.g., Kiruna, the Adirondacks/New York State, and Bafq/Iran; Geijer, 1910; Bergman et al., 2001; Valley et al., 2011; Sabet-Mobarhan-Talab et al., 2015; Westhues et al., 2016). Metasomatism of the host rocks surrounding these deposits is strong evidence that hydrothermal fluids were present. In Kiruna the host rocks are pervasively hydrothermally altered (Westhues et al., 2016); however, at El Laco there is not always direct contact between the altered host rock and ore suggesting the hydrothermal alteration here may not be directly related to ore emplacement (Tornos et al., 2016).

The magmatic model for magnetite-apatite ores involves the existence of immiscible iron rich-melts that crystallized to produce the large volumes of massive magnetite. This type of melt is considered to be similar to nelsonite deposits, which have a 2:1 oxide:apatite ratio and contain abundant Ti in the form of mostly rutile +/- ilmenite +/- titanomagnetite). (Philpotts, 1967; Frietsch, 1978; Kolker, 1982; Dymek and Owens, 2001). Kamenetsky et al. (2013) tracked the existence of a large immiscibility gap

between silica-rich felsic melts and silica-poor mafic melts. The mechanism(s) through which the iron-rich melts efficiently segregate into the ore and a presumed residual parent silicate-rich melt at the scale of massive deposits like those in Kiruna or El Laco, has not yet been determined or observed in the field (i.e. the magnetite-apatite ore and residual silicate-melt in contact with each other). However, immiscible iron-rich and silicate melts have been observed within melt inclusions in the host andesite rocks at El Laco (Tornos et al., 2016; Velasco et al., 2016).

Hydrothermal models for magnetite-apatite deposits are extrapolated from hydrothermal models for IOCG deposits, with the assumption that these two types of deposits are genetically similar (Barton and Johnson, 2004). Two main fluid sources have been proposed: 1) hydrothermal fluids exsolved from a magmatic source (e.g., Sillitoe and Burrows, 2002; Groves et al., 2010); or, 2) derived from an external source (e.g., basinal brines) where igneous intrusions are a heat source for circulating fluids in the crust (e.g., Barton and Johnson, 1996; Rhodes and Oreskes, 1999). Each system would require the generation of saline, sulfur-poor, and oxidized fluids (Barton and Johnson, 2004). It is possible that there are multiple sources for the fluids and they may vary between different localities (Williams et al., 2005; Valley et al., 2011).

Magnetite is an abundant and widespread oxide mineral and occurs in igneous, sedimentary, hydrothermal, and metamorphic rock assemblages and different types of ore deposits (Lindsley, 1991). Magnetite is a member of the spinel group of minerals, which have a cubic close-packing structure with tetrahedral (Fe^{2+}) and octahedral (Fe^{3+}) sites in coordination with oxygen anions and the general stoichiometry $Fe^{2+}Fe^{3+}{}_2O_4$ (Buddington and Lindsley, 1964; Lindsley, 1976). A variety of lithophile and siderophile elements

with similar ionic radii to Fe^{2+} and Fe^{3+} substitute in the magnetite structure (e.g., Mg, Al, Si, P, Ca, Ti, V, Cr, Mn, Co, Ni), though in certain favorable physicochemical conditions chalcophile and other elements can also be incorporated (e.g., Cu, Zn, Ga, Sn, Ce) (Nadoll et al., 2014). Of special interest is the behavior of Ti; the solubility of Ti in magnetite is controlled by the redox state and temperature of the system (Lindsley, 1976). Magnetite is known to be resistant to surface weathering making it an ideal provenance indicator for mineral exploration and perhaps useful for genetic studies of ore deposits (Grigsby, 1990; Dupuis and Beaudoin, 2011; Dare et al., 2012; Nadoll et al., 2014).

Several previous studies have discussed magnetite trace-element chemistry from Kiruna, El Laco, and other magnetite-apatite deposits (e.g., Loberg and Horndahl 1983; Frietsch 1995; Muller et al., 2003; Dupuis and Beaudoin 2011; Dare et al., 2015); however, most of the magnetite samples used in these studies were not from precisely known locations within the ore and surrounding host rocks. Some of these studies have proposed empirical plots in which the magnetite of different types of mineralization have a characteristic trace element signature. In these diagrams, magnetite from magnetite-apatite deposits have distinct trace element chemical compositions compared to magnetite from other deposit types, such as banded iron formations (BIF), IOCG, nelsonite, porphyry Cu and Fe-Ti-V deposits (e.g., Loberg and Horndahl, 1983; Dupuis and Beaudoin, 2011; Dare et al., 2014). Dare et al. (2015) proposed that the composition of the magnetite from the El Laco ore, which is different to that of the accessory magnetite in the unaltered host andesite, is consistent with a hydrothermal origin for the magnetite-apatite ore (e.g., Dare et al., 2015).

The present study uses newly obtained data on the magnetite trace element geochemistry to assess the practical use and limitations of the proposed empirical magnetite discrimination diagrams and whether they can be utilized in interpreting the mineralization style and ore genesis of magnetite-apatite deposits.

Geologic background

Kiruna geology and magnetite-apatite ores

There are over 40 known magnetite-apatite deposits located in the Norrbotten region, with Kiirunavaara being the largest estimated at nearly 2 Ga before extraction of high-grade iron ore averaging 30-70% Fe (e.g., Cliff et al., 1990; Hallberg et al., 2012; Martinsson, 2016; Westhues et al., 2016). The Kiirunavaara magnetite-apatite deposit is a tabular-shaped ore body approximately 5 km long, 100 m thick and at least 1500 m deep that lies concordant within steeply dipping volcanic host rocks (e.g., Parák, 1975; Blake, 1992; Bergman et al., 2001; Harlov et al., 2002; Nyström et al., 2008).

The oldest unit in the Kiruna area are the Karelian (2.4-1.96 Ga) mafic-intermediate metavolcanic flows (Kiruna Greenstone Group), overlain by metasedimentary and intermediate-felsic metavolcanic rocks of the Svecofennian Porphyry group (1.96-1.75 Ga) (Fig. 1a) (e.g., Bergman et al., 2001). The magnetite-apatite deposits in the Kiruna area are hosted by the metavolcanic rocks of the Porphyry Group (Parák, 1975; Martinsson, 2004). The Kiirunavaara-Luossavaara ore bodies follow the contact between thick trachyandesitic lava flows (footwall) and pyroclastic rhyodacites (hanging wall). The entire Norrbotten region has been subjected to greenschist facies metamorphism (Bergman et al., 2001) and is overprinted by regional

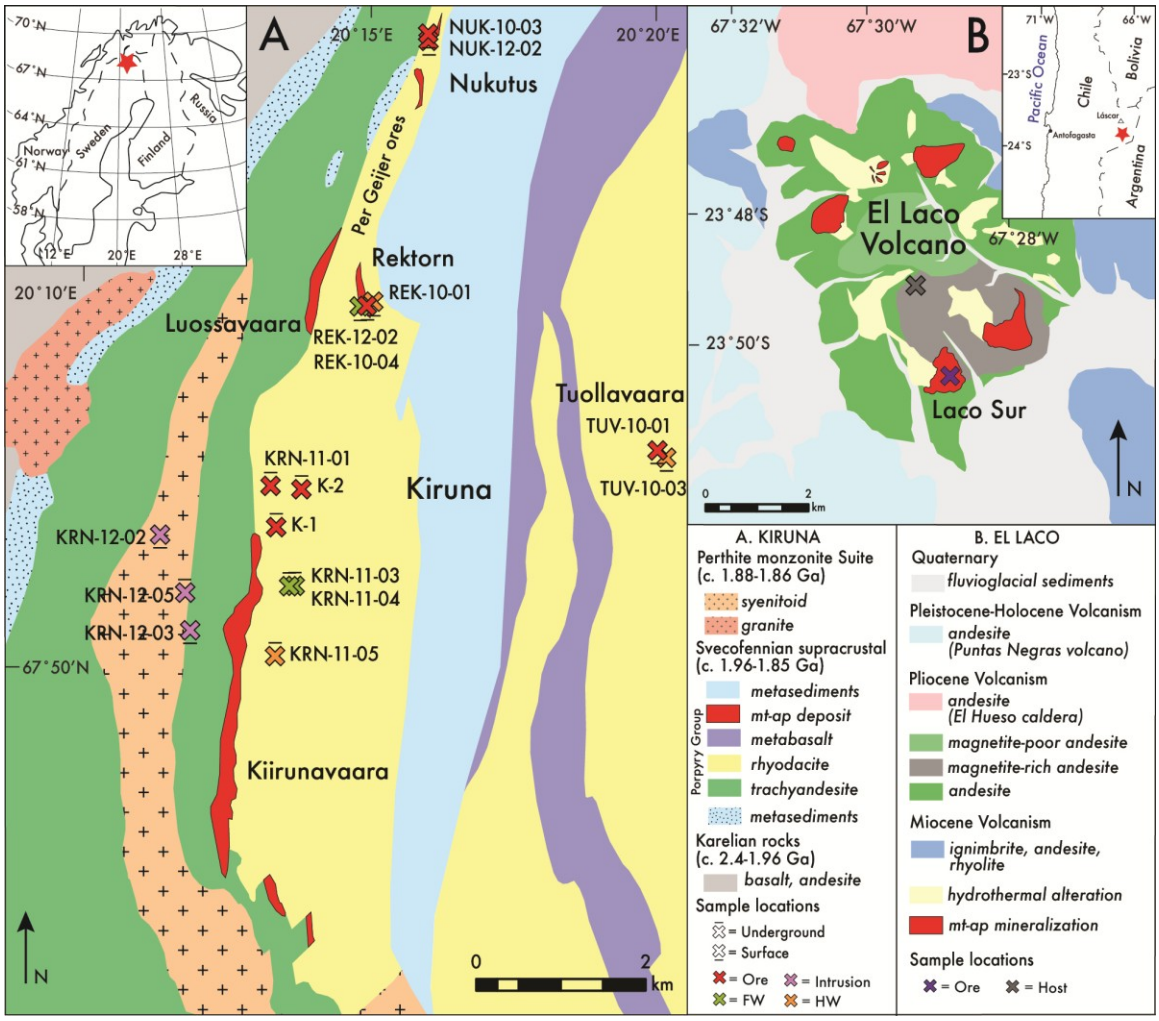

Fig. 1. Simplified geological maps of the study areas. a) Kiruna district, Norrbotten region, northern Sweden, with sample locations for this study. The Kiirunavaara magnetite-apatite deposit dips eastward between the footwall and hanging wall rock units. Samples collected underground within the mine are projected to the map surface and therefore appear to the east of ore body (map modified after SGU data and Westhues et al., 2016). b) El Laco volcano, ore samples from this study are from the Laco Sur deposit with one dacite sample from the Láscar volcano shown in the inset map (map modified after Tornos et al., 2016)

scale Na and Cl metasomatism in the form of albite and Cl-rich scapolite ($Na_4Al_3Si_9O_{24}Cl$–$Ca_4Al_6Si_6O_{24}CO_3$) (Frietsch et al., 1997).

There is a syenite intrusion approximately 1 km stratigraphically below the Kiirunavaara ore body (Blake, 1992; Bergman et al., 2001). Granophyric to granitic

dykes intrude the Kiirunavaara ore, and a larger body of potassic granite can be found within the footwall of the Kiirunavaara mine. New constraints on the ages of these intrusions show that the syenite (1880 ± 7 and 1881 ± 4 Ma) is of a similar age to the metavolcanic host rocks (1884 ± 4 and 1880 ± 3 Ma) and older than the ore (1877 ± 4 and 1874 ±7 Ma), while zircon from the granite (1874 ± 7 Ma) and two ore samples have overlapping ages (Westhues et al., 2016).

Two types of ore can be identified at Kiirunavaara based on their phosphorous content, primarily residing in apatite: the B-ore (<0.05% P) and D-ore (>1% P) (e.g., Bergman et al., 2001). The ore is rich in rare earth elements (REE); dominantly as light rare earth elements contained within the apatite or in inclusions of monazite in apatite, which is currently not mined (Hallberg et al., 2012). The contact with the host rocks is bounded by a magnetite-actinolite filled breccia with veins that can be found extending tens of meters into the hanging wall (Bergman et al., 2001). The footwall at Kiirunavaara is strongly albitized, especially near the syenite intrusion, and here widespread amygdales are found to contain secondary magnetite, actinolite and titanite (Geijer, 1910; Romer et al., 1994; Bergman et al., 2001).

The Tuollavaara and Per Geijer (e.g., Nukutusvaara and Rektorn) ore bodies are smaller than Kiirunavaara and are hosted within rhyodacites in the upper parts of the Porphyry Group (Martinsson, 1994; Bergman et al., 2001). Hematite is more common in these smaller deposits than at Kiirunavaara. Contacts between the ore and host rocks are often brecciated (i.e., altered host rock fragments are surrounded by veins of iron oxides + apatite) and veining of iron ore commonly extends into both footwall and hanging wall up to tens of meters (Bergman et al., 2001).

El Laco geology and magnetite-apatite ores

The El Laco andesite stratovolcano is located in the current active volcanic arc, the Central Volcanic Zone (CVZ), of the Andes in the Atacama Desert of northern Chile (Fig. 1b). The volcano is made up of calc-alkaline andesite flows and pyroclastic rocks, with K-Ar dates from 5.3 +/- 1.9 Ma to 1.6 +/- 0.5 Ma (Naranjo et al., 2010). There are seven high-grade iron ore bodies at El Laco that reach up to 1 km^2 at the surface and exceeding 100 m thickness. (Naslund et al., 2002). The dominant magnetite mineralization occurs as large stratabound lenses that are texturally massive, brecciated, vesicular or friable and are interpreted as lava flows or pyroclastic rocks. They are rooted in subvertical veins of massive and coarse grained magnetite (Henríquez and Martin, 1978; Nyström and Henríquez, 1994; Naslund et al., 2002; Nyström et al., 2016; Tornos et al., 2016). The magnetite ore is associated with minor amounts of diopside, scapolite and anhydrite (Tornos et al., 2016) while apatite is fairly uncommon in the stratabound ores but is abundant in the feeder dykes.

The magnetite-apatite ore bodies and some of the andesite host rocks have been pervasively overprinted by hydrothermal alteration that is thought to be broadly synchronous with the emplacement of the magnetite ore (see Fig. 1b). The andesite has been locally replaced by alkali-calcic hydrothermal assemblages, including diopside, K-feldspar, magnetite, anhydrite and scapolite that are related to widespread brecciation of the altered andesite (Tornos et al., 2016). The andesite host and the alkali-calcic altered rocks are overprinted by a later and shallower steam-heated alteration that is observed as stratabound zones of dominantly alunite and gypsum (Sillitoe and Burrows, 2002; Tornos et al., 2016). Late martitization related to the steam-heated alteration overprints large parts of the magnetite ore (Tornos et al., 2016).

Láscar volcano

The Láscar volcano is located approximately 57 km northwest of El Laco (67°43'W; 23°22'S) and is the most active volcano in the CVZ today with a significant eruption in 1993 and intermittent activity ever since (Tassi et al., 2009). Láscar is considered a typical arc-related volcano with andesitic to dacitic composition. The andesite-dacite at Láscar includes anhydrite phenocrysts as well as droplets of magnetite - no significant concentrations of massive magnetite have been described. The reason to compare the geochemistry of magnetite at El Laco and Láscar volcanoes is to determine if a difference exists with the magnetite from a volcano with massive magnetite mineralization, such as El Laco, with a similar volcano located within the same volcanic arc system that does not have visible massive magnetite deposits, such as Láscar.

Analytical methods

Sample selection and preparation

The magnetite-bearing rocks of this study have been selected using a systematic sample collection that was carried out from magnetite-apatite ores and their respective host rocks in the Norrbotten region of northern Sweden and the El Laco and Láscar volcanoes (Fig. 1 and Appendix I). The samples have been thoroughly examined using cross-polarized and reflected light microscopy on polished thin sections in order to select the samples with minimal replacement of magnetite by hematite. Magnetite grains were chosen in situ from the samples of ore, hanging wall, and footwall as well as from any spatially associated intrusive rocks. Some samples from the host rocks did not contain magnetite or the grains were not large enough for laser ablation analysis and therefore

could not be included in this study (e.g., many of the more felsic hanging wall rocks at Kiruna and altered andesite at El Laco).

For Kiruna, samples that contain sufficient magnetite included all the ore samples from the Kiirunavaara high-P (KRN-10-02, K-1 and KRN-11-01) and low-P (K-2) ore and the selected smaller magnetite-apatite ores, Tuolluvaara (TUV-10-01), Nukutusvaara (NUK-12-02 and NUK-10-03) and Rektorn (REK-10-04). The Rektorn ore also contains abundant hematite, described further below. At Kiirunavaara, the footwall andesite rocks were magnetite-rich and there was an altered (KRN-11-04) and a less altered (KRN-11-03) sample chosen. One sample from the hanging wall rhyodacite rocks at Kiirunavaara contained a small amount of magnetite (KRN-11-05). Several samples containing magnetite from felsic intrusive bodies spatially associated with the Kiirunavaara ore body were also chosen, these included an aplite vein (KRN-12-02) a syenite pluton (KRN-12-03) and a granite pluton from underground inside the mine (KRN-12-05). As mentioned above, the smaller magnetite-apatite bodies in Kiruna (i.e., Per Geijer ores: Rektorn, Nukutus, and Tullovaara) are hosted in the rhyodacitic rocks that generally do not contain abundant magnetite. However, sufficiently sized magnetite was present in the host rock at Tuollavaara (TUV-10-03). The Rektorn footwall (REK-12-02) contains abundant magnetite and the Rektorn hanging wall was eliminated from this study because it contains abundant hematite.

At El Laco in the upper levels of the large magnetite-apatite ore body at Laco Sur two massive magnetite ore samples were collected (ELL-14-04 and ELL-14-05). In the lower levels of the Laco Sur ore body (at approximately 4650 m elevation) a magnetite vein from a feeder structure was sampled (ELL-14-06). A sample of andesite from the El

Laco volcano (ELL-14-02) and a dacite sample from Láscar (LAS-14-07) were also collected.

The magnetite-bearing samples selected (n=17 from Kiruna; n=4 from El Laco and n=1 from Láscar) were first trimmed with a saw to remove any altered or weathered material and then mounted in 25 mm diameter by 6 mm tall epoxy pucks. These pucks were then polished and carbon coated and examined with a JEOL 7100F scanning electron microscope (SEM) at Memorial University of Newfoundland equipped with energy dispersive spectroscopy (EDS) at 15 kV and 50 nA. Magnetite grains, as well as any associated minerals, were identified using back-scattered electron (BSE) imaging and confirmed with EDS and later with conventional reflected light microscopy to distinguish between magnetite and hematite.

EPMA analyses

The iron content of the magnetite grains was measured using a JEOL JXA-8230 SuperProbe electron probe microanalyzer (EPMA) at Memorial University of Newfoundland. Details concerning the EPMA analyses are summarized in Appendix II and a complete list of the Fe results in Appendix IV. Quantitative chemical analyses of magnetite were done to obtain Fe concentrations in the same location as the LA-ICPMS analyses to use Fe as the internal standard for reducing the laser ablation data with Iolite software (Paton et al., 2011). The following conditions were used for the EPMA analyses: accelerating voltage of 15 kV, sample current of 100 nA, peak and background count times of 10 s and a beam diameter of 3 μm. Natural magnetite from the Astimex MINM25-53 mineral standards mount was used as a primary Fe standard. Raw X-ray intensities were corrected using standard ZAF techniques with the JEOL software.

X-ray maps

X-ray maps of the Kiruna magnetite grains were made on one representative magnetite grain per sample for Al, Si, Ca, Ti and V. Vanadium was mapped instead of Mg for the Kiruna analyses after variations in V were detected with energy dispersive spectroscopy (EDS). Aluminum and Ti were also chosen because of their generally immobile nature in hydrothermal fluids. Silica and Ca were chosen for their highly mobile nature in hydrothermal fluids (Dare et al., 2014; Nadoll et al., 2014). For the El Laco samples, EPMA X-ray maps for Al, Si, Ca, V, and Mg were acquired on one representative magnetite grain per sample. For each map an accelerating voltage of 15 kV, and sample current of 250 nA, and a pixel dwell time of 150 ms was used. The map area, step size and total time to create each map ranged from 150 μm^2 to 2 mm^2, 0.4 to 1.0 μm, and 4 to 10 hours, respectively, depending on the size of the magnetite grain.

LA-ICPMS analyses

In situ LA–ICPMS analyses were done at the MicroAnalysis Facility – Bruneau Innovation Centre (MAF–IIC) at Memorial University of Newfoundland using a Finnigan Element XR high-resolution double-focusing magnetic-sector inductively coupled plasma mass spectrometer (HR-ICPMS), coupled to a GeoLas 193 nm Excimer laser system. Details for the LA-ICPMS analyses are summarized in the Appendix II. Zipkin et al. (2015) describes the current methodology in the LA-ICPMS facility for trace element analysis using this equipment; these same methods were used in the present study with the modifications noted below.

A laser spot diameter of 30 μm was used for all magnetite analyses, a 59 μm spot was used for the primary calibration material NIST 610, and a 49 μm spot for the

secondary standard reference material BCR-2G. A total of 42 elements and 35 elements, respectively, were analyzed for each magnetite analysis during the Kiruna and El Laco LA-ICPMS analyses. Magnetite samples from El Laco were analyzed prior to the Kiruna samples and elements that were consistently below the limit of detection (LOD) were not measured during the Kiruna analyses after verifying that those elements were again not detectable. Instead, rare earth elements (REE) were included for the Kiruna analyses in order to make a comparison with the well-constrained trace REE concentrations in the BCR-2G glass (Jochum et al., 2005). The laser energy density used for all laser ablation analyses was 3 J/cm^2 with a pulse frequency of 8 Hz. For each analysis, the background was measured for about 30 s, followed by 90 s of laser ablation, and wash out was monitored for about 20 s after each ablation. Isotope signals ^{57}Fe, ^{51}V, and ^{9}Co were closely monitored during the day to track instrumental drift. For the El Laco ablation session laser spots were taken across grains that showed zoning in BSE and X-ray maps. A total of 72 analyses were done on magnetite from El Laco and Láscar. Eighty-seven analyses were done on magnetite from the Kiruna area samples. A complete list of the analyses that was done as well as the spot locations is reported in the Appendix V and VI, respectively.

The LA-ICPMS data were reduced using the Iolite software (Paton et al., 2011) with the Fe concentration from the EPMA analysis used as the internal standard. Peaks for La, Ce, Al, Mg, Zr, Si, P, Ca, and Ti were monitored during the data reduction to avoid inclusions of other minerals (e.g., monazite, apatite, zircon, titanite) or inclusion of the host material in the case of tiny magnetite grains (e.g., feldspar, amphibole, quartz). The LOD for each of the elements measured was calculated in Iolite (Paton et al., 2011)

using the method described in Zipkin et al. (2015). The LOD and mean results of each isotope measured are listed in Appendix III. The BCR-2G results from the Kiruna and El Laco analysis sessions show excellent correlation with the long term running averages for BCR-2G collected over a span of 17 years at Memorial University (see Fig. 2 and Appendix VIII).

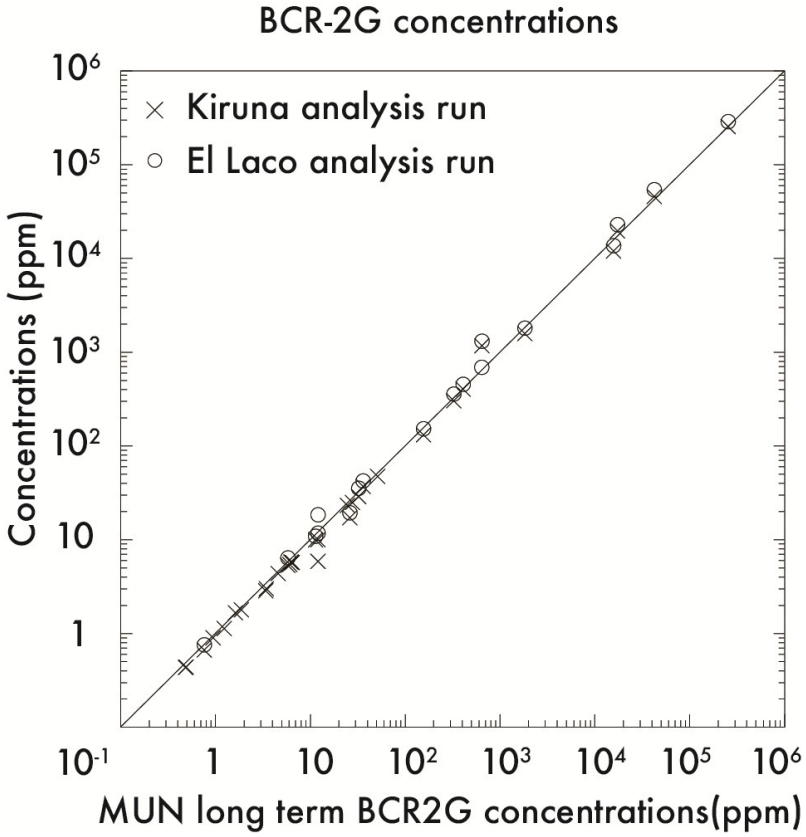

Fig. 2. LA-ICP-MS BCR-2G average concentrations for this study (y-axis) compared with the MUN BCR-2G long term average from 1997-2014 (x-axis).

Results

Kiruna magnetite textures and associated minerals

From the samples investigated at Kiirunavaara, the D-ore (i.e., high-P ore) contains two types of magnetite: 1) massive magnetite with interstitial apatite, biotite, and

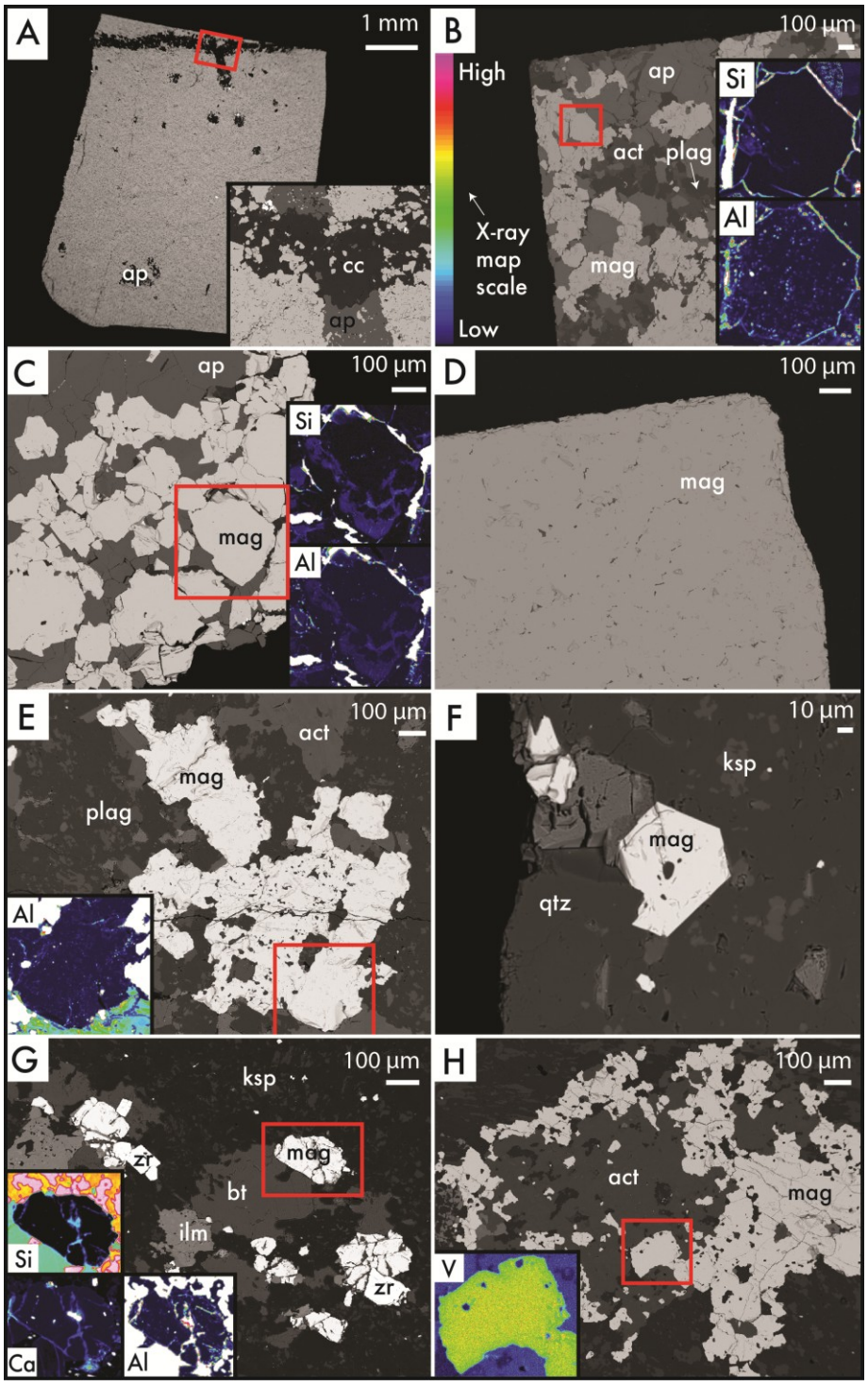

Fig. 3. Back-scattered electron images and chemical X-ray maps of representative magnetite (*mag*) from the Kiirunavaara ore, host rocks and associated intrusive rocks. Relative chemical variation scale for X-ray maps in b. Red boxes show locations of BSE images or X-ray maps that are shown as insets. a) KRN-10-02 (D-ore), massive magnetite with interstitial apatite (*ap*) and cross cutting calcium carbonate (*cc*) vein. b)

K-1 (D-ore), subhedral magnetite grains with zones of slight increases in Si and Al shown in X-ray map. c) KRN-11-01 (D-ore), subhedral magnetite with correlating zones of increased in Si and Al. d) K-2 (B-ore), massive magnetite. e) KRN-11-04 (FW), anhedral magnetite aggregate associated with actinolite (*act*), X-ray map shows spots of increased Al. f) KRN-11-05 (HW), small euhedral-subhedral magnetite grain. g) KRN-12-02 (syenite intrusive), small anhedral magnetite grains associated with zircon (*zr*), biotite (*bt*) and ilmenite (*ilm*), cracks filled with increased Ca, Si and Al concentrations. h) Anhedral magnetite associated with actinolite, rim of magnetite depleted in V relative to the core. Other mineral abbreviations: K-feldspar (*ksp*), quartz (*qtz*) and plagioclase (*plag*).

later calcite (Fig. 3a); and 2) 20-200 μm magnetite grains that are subhedral to anhedral with apatite as the dominant gangue mineral phase +/- actinolite, plagioclase, and quartz (Fig. 3b, c). The B-ore (i.e., low-P ore, Fig. 3d) magnetite is massive with interstitial biotite and calcite and contains much less apatite (and thus phosphorus) than the D-ore. The Kiirunavaara trachyandesitic footwall has large anhedral magnetite grains ranging in size from 100-300 μm that are found in clusters as well as disseminated magnetite. The magnetite clusters are more abundant and larger (approximately 1 mm in diameter) in the altered footwall (Fig. 3e) compared to the less altered footwall (approximately 500 μm in diameter). The hanging wall rocks at Kiirunavaara have a low abundance of magnetite with grains that are euhedral-subhedral and <60 μm (Fig. 3f). The aplite vein sample (KRN-12-02) has a low abundance of magnetite with grains that are <100 μm, fractured and associated with biotite, titanite and zircon (Fig. 3g). The syenite sample (KRN-12-03) has 50-100 μm sized anhedral magnetite grains that are commonly associated with actinolite (Fig. 3h). The potassic granite intrusion (sample KRN-12-05) found underground within the mine (Westhues et al., 2016) has disseminated euhedral to anhedral magnetite grains that are <60 μm in size.

The Tuollavaara ore has subhedral to anhedral magnetite grains that range in size from 100-800 µm (Fig. 4a). The host rock at Tuollavaara has disseminated magnetite with typically 1 mm sized clusters of <100 µm sized grains that are anhedral (Fig. 4b).

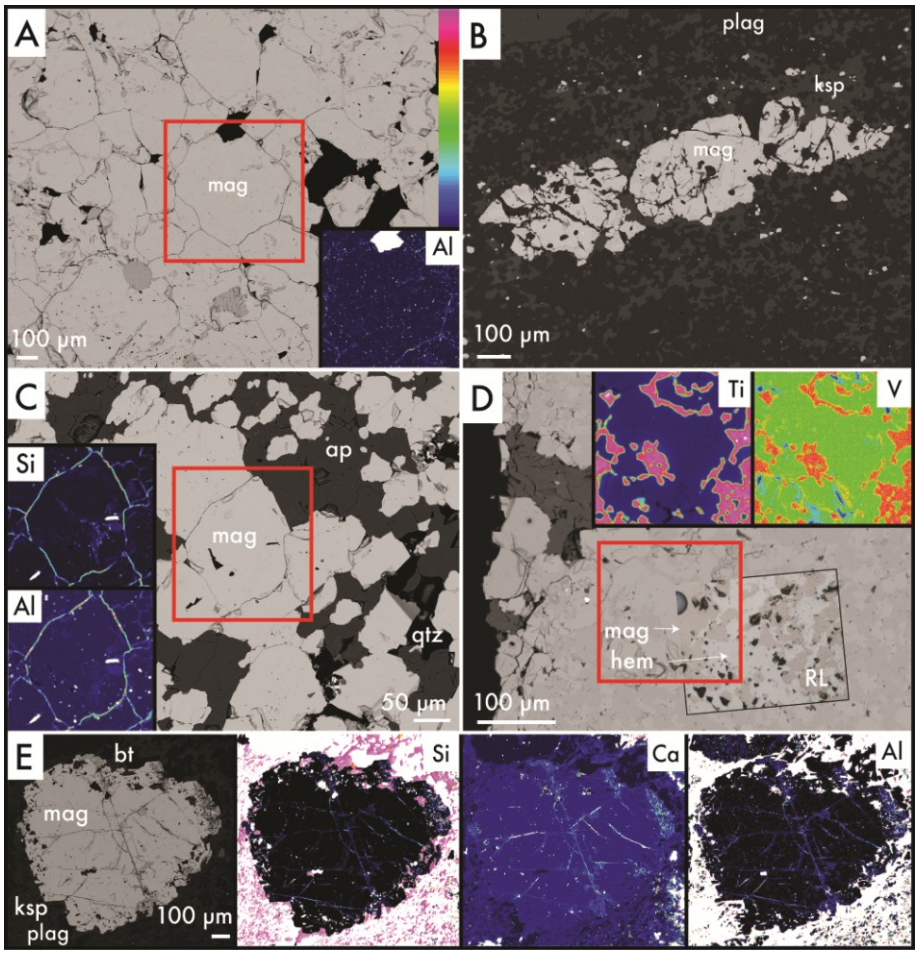

Fig. 4. Back-scattered electron images and chemical X-ray maps of representative magnetite (*mag*) from the smaller magnetite-apatite ores and their host rocks in Kiruna. Relative chemical variation scale for X-ray maps in a. Red box surrounds area of X-ray maps that are shown as insets. a) TUV-10-01 (ore) equally distributed spots of high aluminum present in X-ray map are visible as darker spots in the BSE image b) TUV-10-03 (hanging wall), anhedral magnetite. c) NUK-10-03 (ore), X-ray maps of Si and Al show a correlation. d) REK-10-04 (ore), massive magnetite with dark hematite (*hem*) and brighter magnetite areas in BSE correlating to white and pink, respectively, in reflected light (RL). The hematite has high Ti and V compared to the magnetite in the X-ray maps. e) REK-12-02 (FW), correlating increase in Ca, Si and Al are located along fractures in magnetite grain as seen in BSE image (left).

The Nukutus ore has subhedral to anhedral magnetite grains that range in size from 10-150 μm with abundant apatite and interstitial actinolite +/- quartz, calcite and biotite (Fig. 4c). The Rektorn ore is massive with interstitial calcite and quartz; BSE imaging revealed that approximately 60% of ore is lighter and therefore different in composition; under reflected light it was determined that the lighter BSE iron oxide is magnetite and the darker BSE iron oxide is hematite (Fig. 4d); both iron oxide phases were analyzed and differences in the chemistry are described in more detail below. The Rektorn footwall host rocks contain abundant 1 mm sized magnetite grains with rims that are rich in inclusions of feldspar, biotite and quartz (Fig. 4e).

El Laco magnetite textures and associated minerals

The magnetite ore samples studied at the Laco Sur magnetite-apatite deposit are dominated by massive or anhedral magnetite, up to 2 mm sized euhedral to subhedral grains can be found along the edges of void spaces (Fig. 4). Unlike the magnetite-apatite ore at Kiruna the El Laco magnetite is generally not associated with other mineral phases and shows partial to extensive alteration to martite (i.e., pseudomorphic replacement of magnetite by hematite). One of the samples from the upper levels of the ore body (ELL-14-04) consists primarily of massive magnetite or anhedral μm-sized grains of magnetite; there are abundant cm-sized elongated voids that are lined by 200-400 μm euhedral magnetite crystals.

In BSE images, the magnetite grains have porous inner cores that display chemical growth zoning and outer regions with no detectable chemical zoning (Fig. 4a). Under reflected light the magnetite crystals show extensive alteration to kenomagnetite (nominally $Fe^{2+}_{1-y}(Fe^{3+}_{1-2/3y}[]_{y/3}O_4$) and less extensively hematite along fractures (Fig. 4a)

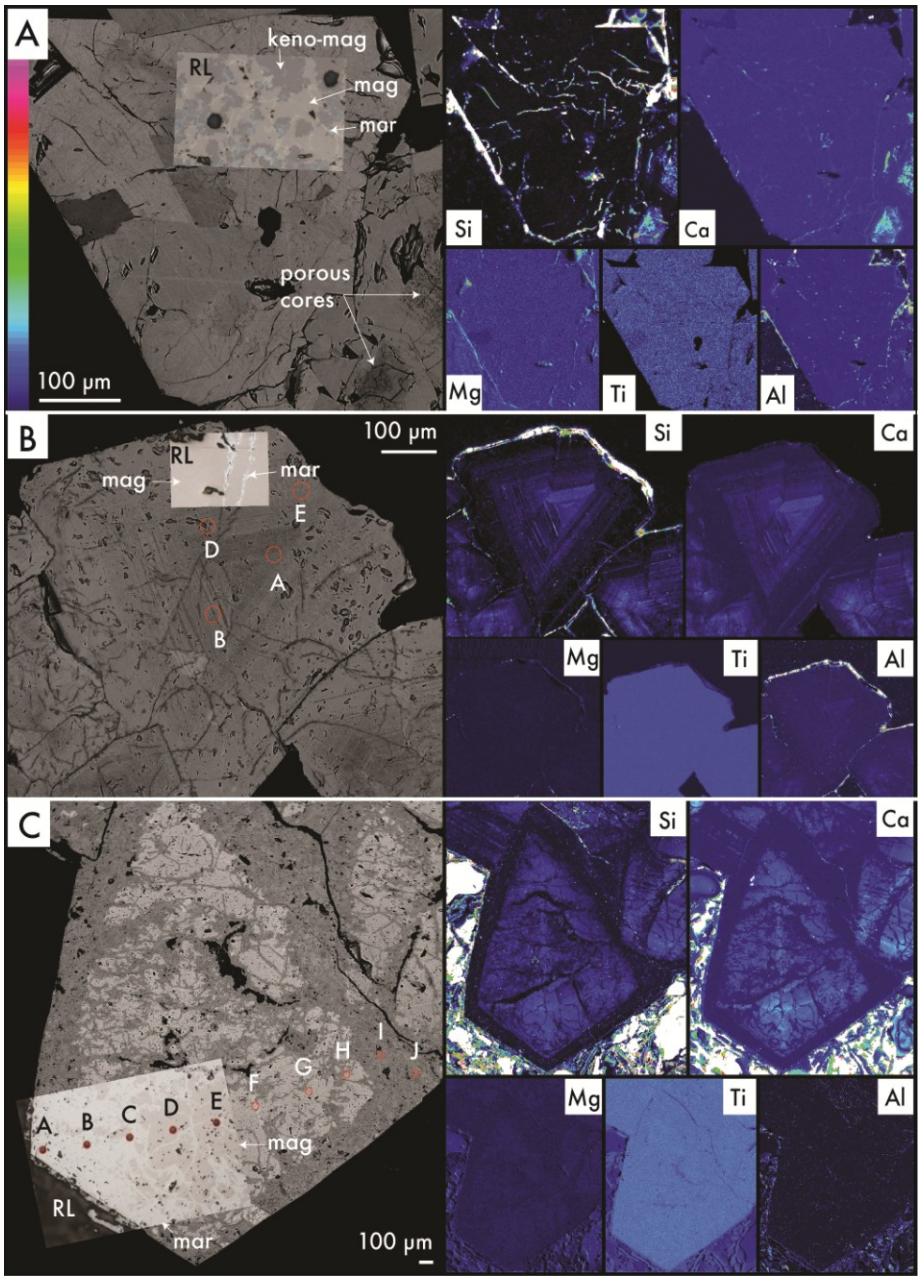

Fig. 5. Back-scattered electron images and chemical X-ray maps of representative Laco Sur ore magnetite. Relative chemical variation scale for X-ray maps in a. Orange circles represent LA-ICPMS spot locations relevant to Fig. 7 and X-ray maps include the whole crystals shown in the BSE image. Direct comparisons in the zoning contrast in BSE cannot be made between each sample because the photographs were taken at different settings to optimize the chemical structure in the magnetite grains. a) ELL-14-04, subhedral-euhedral magnetite grain with clear zoning in BSE imaging and no evident zoning in the X-ray maps for this grain. Adjacent grains with vuggy cores show elevated growth zones of Si, Ca and Al. Reflected light (RL) microscopy shows areas of the grain has been altered to kenomagnetite (*keno-mag*) and slight martite (*mar*) replacement along

fractures. b) ELL-14-05, subhedral-euhedral magnetite grains with clear growth zoning in the BSE image that correlates with the X-ray maps for Si, Ca and Al, each element is elevated or depleted in the same layers with increasing concentrations towards the core. RL microscopy shows slight martite replacement along fractures. c) ELL-14-06, euhedral magnetite with clear zoning that correlates with increasing Si and Ca towards the core. RL microscopy shows that extensive replacement of the magnetite to martite has occurred, which correlates to very low trace element concentration in the X-ray maps.

(Ramanaidou et al., 2008). Another sample from the upper levels of the ore body (ELL-14-05) consists primarily of spongy porous magnetite with cm-sized elongated voids that are lined with 200-600 μm euhedral magnetite crystals. In BSE images, the magnetite crystals have concentric growth zoning with darker central regions. Under reflected light hematite alteration can be seen along fractures in the magnetite and the edges of the magnetite (Fig. 4b). The magnetite from a magnetite vein in the lower level of the ore body (ELL-14-06) has 0.5-2 mm sized magnetite grains that are euhedral along the edge of 0.5-1 cm sized cavities and the magnetite is anhedral elsewhere. In BSE images, the magnetite grains displays a lighter core with darker portions that occurs along fractures and the grain rims (Fig. 4c). Under reflected light the lighter BSE portions of the grain can be identified as magnetite and the darker portions are martite.

The andesite host rock has microphenocrysts of magnetite, 100-200 μm in size, that are anhedral and contain trellis texture exsolution lamellae that in BSE images are visibly darker than the magnetite (Fig. 6a). Under reflected light the lamellae were identified as ilmenite. The Láscar dacite has disseminated anhedral magnetite in <100 μm sized grains with local exsolution lamellae, visibly darker in BSE images, but this is not widespread (Fig. 6b). The exsolution lamellae in the Láscar dacite were identified as

ilmenite with reflected light microscopy, a common texture found in titaniferous magnetite (Mehdilo and Irannajad 2010).

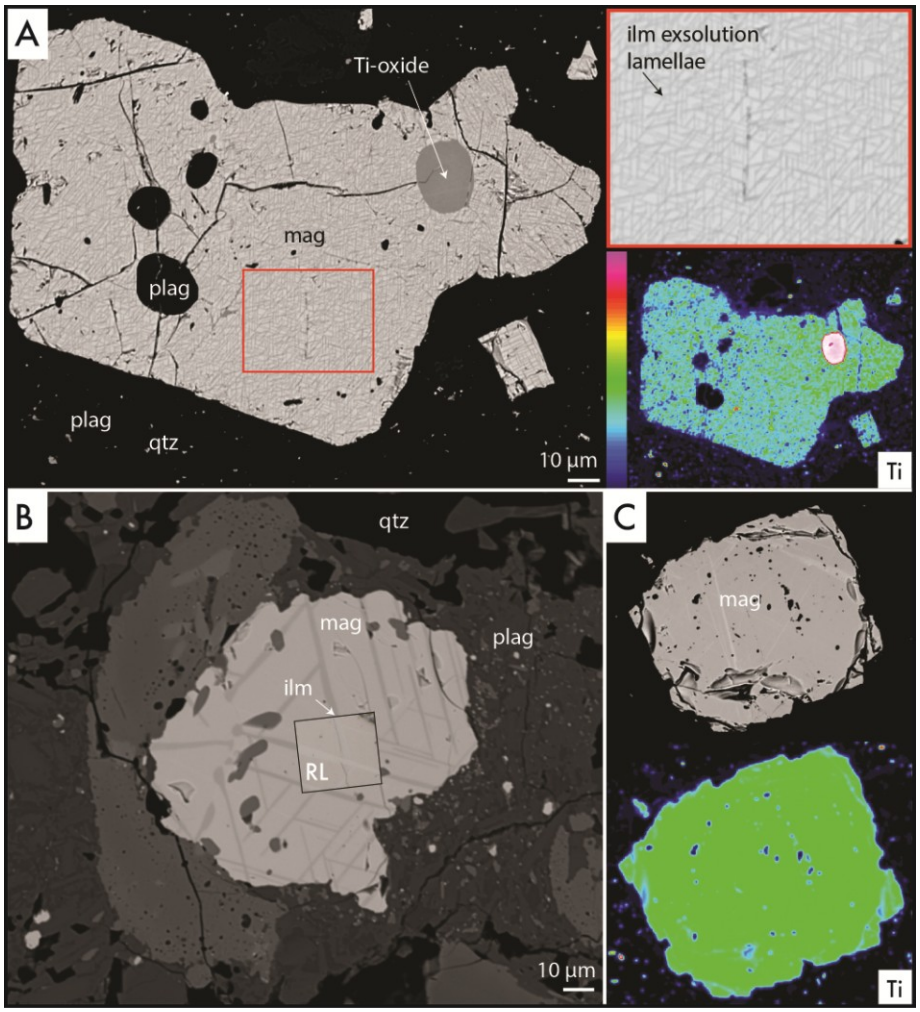

Fig. 6. Back-scattered electron images and chemical X-ray maps of magnetite from the andesite host rock at El Laco volcano and the dacite sample from Láscar volcano. Relative chemical variation scale for X-ray maps in a. a) ELL-14-02 (El Laco andesite), andesite with fine trellis textured ilmenite lamellae visible in BSE image and X-ray map for Ti, red box surrounds the magnified view of the exsolution domain. b and c) LAS-14-07 (Láscar dacite), ilmenite exsolution lamellae visible in BSE and RL are found in some grains (b) and are absent in others (c).

Kiruna magnetite X-ray maps

Little chemical variation was observed in the X-ray maps for any of the Kiruna magnetite samples. The ore magnetite from the deposits in the Kiruna area display zones of elevated Al and Si that correlate with each other (see Fig. 3b, c and Fig. 4c). Many of the larger (>100 μm) ore and host rock magnetite grains display equally distributed spots of elevated Al throughout the grains that is not observed in the Si, V, Ca, or Ti X-ray maps (see Fig. 3b, e and 4a). These elevated Al spots are displayed in BSE images as darker spots (see Fig. 4a). The magnetite from the granite intrusive at Kiirunavaara (Fig. 3g), and the footwall magnetite at Rektorn, display elevated contents of Si, Al, Ca, and Ti can be found along structures that follow the typical shape of spinel exsolution lamellae (Fig. 4e). The syenite sample of the Kiirunavaara mine revealed rims depleted in V (Fig. 3h). The Rektorn ore X-ray map has the most distinct chemical variations due to the presence of hematite that correlates to elevated Ti and V found in the zones darker in BSE (see Fig. 4d).

El Laco magnetite X-ray maps

The ore magnetite-kenomagnetite crystal from ELL-14-04 that was mapped did not have a porous core that was observed in other grains from that sample and did not show any variation in chemistry. However, the adjacent grains in the X-ray map have porous cores which display elevated Si, Ca, and Al with growth zoning (Fig. 5a). The X-ray maps of the ELL-14-05 magnetite, with concentric growth zoning visible in BSE imaging, revealed increasing Si, Ca, and Al content towards the core of the grain (Fig. 5b). Magnetite grains from a vein in the lower levels of the ore (ELL-14-06) displays growth zoning in Si and Ca with highest concentrations in the core. The martite (i.e.,

hematite) replaced portions of the magnetite show lowest concentrations of trace elements (Fig. 5c). The El Laco andesite magnetite grain shows elevated Ti in the ilmenite exsolution lamellae that are visible in BSE imaging and reflected light microscopy (Fig. 6a). The Láscar dacite magnetite grain chosen for the X-ray map shows overall elevated Ti (Fig. 6b) compared to the El Laco magnetite.

Trace element chemistry of Kiruna magnetite

The iron content of magnetite for the ore, host, and intrusive rocks at Kiruna were slightly lower than the ideal stoichiometric value (72.4 wt.% Fe) with EPMA results ranging from 69.4 and 70.8 wt.% Fe (Table 2). The iron content for analyses on samples that were identified as hematite (REK-10-01 and REK-10-04) was distinctly lower than the magnetite and ranged from 63.8-68.5 wt.% Fe. All of the magnetite grains from the Kiruna area, including the magnetite-apatite ore, host rocks and related felsic intrusive rocks, are overall chemically homogeneous and contain low trace element concentrations (i.e., <500 ppm). The V concentrations, and locally the Si content, in the magnetite are generally higher than the other trace elements with concentrations around 0.1 wt % and up to 0.2 wt %. The Ti contents are very low for magnetite with concentrations generally <50 ppm. The Kiirunavaara D-ore magnetite grains have higher Si and V contents than the B-ore magnetite. The degree of alteration seems not to affect the chemical composition of the footwall magnetite at Kiirunavaara; both samples contain similar, and low, trace element concentrations. The hanging wall magnetite at Kiirunavaara has higher Si and lower V compared to the footwall magnetite. The magnetite from the syenite, aplite, and granite intrusive rocks at the Kiirunavaara deposit shows some variation in chemistry; particularly, the syenite magnetite, which has the highest Si content, and the

aplite magnetite has the highest V content. The Nukutusvaara ore magnetite grains have higher Ti content than Kiirunavaara, Tuollavaara and Rektorn. The Rektorn ore shows the most chemical variability visible in BSE, X-ray maps and reflected light described earlier; trace element results confirms that the hematite ore contains elevated Ti and V and is depleted in Ni and Ga relative to the magnetite ore (see Fig. 8).

Trace element chemistry of the El Laco magnetite

The Fe concentrations for the magnetite grains at the Laco Sur ore are 67.25-70.4 wt % Fe. The magnetite grain that displays concentric growth zoning (ELL-14-05) showed decreasing Si, Ca and Al towards the rim of the grain in the X-ray maps and trace element analysis confirms this (Fig. 7a, see Fig. 5b for analysis locations). In addition, Mg and Ce as well as the high field strength elements (HFSE) Y, Nb, and Th and the large ion lithophile elements (LILE) and Sr follow a similar pattern; with a systematic decrease towards the rim. A euhedral magnetite grain from the magnetite vein referred to above (ELL-14-06) was analyzed 10 times across the grain; this produced a chemical cross-section of the grain (Fig. 7b, see Fig. 5c for spot locations). This cross-section shows that the core is enriched in Si and Ca, already detected in the X-ray maps (see Fig. 5c), as well as Mn, Sr, Y, Nb, Ce and Th. Five of the analyses (A, C, F, I and J) were done on magnetite that has been altered to martite and these analyses show lower concentrations of each trace element that defines the zoning patterns in the magnetite. Other trace element concentrations, such as Ti, V, Ni, Sn, Ga, and V do not show variations between the pure magnetite and areas replaced by martite (see Fig. 8, 9, 10 and 11).

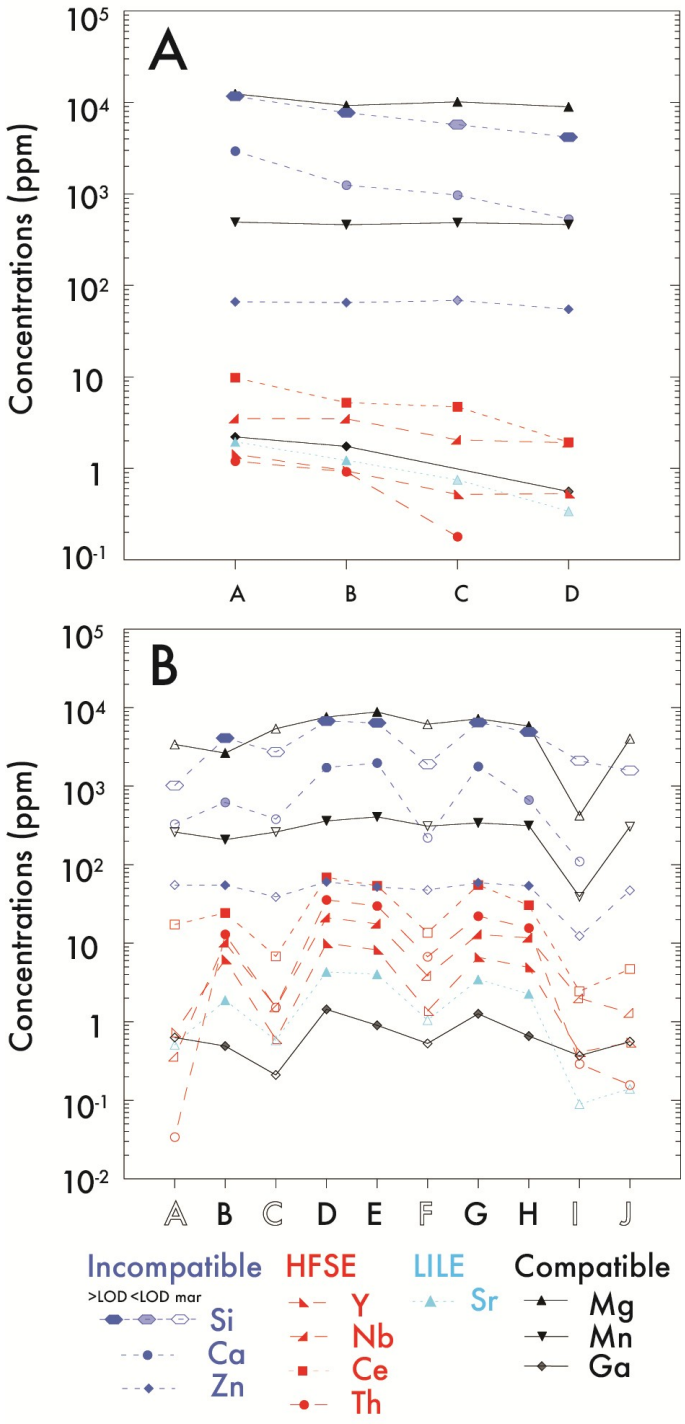

Fig 7. Trace element zoning patterns in magnetite grains from the Laco Sur magnetite ore. a) ELL-14-05 ore sample (see Fig. 5c for laser spot locations) and b) ELL-14-06 ore sample (see figure 5c for laser spot locations). Faded symbols represent analysis that are <LOD and open symbols are analysis of martite (pseudomorphic replacement of magnetite to hematite). See text for details.

The host andesite at El Laco and the dacite from the Láscar volcano have lower Fe content with concentrations ranging from 59.4-65.6 wt.% Fe and 56.8-61.4 wt % Fe, respectively. This is possibly due to the presence of unavoidable ilmenite exsolution lamellae and overall much higher Ti and other trace element concentrations. The andesite host rock magnetite at El Laco contains elevated concentrations of Al, P, Ti, V, Cr, Mn, Zn, Nb and Ba compared to the ore magnetite, a similar pattern to that described by Dare et al. (2015) (see Figure 13). The dacite magnetite from Láscar had the highest trace element content with the addition of elevated Mg, Si, Ca and Sn compared to the andesite magnetite.

Mineral deposit-type discrimination diagrams

Loberg and Horndahl (1983) studied the geochemistry of magnetite in different types of iron ores, including magnetite-apatite, titaniferous, and BIF, including samples from the Kiruna and Bergslagen (southeast Sweden) regions and some samples from Iran and Chile. Fe, Ti, V, and Ni, were used to create several discrimination plots. The Ni vs. V diagram (Fig. 8a) show very homogeneous compositions of these two elements for each individual sample, but there are significant variations between samples from each locality and between El Laco and Kiruna samples. In contrast, the Ti concentrations are rather heterogeneous and vary considerably even within each sample (Fig. 8b and c). Distinct chemical variations between the Kiirunavaara ore (lowest Ti contents), the Per Geijer ores near Kiruna (highest Ti concentrations), and the El Laco ores are observed.

-

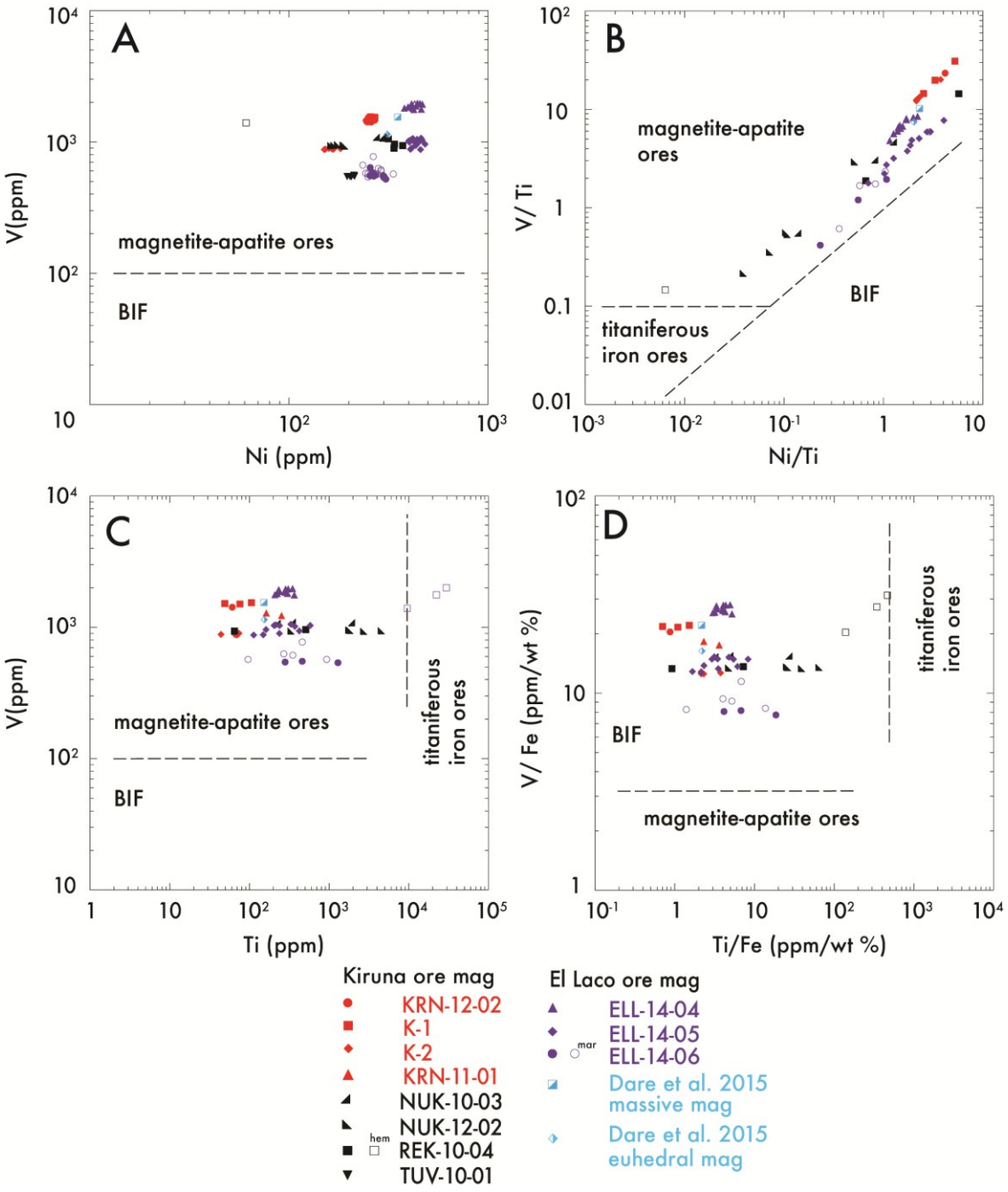

Fig. 8. Magnetite discrimination plots by Loberg and Horndahl (1983) containing fields for magnetite-apatite ores and BIF (a - d) and titaniferous iron ores (b - d) with samples from this study plotted. a) V (ppm) vs. Ni (ppm). b) V/Ti vs. Ni/Ti. c) V (ppm) vs. Ti (ppm) and d) V/Fe (ppm/wt %) vs. Ti/Fe (ppm/wt %). The symbols used here for the ore magnetite are the same for the remaining figures in this paper. The open symbols represent analysis of hematite or martite. See text for details.

Dupuis and Beaudoin (2011) also proposed several empirical discrimination diagrams for magnetite from various deposit types including BIF, IOCG, magnetiteapatite (Kiruna-type), porphyry-Cu, skarn and Fe-Ti-V layered mafic intrusion deposits (Fig. 9). The two diagrams are based on Al + Mn + Ca (wt %) (Fig. 9a) and Ni/(Cr + Mn) (Fig. 9b) on the y-axis vs. Ti + V (wt %) on the x-axis. In these plots, the field of the Kiruna-type deposits was based on the analysis of magnetite from seven different magnetite-apatite locations around the world, including Kiruna and El Laco (Dupuis and Beaudoin, 2011). It should be noted that the samples chosen from Kiruna and El Laco are different to those used in the present study. These diagrams are suggested for usage during mineral exploration to fingerprint different styles of mineralization using magnetite chemistry. We chose the version of the first diagram (Fig. 9a) modified by Nadoll et al. (2014), who eliminated Ca from the y-axis component, because plotting with or without Ca made little difference in where our data plotted because many of the Ca contents are low or below the LOD.

In Figure 9a, the majority of the Kiruna and El Laco magnetite analyses from the present study plot below and to the left of the proposed Kiruna field and none of the data plot within that field. Magnetite from the Rektorn ore with elevated Ti plot within the Fe-Ti, V deposit field. Magnetite from the stratabound ore of El Laco, plots non-uniquely in the IOCG and porphyry copper fields, situated above and to the left of the Kiruna-type field.

In Figure 9b, about one third of the magnetite-apatite ore analyses plot within the Kiruna-type field but the majority plots within the IOCG field. The Ti-rich hematite from

the Rektorn ore plots within the Fe-Ti, V deposit field. The Ti-poor magnetite from the Rektorn ore plots above the IOCG and Kiruna-type fields.

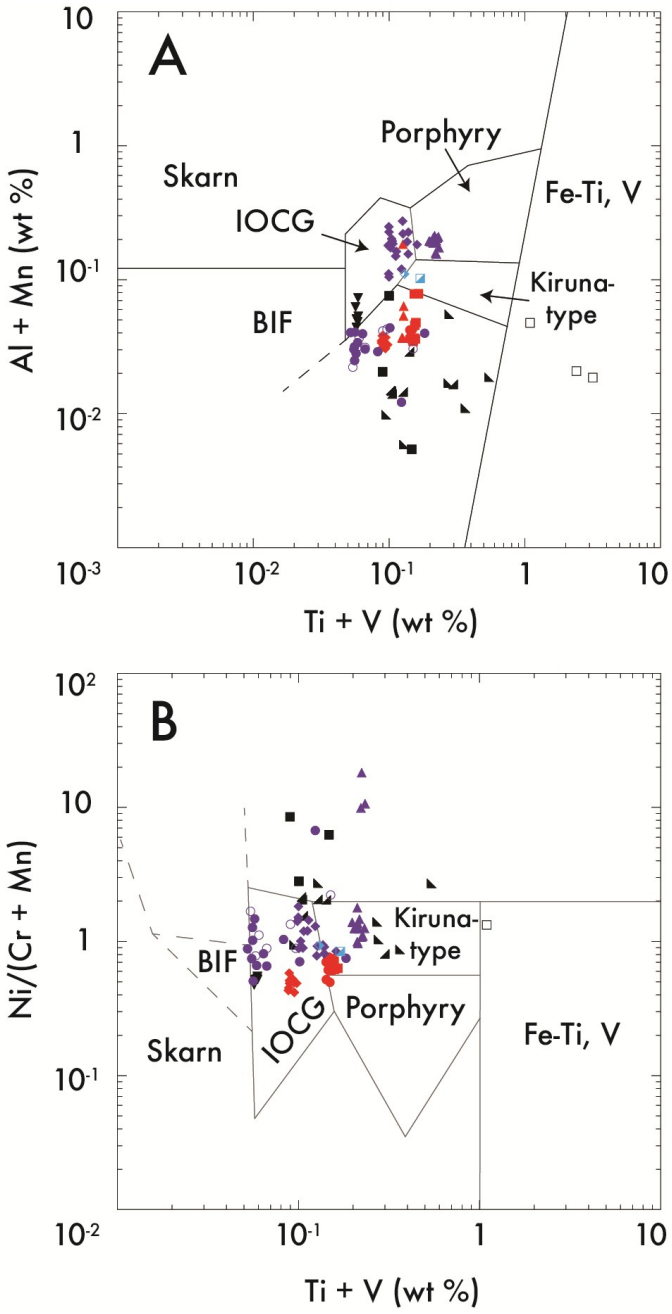

Fig. 9. Magnetite discrimination plots for various ore deposit-types by Dupuis and Beaudoin (2011) and modified by Nadoll et al. (2014) with samples from this study

plotted. a) Al + Mn (wt %) vs. Ti + V (wt %). b) Ni/(Cr + Mn) vs. Ti + V (wt %). See text for details.

Knipping et al. (2015) presented a discrimination diagram to distinguish Kiruna-type deposits from porphyry, IOCG and Fe-Ti, V deposits based on the Cr and V content of the magnetite (Fig. 10). The Kiruna-type deposits were defined as having low Cr content (<~100ppm) and high V content (>~500ppm). Some of the magnetite analyses from the Kiruna and El Laco magnetite-apatite ores in this study have higher Cr content than previously reported (Dare et al., 2015) and plot above the Kiruna-type zone with similar Cr and V content as magnetite from IOCG and porphyry deposits.

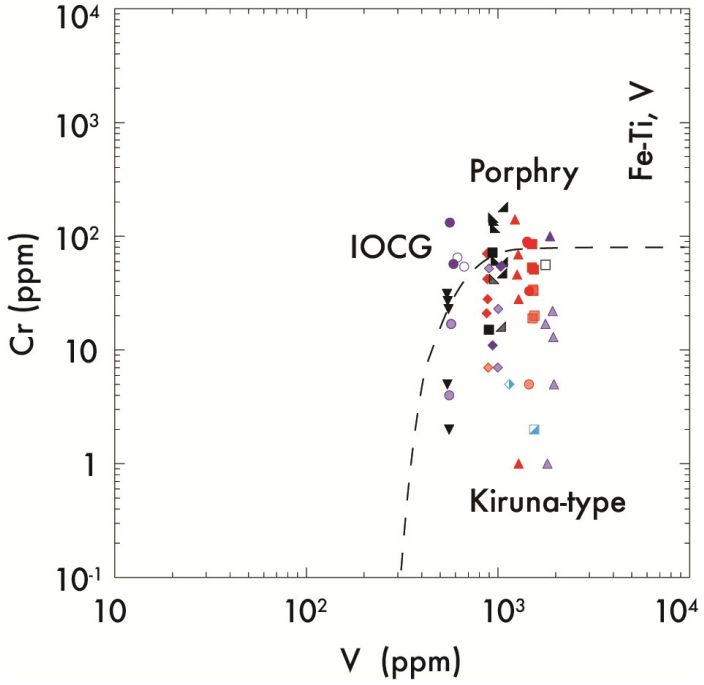

Fig. 10. Cr vs. V plot discriminating Kiruna-type from other ore deposit proposed by Knipping et al. (2015). Many of the magnetite grains from the Kiruna and El Laco magnetite-apatite ores in this study contain higher Cr concentrations than suggested in this diagram. The faded symbols represent analysis of Cr that is <LOD. See text for details.

Magmatic vs. hydrothermal magnetite discrimination diagrams

Nadoll et al. (2015) proposed using the concentrations of Ti and V in magnetite to distinguish between hydrothermally and magmatically formed magnetite (Fig. 11). The justification for this diagram is that Ti and V are often found in high concentrations within magmatic magnetite and low concentrations within hydrothermal magnetite (Nadoll 2015; Knipping et al., 2015). Knipping et al. (2015) used this diagram as well, to support their magmatic-hydrothermal model for the formation of magnetite-apatite deposits, and drew magmatic and hydrothermal fields using magnetite data from Nadoll (2015). This is essentially the same plot used by Loberg and Horndahl (1983), to describe magnetite from magnetite-apatite deposits vs. BIF and titaniferous iron ores (see Fig. 8c), though used here to describe magnetite from different environments.

In Figure 11, magnetite data from the magnetite-apatite ores are plotted with the addition of the host rock magnetite to evaluate the fields drawn by Knipping et al. (2015). Most of the Kiruna magnetite data in the present study do not plot within the magmatic, hydrothermal, or overlapping magmatic-hydrothermal fields. The magnetite from the Kiirunavaara ore and host rocks has very low Ti concentrations that are at or below LOD and plot to the left of the overlapping magnetite-apatite field. The hematite portions of the Rektorn ore, with elevated Ti concentrations, plots in the magmatic magnetite field and the magnetite, with low Ti concentrations, plots in the overlapping field. The footwall magnetite at Rektorn plots within the hydrothermal magnetite field. The stratabound ore magnetite at El Laco plots within the overlapping magnetite-apatite field or to the left of this field. The host andesite magnetite at El Laco and the Láscar dacite magnetite, both with high Ti and V concentrations, plot at the far top right of the magmatic field.

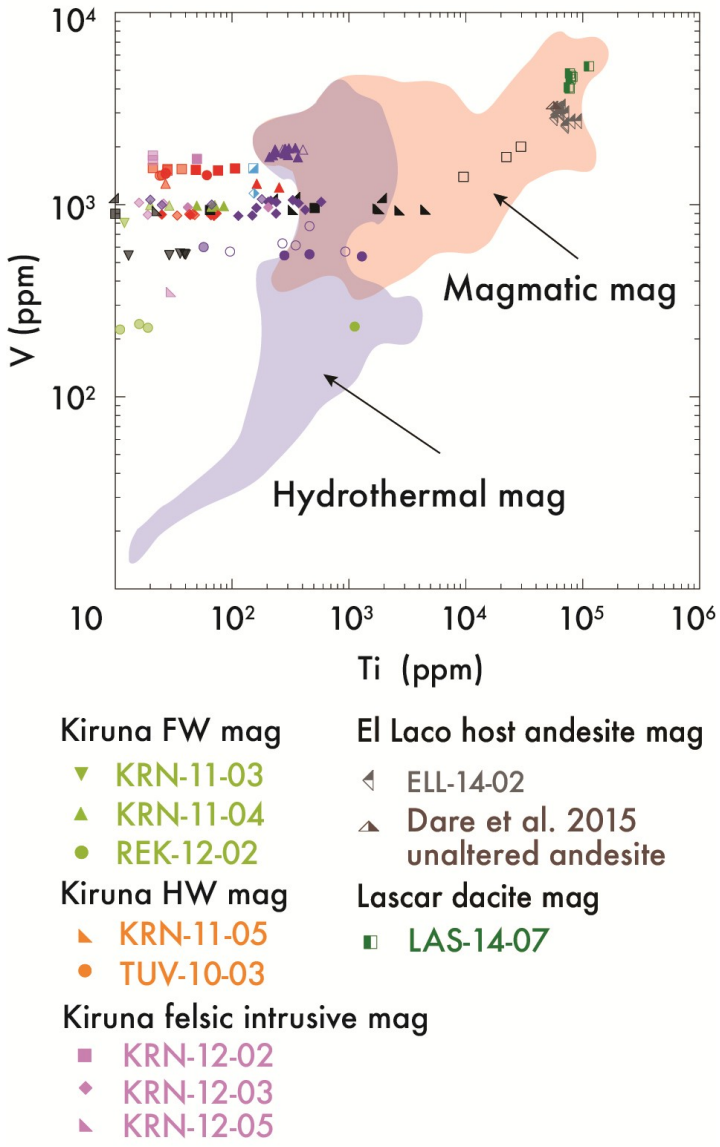

Fig. 11. V vs. Ti plot first proposed by Nadoll et al. (2015) with hydrothermal and magmatic magnetite fields drawn by Knipping et al. (2015). The plot suggests overall higher Ti and V concentrations in igneous magnetite with considerable overlap in Ti and V chemistry between hydrothermal and igneous magnetite. The symbols used for magnetite samples of the host rock and related intrusive bodies are the same for the remaining figures in this paper. The faded symbols here represent analysis of Ti that is <LOD. See text for details.

Dare et al. (2014) proposed an empirical discrimination diagram of Ti vs. Ni/Cr that shows there is a distinct chemical difference between magnetite that precipitated

from hydrothermal fluids and magnetite that crystallized from a magmatic melt (Fig. 12). Most of our magnetite data, including the host rock magnetite data for Kiruna, had one or more of the elements required for this plot below LOD. The Kiruna and Laco Sur ore magnetite as well as most of the Kiruna host rock and related intrusive magnetite, which occurs in igneous rocks, plots within the hydrothermal magnetite field proposed by Dare et al. (2014) due to the low Ti and Cr content of the magnetite. However, magnetite from

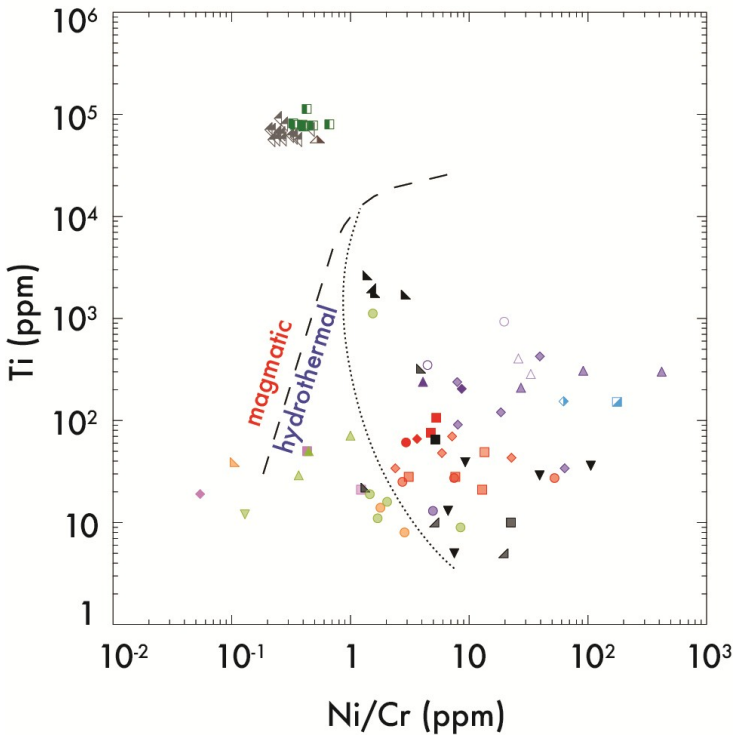

Fig. 12. Samples from this study plotted on the Ti vs. Ni/Cr plot proposed by Dare at al. (2014) to discriminate between magmatic and hydrothermal environments for magnetite formation. The majority of the magnetite data from Kiruna and the ore magnetite from El Laco had either Ni, Cr or Ti <LOD and these analysis are plotted here as faded symbols. The dotted line, placed in this study, separates the host and intrusive magnetite in Kiruna from the ore magnetite. See text for details.

the Kiruna host rocks and related intrusive rocks show a distinctly lower Ni/Cr ratio compared magnetite from the Kiruna and El Laco ore. A recent detailed study of El Laco by Velasco et al. (2016) showed that massive magnetite from the stratabound ore and the disseminated magnetite related to the early alkaline-calcic alteration, and of undisputable hydrothermal origin, plot in both the magmatic and hydrothermal fields.

Trace element variations for magnetite were plotted on a multi-element diagram proposed by Dare et al. (2014) that was modified in this present study to leave out trace elements not commonly found in magnetite and not measured in this study (e.g., Zr, Ge, W, Sc, and Mo from the Kiruna analyses and Zr, Hf, Sc from the El Laco analyses) (Fig. 13). Elements are normalized to the bulk continental crust data from Rudnick and Gao (2003). This diagram shows there to be distinct trace element chemical patterns between magnetite from a magmatic origin and from magnetite that could be from a high-T or low-T hydrothermal origin. Magmatic magnetite patterns from Dare et al. (2014) are based on data from the El Laco andesite and the Bushveld complex as well as magnetite from I-type granite. The high-temperature hydrothermal (500-700°C) region was defined using analytical results for magnetite from nine different IOCG deposits. The low-temperature hydrothermal zone (<500°C) is based on magnetite from iron-rich skarns, Ag-Pb-Zn veins and BIFs. Average results from each magnetite sample in the present study were used for this plot (Appendix III); this made the diagram easier to read and interpret.

The trace element patterns for the magnetite-apatite ores at Kiruna are most similar to the high-temperature hydrothermal magnetite zone (Fig. 13a). Magnetite within the host and intrusive rocks in Kiruna for the most part follows a similar trace element

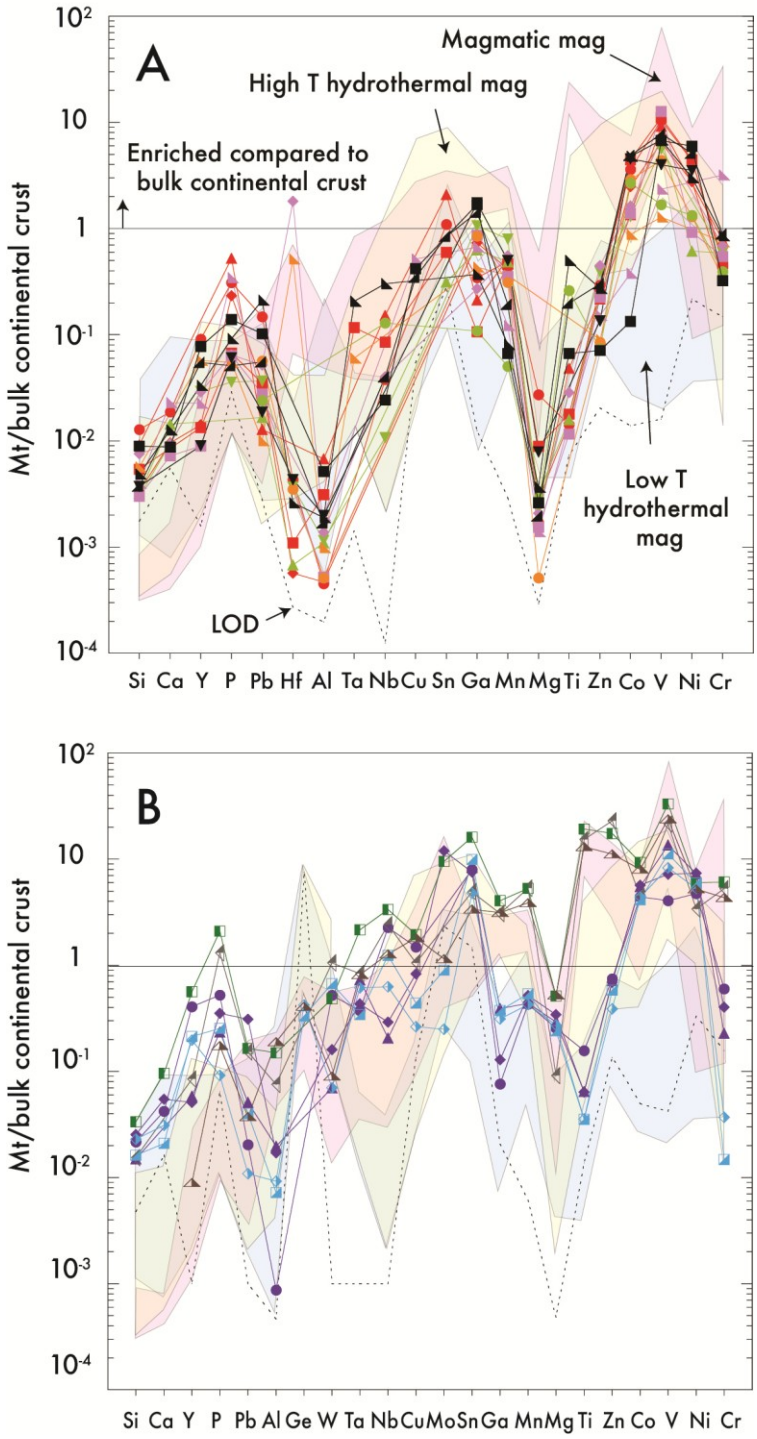

Fig. 13. Samples from this study on a multi-element variation diagram proposed by Dare et al. (2014) showing trace elements in magnetite normalized to bulk continental crust from Rudnick and Gao (2003). Zones showing the proposed compositional patterns of magnetite from magmatic (pink), high- (yellow) and low- (blue) temperature hydrothermal environments are shown. Each zone was adjusted in this study to accommodate elements that were not analyzed. See text for details.

pattern to the ore magnetite, in the high-temperature hydrothermal zone, though with overall lower trace element concentrations than the ore magnetite. None of the host magnetite at Kiruna resembles the proposed magmatic trend even though they are hosted in volcanic rocks, except peaks in Hf in magnetite from the Kiirunavaara hanging wall and the syenite sill in the footwall at Kiirunavaara.

The trace element patterns for the Laco Sur ore magnetite show similar trends as the high-temperature hydrothermal pattern, with high Mg trending into the magmatic field and low Ga trending into the low-temperature hydrothermal field (Fig. 13b). The andesite host rock magnetite at El Laco and the Láscar dacite magnetite follow the magmatic magnetite trend. All magnetite from El Laco and Láscar analyzed in the present study, including the andesite and dacite magnetite, shows higher concentrations of Si, Ca, Y and P than what is typical of the magnetite zones proposed in this plot, with the volcanic dacite magnetite containing the highest concentrations of these elements.

Discussion

The trace element geochemistry of magnetite depends on the content of the element in the fluid, melt or aqueous, source and the capability of the host mineral to accept the trace element in its structure, which can depend on variables such as the temperature or the redox state. Thus, discrimination diagrams could only be used when the host mineral is not saturated in the contained element and there is no competing phases that could host it; otherwise, the trace element composition should be controlled by the partitioning coefficient (K_D) between both minerals. Also, drop in the temperature or fluctuating conditions can lead to exsolution of separate phases, which also has to also be taken into account. Furthermore, the accurate use of discrimination diagrams should

also exclude the presence of nanoinclusions, which cannot always be removed during the LA-ICPMS data reduction.

The use of mineral deposit-type discrimination diagrams

The Loberg and Horndahl (1983) diagrams (see Fig. 8) worked effectively plotting the magnetite-apatite ores within the appropriate fields. These diagrams contain very broad discrimination fields, which accounts for the chemical variation observed in the ore magnetite. In the case of the Rektorn ore, a higher Ti concentration in the hematite ore suggests that this ore body formed at higher temperatures and more reducing conditions (see Lindsley, 1976) or from a source richer in Ti. Regardless, the data suggest that this mineralization had a different genesis or a source of different composition, or both, from the other magnetite-apatite ores at Kiruna.

The Dupuis and Beaudoin (2011) diagrams (see Fig. 9) have narrow discrimination fields. The magnetite-apatite data from this study do not plot within the proposed Kiruna-type discrimination field and overlapped significantly with other deposit types such as IOCG and porphyry-Cu. There is too much overlap in magnetite chemistry from the Kiruna-type magnetite-apatite mineralization and the other types of deposits for this diagram to work effectively. For instance, if these diagrams were to be used in mineral exploration using magnetite as an indicator mineral it would be impossible to distinguish magnetite sourced from magnetite-apatite ores from magnetite from IOCG or Cu-porphyry deposits. Thus, and based on the results from the present study, the Kiruna field needs to be significantly modified or removed from the diagram. Since many of the magnetite-apatite ore analyses plot within the IOCG field, this could have implications

for a common connection between these two styles of mineralization, or alternatively, could reveal a flaw in the reasoning behind the rationale for these diagrams.

The Knipping et al. (2015) Cr/V discrimination diagram was used to fingerprint how Kiruna-type deposits have distinct Cr and V contents from porphyry, IOCG, and Fe-Ti, V deposits (see Fig. 10). The rationale behind the Kiruna-type field in this diagram is that higher V content relates to the high formational temperatures. The low Cr content of Kiruna-type magnetite is explained by its high K_D into the fractionation of augite or, and deemed more likely, the high mobility of the Cr^{6+} into oxidized fluids that transported Cr out of the magnetite-apatite ore forming system. As mentioned above in the results, several of the magnetite analyses from the Kiruna and El Laco ores in this study have higher Cr contents than previously reported for those localities (Dare et al., 2015). Assuming the rationale behind the diagram is valid, then higher Cr content observed in the ore magnetite in the present study suggests Cr, and possibly other elements that are mobile in hydrothermal fluids such as Si, Ca and LILE, were not transported out of the system but were incorporated into the magnetite.

The use of magmatic vs. hydrothermal magnetite discrimination diagrams

Nadoll et al. (2015), further used by Knipping et al. (2015), used V and Ti concentrations to discriminate between magmatic and hydrothermal magnetite (see Fig. 11). Based on the magnetite data from the present study, and those of Velasco et al. (2016), it is clear that magnetite from the magnetite-apatite deposits has extremely variable V and Ti concentrations. Thus, many of the magnetite samples here plot outside the fields on this diagram, questioning the integrity of the plot. Dare et al. (2014) proposed another diagram that discriminates between magmatic and hydrothermal

magnetite using Ti and Ni/Cr concentrations (see Fig. 12). Although the magnetite from magnetite-apatite ores plot within the hydrothermal magnetite field, this does not necessarily verify that they formed hydrothermally, as has been shown by Velasco et al. (2016). Probably, these empirical diagrams are too simple to distinguish and the Ti and Ni/Cr ratios do not only depend on the precipitation from silicate or aqueous fluids or needs additional constraints and/or adjustments.

Magnetite that crystallized from a melt of unique composition may contain lower Ti concentrations than is normal for igneous magnetite. The multi-element variation diagrams proposed by Dare et al. (2014) have fields that overlap significantly with each other and none of the analyses from the present study plot perfectly within one field, leaving ambiguity regarding the utility of that diagram (see Fig. 13). Furthermore, it must be considered that it is not possible to directly compare the trace element patterns between immiscible melts, such as a silicate melt and a presumable iron rich-melt, since during phase separation, the K_D irregularly distributes the elements between them.

Magnetite chemistry at Kiruna

The magnetite studied from the Kiruna magnetite-apatite ores is generally very homogenous and shows few textural and chemical variations. It is strongly suggested that the original trace element chemistry of the magnetite in the Kiruna ore and their host rocks were affected by subsequent hydrothermal alteration and metamorphism. The rocks at Kiruna have undergone widespread hydrothermal alteration (Westhues et al., 2016) and up to greenschist facies metamorphism (Bergman et al., 2001); where widespread re-crystallization of magnetite can occur (Dahl 1979). The X-ray maps of the Kiruna magnetite grains revealed areas of increased Si and Al that often are correlated with each

other. These zones are blotchy and random and could likely be a result of metasomatic alteration. The high-Al domains are most prominent in the larger grains of the ore and footwall magnetite could be nanoinclusions of an Al-rich mineral or may also be the result of metasomatic alteration.

Hydrothermal titanite is widespread in the Kiruna ore (Romer et al., 1994; Storey et al., 2007) and indicates that the hydrothermal fluids were rich in Ti. Titanite has been dated to be just younger, though with overlapping error (1876 ± 9 Ma, Romer et al., 1994) than the volcanic rocks around Kiirunavaara (1890 ± 90 Ma, Cliff et al., 1990). Recent in situ dating confirmed these time constraints and it is suggested that the titanite ages reflect the metasomatic alteration overlapping with the ore formation (Westhues et al., 2016).

Although the magnetite chemistry of the Kiruna rocks are very similar in most elements (see Fig. 11 and 13), the Ni/Cr vs Ti plot after Dare et al. (2014) (see Fig. 12) revealed, a distinct difference in the Ni/Cr content of the magnetite from the magnetite-apatite ores and the host rocks/related felsic intrusive rocks: The latter have a more similar Ni/Cr content as the El Laco host rocks but with lower Ti concentrations. This may suggest that, before subsequent intensive alteration of the host rocks, primary magnetite may have had a more similar composition to the magnetite in andesite at El Laco. Because the chemistry of the magnetite studied in the rocks at Kiruna show indications of being subsequently altered by metasomatism, it is difficult to draw any conclusive arguments on how the magnetite-apatite ores formed through the utilization of magnetite discrimination diagrams.

Magnetite chemistry at El Laco

The magnetite from El Laco is much younger than at Kiruna and has not been affected by metamorphism, but most of it likely has undergone various degrees of hydrothermal alteration (Tornos et al., 2016). There are clear chemical differences at El Laco in the magnetite ore and magnetite from the andesite host and the dacite sample from the nearby Láscar Volcano. The andesite and dacite samples have similar trace element chemistry with signatures that plot as igneous magnetite on proposed discrimination diagrams (see Figs. 10, 11 and 12) and have clear exsolution textures common in Ti-rich magmatic magnetite crystallized in hot and reduced settings (Mehdilo and Irannajad 2010). The Láscar dacite magnetite has elevated trace element concentrations compared to the El Laco andesite magnetite. This may indicate that the source melt of the volcanic rocks at Láscar has a different composition from the El Laco volcanic rocks or certain physicochemical parameters were different such as lower fO_2 of the melt at Láscar during magnetite crystallization.

The ore magnetite at El Laco shows clear zonation patterns in BSE and X-ray maps, which have also been described by previous authors (Fig. 5) (e.g., Velasco and Tornos 2011; Dare et al., 2015; Velasco et al., 2016). The centers of the magnetite crystals show elevated concentrations of Si, Ca and LILE (Fig. 7) compared to the outer regions; these elements are considered to be incompatible and highly mobile in hydrothermal environments (Dare et al., 2014; Nadoll et al., 2014). However, the cores also show elevated concentrations of Mg, Al and Mn, elements that are considered compatible and generally immobile in hydrothermal fluids as well as HFSE (Y, Nb, Ce and Th), which are incompatible during partial melting but not as readily mobile in hydrothermal environments (McCulloch and Gamble 1991, Blake 1992). Also, the ore

magnetite were reported as being “enriched” in elements that are highly mobile in hydrothermal fluids, though concentrations of these elements are not higher than was detected in the unaltered andesite magnetite or the Láscar dacite magnetite (see Fig. 13 and Appendix III).

If the El Laco ores formed through metasomatic replacement of the andesite host rocks as proposed by Dare et al. (2015), one would expect elevated LILE concentrations in the magnetite; however, the HFSE and especially incompatible elements are not readily mobile in hydrothermal fluids and one would expect them to be in lower concentrations than the LILE and not behaving the same way during magnetite crystallization. Dare et al. (2014) describes iron-rich skarn magnetite as having element concentrations and euhedral zoning similar to the El Laco magnetite. However, the elements that define growth zones in the iron-rich skarn magnetite are not enriched and depleted in the same layers, suggesting quick changes in the composition of the igneous/aqueous fluid pulses that crystallized the magnetite. Also, elements such as V and Ni are zoned in the iron-rich skarn magnetite (Dare et al., 2014) and this is not observed in the El Laco magnetite suggesting not all elements were fluctuating during magnetite growth, as would be the case during growth from hydrothermal fluids.

Looking closely at the zoning chemistry of the El Laco ore magnetite, a combination of incompatible elements, compatible elements, LILE and HFSE behave the same way during magnetite crystal growth (i.e., they are all found either elevated or depleted in the same layers). Formation of magnetite from a crystallizing iron oxide melt at El Laco is consistent with the presence of magmatic textures, the stable isotope geochemistry and the presence of melt inclusions with evidences of melt immiscibility; it

is also difficult to envisage the circulation of iron-rich hot brines at shallow depths (Tornos et al., 2016). Thus, the chemistry of the magnetite at El Laco can be explained by magnetite crystallizing from an iron-rich melt that is initially enriched in the elements involved in the zonation patterns with periodic replenishment from the source melt during magnetite growth with less replenishment over time. Or, and more likely, the crystallization of magnetite during fluctuating redox conditions (fO_2), fluid content and temperature of the melt. As the iron-rich melt moved closer to the surface the system would have shifted from a reduced environment to an oxidized environment. In an oxidized system there is an increase of Fe^{3+}, which occupies octahedral sites in magnetite, inhibiting the incorporation of other elements, such as Ti, that were present in the iron-rich melt (Buddington and Lindsley 1964). It should also be noted that spherical to spheroidal magnetite particles have been described from more friable ore than the samples used in the study, textures that can only be explained by rapid cooling of an iron-rich melt (Henríquez and Martin 1978; Nyström et al., 2016).

Conclusions

After a critical evaluation of empirical magnetite discrimination diagrams using newly obtained data on the trace element composition of magnetite from precisely known geographic and geologic locations (encompassing the Kiruna and El Laco magnetite-apatite ores and their associated hydrothermally altered host rocks) the following conclusions can be drawn for practical usage in determining the environment from which magnetite crystallized (i.e., hydrothermal or magmatic):

1) Only the earlier diagrams by Loberg and Horndahl (1983), with very broad discrimination fields, allowed effectively plotting the magnetite-apatite ores within the

appropriate field. The more recent discrimination diagrams proposed by Dupuis and Beaudoin (2011) and Knipping et al. (2015), with more constrained fields, need to be adjusted if they are to include the Kiruna-type magnetite;

2) The Cr content from Kiruna-type magnetite reached higher concentrations than previously reported by Knipping et al. (2015), this calls into questions the validity of the Cr-V plot as well as conclusions drawn from using this plot to support the genetic model for magnetite-apatite deposits that is proposed by these authors;

3) The magmatic vs. hydrothermal discrimination diagram for magnetite by Knipping et al. (2015) needs modification as many of the data from the present study did not plot within either of the proposed fields;

4) The magmatic vs. hydrothermal magnetite diagram by Dare et al. (2014) had limited use because most of the data collected had non-detectable Cr, Ni, or Ti concentrations. The data below LOD, however, had to be plotted in order to evaluate this diagram. The indisputably igneous magnetite (e.g., El Laco andesite and Láscar dacite) effectively plotted within the magmatic magnetite field. The magnetite-apatite ores from El Laco and Kiruna and host rock magnetite at Kiruna all plot within the hydrothermal field. The host rock magnetite has distinctly lower Ni/Cr ratio than magnetite from the magnetite-apatite ores.

5) The multi-element variation diagrams proposed by Dare et al. (2014) only work if the magnetite-apatite ores are actually of hydrothermal origin, and do not work on magnetite that has undergone subsequent metamorphism and/or metasomatic alteration such as at Kiruna.

After reviewing the chemistry and textures of the magnetite from the Kiruna and El Laco magnetite-apatite ores and their host rocks the following conclusions can be made:

1) It is likely that the magnetite at Kiruna is largely influenced by subsequent metamorphism and/or metasomatic alteration. Whether the magnetite-apatite ores, which show hydrothermal signatures on the diagrams discussed above, originated from hydrothermal fluids or formed later through post-ore metamorphic or metasomatic alteration cannot be determined using magnetite chemistry alone; and

2) The magnetite from magnetite-apatite ores at El Laco have chemical zonations that appear similar to Fe-rich skarns (Dare et al., 2015), though there are very distinct differences in the zonation patterns. Observations of the chemical zonation patterns in the El Laco magnetite that do not correlate with iron-rich skarn magnetite include: a) The El Laco ore magnetite has zonations of compatible, LIL and HFS elements that are all elevated or depleted in the same crystal layers; and, b) some compatible elements are homogenous across the magnetite grains (i.e., V and Ni). With these observations, we propose the magnetite at El Laco is indicative of having crystallized from a volatile-rich iron-oxide melt that was fluctuating in physiochemical conditions rather than from replacement of the host rocks by pulses of hydrothermal fluids.

Acknowledgements

We would like to thank the Natural Sciences and Engineering Research Council of Canada (NSERC) discovery grant to JMH. The contribution of FT has been funded by the project SEIDI 2014 CGL2014-55949-R. Thanks to LKAB and Compañía Minera del Pacífico for help in logistics, and permission to sample and granting access to the mine

sites. We thank the reviewers (P. Williams and N. Oliver) for thorough and constructive criticism of the original manuscript. Thanks also to B. Lehmann for his review and editorial additions, and handling of this paper.

References

Alva-Vadivia LM, Rivas ML, Goguitchaichvili A, Urrutia-Fucugauchi J, Gonzalez JA, Morales J, Gómez S, Henríquez F, Nyström JO, Naslund RH (2003) Rock-magnetic and oxide microscopic studies of the El Laco ore deposits, Chilean Andes, and implications for magnetic anomaly modeling. International Geology Review 45:533-547

Barton MD, Johnson DA (1996) Evaporitic-source model for igneous-related Fe oxide-(REE-Cu-Au-U) mineralization. Geology 24:259-262

Barton MD, Johnson DA (2004) Footprints of Fe-oxide(-Cu-Au) systems. SEG 2004: Predictive Mineral Discovery Under Cover. Centre for Global Metallogeny, Spec Pub 33:112-116

Bergman S, Kubler L, and Martinsson O (2001) Description of regional geological and geophysical maps of northern Norrbotten County (east of the Caledonian Orogen). Sveriges Geologiska Undersokning 56:110

Blake KL (1992) The petrology, geochemistry and association to ore formation of the host rocks of the Kiirunavaara magnetite-apatite deposit, northern Sweden. PhD thesis. University of Wales College of Cardiff

Buddington AF, Lindsley DG (1964) Iron-titanium oxide minerals and synthetic equivalents. J Petrol 5(2):310-357

Chamberlain SC, Robinson GW, Lupulescu M, Morgan TC, Johnson JT, deLorraine WB (2008) Cubic and tetrahexahedral magnetite. Rocks & Minerals 83(3):224-239. Doi: 10.3200/RMIN.83.3.224-239

Crohn PW, Moore DH (1984) The Mud Tank carbonatite, Strangways Range, central Australia. Journal of Australian Geology & Geophysics 9:13-18

Dahl PS (1979) Comparative geothermometry based on major-element and oxygen isotope distributions in precambrian metamorphic rocks from southwestern Montana. American Mineralogist 64:1280-1293

Dare SAS, Barnes S-J, Beaudoin G, Méric J, Boutroy E, Potvin-Doucet C (2014) Trace elements in magnetite as petrogenetic indicators. Miner Deposita 49:785-796

Dare SAS, Barnes S-J, Beaudoin G (2015) Did the massive magnetite "lava flows" of El Laco (Chile) form by magmatic or hydrothermal processes? New contraints from magnetite composition by LA-ICP-MS. Miner Deposita 50:607-617

Dupuis C, Beaudoin G (2011) Discriminant diagrams for iron oxide trace element fingerprinting of mineral deposit types. Miner Deposita 46:319-335.

Dymek RF, Owens BE (2001) Petrogenesis of apatite-rich rocks (nelsonites and oxide-apatite gabbronorites) associated with massif anorthosites: Econ Geol 96:797-815

Edfelt A, Armstrong RN, Smith M, Martinsson O (2005) Alteration paragenesis and mineral chemistry of the Tjarrojakka apatite-rion and Cu (-Au) occurrences, Kiruna area, northern Sweden. Miner Deposita 40:409-434

Frietsch R (1978) On the magmatic origin of iron ores of the Kiruna type. Econ Geol 73:478-485

Frietsch R, Perdahl Jan-Anders (1995) Rare earth elements in apatite and magnetite in Kiruna-type iron ores and some other iron ore types. Ore Geology Reviews 9:489-510

Geijer P (1910) Igneous rocks and iron ores of Kiirunavaara, Luossavaara and Tuollavaara. Scientific and practical researches in Lapland arranged by the Luossavaara-Kiirunavaara Aktiebolag - Geology of the Kiruna district, 2: Stockholm, p. 278

Geijer P (1919) Recent developments at Kiruna, SGU, C 288, p. 23

Grigsby JD (1990) Detrital magnetite as a provenance indicator. Journal of Sedimentary Petrology 60(6):940-951

Groves DI, Bierlein FP, Meinert LD, Hitzman MW (2010) Iron oxide copper-gold (IOCG) through earths history: implications for origin, lithospheric setting, and distinction from other epigenic iron oxide deposits. Econ Geol 105:641-654

Hall JM, Fisher BE (1987) The characteristics and significance of secondary magnetite in a profile through the dike component of the Troodos, Cyprus, ophiolite. Canadian Journal of Earth Science 24:2141-2159

Hallberg A, Bergman T, Gonzalez J, Larsson D, Morris GA, Perdahl JA, Ripa M, Niiranen T, Eilu P (2012) Metallogenic areas in Sweden. Survey of Finland, Special Paper 53:139-206

Harlov DE, Andersson UB, Forster H-J, Nyström JO, Dulski P, Broman C (2002) Apatite-monazite relations in the Kiirunavaara magnetite-apatite ore, northern Sweden. Chemical Geology 191:47-72

Henríquez F, Martin RF (1978) Crystal growth textures in magnetite flows and feeder dykes, El Laco, Chile, Can Miner 16:581-589

Hildebrand RS (1986) Kiruna-type deposits - their origin and relationship to intermediate subvolcanic plutons in the Great Bear magmatic zone, northwest Canada: Econ Geol 81:640-659

Hitzman MW, Oreskes N, Einaudi MT (1992) Geological Characteristics and Tectonic Setting of Proterozoic Iron-Oxide (Cu-U-Au-Ree) Deposits. Precambrian Research 58:241-287

Jochum KP, Willbold M, Raczek I, Stoll B, Herwig K (2005) Chemical characterisation of the USGS reference glasses GSA-1G, GSC-1G, GSD-1G, GSE-1G, BCR-2G, BHVO-2G and BIR-1G using EPMA, ID-TIMS, ID-ICP-MS and LA-ICP-MS. Geostandards and Geoanalytical Research 29(3):285-302

Knipping JL, Bilenker LD, Simon AC, Reich M, Barra F, Deditius AP, Wälle M, Heinrich CA, Holtz F, Munizaga R (2015) Trace elements in magnetite from massive iron oxide-apatite deposits indicate a combined formation by igneous and magmatic-hydrothermal processes. Geochim Cosmochim Acta 171:15-38

Lindsley DH (1976) The crystal chemistry and structure of oxide minerals as exemplified by the Fe-Ti oxides. In Oxide minerals. Mineralogical Society of America, Short Course Notes 3:L-1 to L-60

Lindsley DH (1991) Oxide minerals: petrologic and magnetic significance. Reviews in Mineralogy, Volume 25, Stony Brook, New York, USA

LKAB (2015) Annual and sustainability report. http://www.lkab.com/en/. Accessed 30 April 2016

Loberg BEH, Horndahl A-K (1983) Ferride geochemistry of swedish precambrian iron ores. Miner Deposita 18:487-504

Martinsson O (1994) Greenstone and porphyry hosted ore deposits in northern Norbotten, NUTEK report nr 92-00752P: Luleå, p. 31.

Martinsson O (2004) Geology and metallogeny of the northern Norrbotten Fe-Cu-Au province: Society of Economic Geologists, Guidebook Series 33:131-148

Martinsson O, Billström K, Broman C, Weihed P, Wanhainen C (2016) Metallogeny of the northern Norrbotten ore province, northern fennoscandian shield with emphasis on IOCG and apatite-iron ore deposits. Ore Geology Reviews. doi: 10.1016/j.oregeorev.2016.02.011

McCulloch MT, Gamble JA (1991) Geochemical and geodynamical constraints on subduction zone magmatism. Earth and Planetary Science Letters 102:358-374

Mehdilo A, Irannajad M (2010) Applied mineralogical studies on iranian hard rock titanium deposit. Journal of Minerals & Material Characterization & Engineering 9(3):247-262

Mucke A, Younessi R (1994) Magnetite-Apatite Deposits (Kiruna-Type) Along the Sanandaj-Sirjan Zone and in the Bafq Area, Iran, Associated with Ultramafic and Calcalkaline Rocks and Carbonatites: Mineralogy and Petrology 50:219-244

Muller B, Axelsson MD, Bjorn O (2003) Trace elements in magnetite from Kiruna, northern Sweden, as determined by LA-ICP-MS. GFF 125:1-5

Nadoll P, Angerer T, Mauk JL, French D, and Walshe J (2014) The chemistry of hydrothermal magnetite: a review. Ore Geology Reviews 61:1-32

Naranjo JA, Henríquez F, Nyström JO (2010) Subvolcanic contact metasomatism at El Laco Volcanic Complex, Central Andes. Andean Geology 37:110-120

Naslund HR, Henríquez FJ, Nyström JO, Vivallo W, Dobbs F (2002) Magmatic iron ores and associated mineralization: examples from the Chilean High Andes and Coastal Cordillera; in Porter, T.M. (Ed.), Hydrothermal Iron Oxide Copper-Gold & Related Deposits: A Global Perspective, PGC Publishing, Adelaide, 2:207-226

Nyström JO, Henríquez F (1994) Magmatic features of iron ores of the Kiruna type in Chile and Sweden; ore textures and magnetite geochemistry. Econ Geol 89:820-839

Nyström JO, Billström K, Henríquez F, Fallick AE, Naslund H R (2008) Oxygen isotope composition of magnetite in iron ores of the Kiruna type in Chile and Sweden. Gff 130:177-188

Nyström JO, Henríquez F, Naranjo JA, Naslund HR (2016) Magnetite spherules in pyroclastic iron ore at El Laco, Chile. Am Mineral 101:587-595

Paton C, Hellstrom J, Paul B, Woodhead J, Hergt J (2011) Iolite: Freeware for the visualisation and processing of mass spectrometric data. Journal of Analytical Atomic Spectrometry 26:2508-2518. doi: 10.1039/c1ja10172b

Parák T (1975) Kiruna iron ores are not 'intrusive-magmatic ores of the Kiruna type'. Econ Geol 70:1242-1258

Park CF (1961) A magnetite “flow” in northern Chile. Econ Geol 56:431-436

Pollard PJ (2006) An intrusion-related origin for Cu-Au mineralization in iron-oxide-copper-gold (IOCG) provinces. Miner Deposita 41:179-187

Philpotts AR (1967) Origin of certain iron-titanium oxide and apatite rocks. Econ Geol 62:303-315

Ramanaidou E, Wells M, Belton D (2008) Mineralogical and microchemical methods for the characterization of high-grade banded iron formation-derived iron ore. SEG Reviews 15:129-156

Rhodes AL, Oreskes N (1999) Oxygen isotope composition of magnetite deposits at El Laco, Chile: evidence of formation from isotopically heavy fluids. Soc of Econ Geol, Spec Pub 7:333-351

Richards JP, Mumin AH (2013) Magmatic-hydrothermal processes within an evolving Earth: Iron oxide-copper-gold and porphyry Cu ± Mo ± Au deposits. Geology 41:767-770

Rudnick R, Gao S (2003) Composition of the continental crust. Treatise Geochem 3:1-64

Sabet-Mobarhan-Talab A, Alinia F, Ghannadpour S-S, Hezarkhani A (2015) Geology, geochemistry, and some genetic disscussion of the Chador-Malu iron oxide-apatite deposit, Bafq District, Central Iran. Arab J Geosci 8:8399-8418

Sillitoe RH, Burrows DR (2002) New field evidence bearing on the origin of the el laco magnetite deposit, northern Chile. Econ Geol 97:1101-1109

Sillitoe RH (2003) Iron oxide-copper-gold deposits: an Andean view. Miner Deposita 38:787-812. doi: 10.1007/s00126-003-0379-7

Tassi F et al. (2009) The magmatic- and hydrothermal-dominated fumarolic system at the active crater of Láscar volcano, northern Chile. Bull Volcanol 71:171-183

Tornos F, Velasco F, Hanchar JM (2016) Iron oxide melts, magmatic magnetite and superheated magmatic-hydrothermal systems: the El Laco deposit, Chile. Geology, 44(6):427-430

Valley PM, Fisher CM, Hanchar JM, Lam R, and Tubrett M (2010) Hafnium isotopes in zircon: A tracer of fluid-rock interaction during magnetite-apatite ("Kiruna-type") mineralization. Chemical Geology 275:208-220

Valley PM, Hanchar JM, Whitehouse MJ (2011) New insights on the evolution of the Lyon mountain granite and associated Kiruna-type magnetite-apatite deposits, Adirondack Mountains, New York State. Geosphere 7:357-389

Velasco F, Tornos F (2012) Insights on the effects of the hydrothermal alteration in the El Laco magnetite deposit (Chile). Revista de la Sociedad Española de Mineralogía 16:210-211

Westhues A, Hanchar JM, Whitehouse MJ, Martinsson O (2016) New constraints on the timing of host rock emplacement, hydrothermal alteration and iron oxide apatite mineralization in and around Kiruna, Norrbotten region, northern Sweden. Econ Geol, in press

Williams PJ, Hedenquist JW, Barton MD, Johnson DA, Fontbote L, de Haller A, Mark G, Oliver NHS, Marschik R, Thompson JFH, Goldfarb RJ, Richards JP (2005) Iron oxide copper-gold deposits; geology, space-time distribution, and possible modes of origin. Econ Geol 100:371-405

Chapter 3: Summary

Magnetite-apatite ore mineralization has been a subject of debate for over a century and it continues to remain unclear whether they are of hydrothermal or magmatic origin, or a combination of those two processes (e.g., Geijer, 1910; Geijer, 1919; Parák, 1975; Frietsch, 1978; Nyström and Henríquez, 1994; Dare et al., 2014; Tornos et al., 2016). My research contributes to the understanding of how magnetite-apatite ore crystallized at El Laco and Kiruna specifically and possibly other localities through interpretation of the trace element content of magnetite.

Magnetite can incorporate a wide range of trace elements, with distinctive chemical characteristics depending on the crystallizing environment in which it formed. The specific trace element characteristics of magnetite from the various crystallizing environments are not yet well known. Previous authors have proposed various empirical discrimination diagrams to delineate the magnetite chemistry from different types of deposits and crystallizing environments. My research presents new magnetite trace element geochemistry data from the magnetite-apatite deposits in Kiruna, Sweden, and El Laco, Chile, and their respective host rocks as well as magnetite from three different crystallizing environments. The magnetite chemistry was used in this study to critically evaluate the proposed discrimination diagrams for their general use and determine whether magnetite chemistry can be used to determine the crystallizing environment (i.e., hydrothermal or magmatic) of magnetite-apatite deposits. The following conclusions were drawn from this study:

1) From the mineral deposit-type magnetite discrimination diagrams tested in this study only the earlier diagrams by Loberg and Horndahl (1983), worked for effectively

plotting the magnetite-apatite ores within the appropriate field. The more recent empirical discrimination diagrams proposed by Dupuis and Beaudoin (2011) and Knipping et al. (2015), with more tightly constrained fields, need to be modified if they are to include the Kiruna-type magnetite.

2) The magmatic vs. hydrothermal diagrams tested in this study did not help in determining the mineralizing environment of magnetite-apatite deposits. The magnetite discrimination diagram proposed by Knipping et al. (2015) needs modification as many of the data from the present study did not plot within either of the proposed fields. We believe that the magmatic vs. hydrothermal magnetite diagram by Dare et al. (2014) is too simple to distinguish the crystallizing environment of magnetite because the Ti and Ni/Cr ratios do not only depend on the precipitation from silicate or aqueous fluids. The diagram was also not entirely useful since most of the magnetite analyzed has Cr, Ti or Ni content at or below the LOD. The multi-element variation diagrams proposed by Dare et al. (2014) only work if the magnetite-apatite ores are actually of hydrothermal origin, and do not work on magnetite that have undergone subsequent metamorphism and/or metasomatic alteration such as at Kiruna.

3) Based on the trace element results of the magnetite in Kiruna it is likely that the grains are mostly influenced by subsequent metamorphism and/or metasomatic alteration by hydrothermal fluids because primary textures and unique chemical signatures do not appear to be present. Therefore, conclusions on the crystallizing environment of the magnetite-apatite ores in Kiruna cannot be made using the magnetite chemistry. At El Laco however, the magnetite shows internal chemical zonation that are indicative of having crystallized from a volatile-rich iron oxide melt rather than directly as a

precipitate from hydrothermal fluids. This interpretation is based on unique differences in the chemical zonations of the magnetite-apatite ore magnetite at El Laco and the chemical zonations found in iron-rich skarn magnetite presented by Dare et al. (2014).

References

Dare SAS, Barnes S-J, Beaudoin G, Méric J, Boutroy E, and Potvin-Doucet C (2014) Trace elements in magnetite as petrogenetic indicators. Miner Deposita 49:785-796

Dupuis C, Beaudoin G (2011) Discriminant diagrams for iron oxide trace element fingerprinting of mineral deposit types. Miner Deposita 46:319-335.

Frietsch R (1978) On the magmatic origin of iron ores of the Kiruna type. Econ Geol 73:478-485

Geijer P (1910) Igneous rocks and iron ores of Kiirunavaara, Luossavaara and Tuollavaara. Scientific and practical researches in Lapland arranged by the Luossavaara-Kiirunavaara Aktiebolag - Geology of the Kiruna district, 2: Stockholm, p. 278

Geijer P (1919) Recent developments at Kiruna, SGU, C 288, p. 23

Knipping JL, Bilenker LD, Simon AC, Reich M, Barra F, Deditius AP, Wälle M, Heinrich CA, Holtz F, and Munizaga R (2015) Trace elements in magnetite from massive iron oxide-apatite deposits indicate a combined formation by igneous and magmatic-hydrothermal processes. Geochim Cosmochim Acta 171:15-38

Loberg BEH, and Horndahl A-K (1983) Ferride geochemistry of swedish precambrian iron ores. Miner Deposita 18:487-504

Nyström JO, and Henríquez F (1994) Magmatic features of iron ores of the Kiruna type in Chile and Sweden; ore textures and magnetite geochemistry. Econ Geol 89:820-839

Parák T (1975) Kiruna iron ores are not 'intrusive-magmatic ores of the Kiruna type'. Econ Geol 70:1242-1258

Appendix I. Sample list with GPS location, underground level (Kiruna samples) or Elevation (El Laco and Láscar samples), rock type, mineralogy and magnetite textures.

Sample	Latitude	Longitude	Underground level (m)	Rock type: *mineralogy*	Magnetite texture
KRN-10-02	N 67° 51' 11.5"	E 20° 12 '42.1"	1060	B-ore: *mag, ±bt*	massive
K-1	N 67° 51' 0.6"	E 20° 12' 23.8"	767	D-ore: *mag, ap, plag, ±bt, ksp, qtz*	subhedral
K-2	N 67° 51' 11.5"	E 20° 12 '42.1"	1060	B-ore: *mag, ±bt*	massive
KRN-11-01	N 67° 51' 15.7"	E 20° 12' 20.7"	816	D-ore: *mag, act, ap*	massive, subhedral
KRN-11-03	N 67° 50' 13.1"	E 20° 12' 17.4"	1365	Andesite (less altered FW): *plag, ksp, bt, act, mag, ±qtz*	anhedral
KRN-11-04	N 67° 51' 07.0"	E 20° 12' 25.1"	1020	Andesite (altered FW): *ksp, plag, bt, mag, act, ±qtz*	anhedral
KRN-11-05	N 67° 50' 35.6"	E 20° 12' 37.4"	1065	Rhyodacite (less altered HW): *ksp, plag, qtz, bt, ±amph*	euhedral-subhedral
KRN-12-02	N 67° 50' 57.8"	E 20° 10' 24.7"	Surface	Aplite vein: *qtz, ksp, plag, ±mag, act, tit, zr*	anhedral
KRN-12-03	N 67° 50' 23.4"	E 20° 10' 49.7"	Surface	Syenite: *ksp, amph, tit, ±plag, qtz*	anhedral
KRN-12-05	N 67° 50' 30.1"	E 20° 10' 50.1"	1365	Granite: *ksp, qtz, tit, ilm, ±plag, bt*	euhedral-subhedral
REK-10-04	N 67° 52' 17.4"	E 20° 14' 07.4"	Surface	Ore: *mag, hem, ap, ±cc, qtz*	massive mag and hem
REK-12-02	N 67° 52' 18.0"	E 20° 14' 08.1"	Surface	Rhyodacite (FW): *qtz, ap, ksp (ser), chl, mag ±bt*	subhedral-anhedral
NUK-10-03	N 67° 53' 51.0"	E 20° 15' 31.9"	Surface	Ore: *mag, ap, act, bt, ±cc*	subhedral-anhedral
NUK-12-02	N 67° 53' 51.0"	E 20° 15' 31.9"	Surface	Ore + host: *mag, ap, qtz, ksp, ser, ±bt*	subhedral-anhedral
TUV-10-01	N 67° 51' 15.1"	E 20° 18' 54.1"	Surface	Ore: *mag, act, ap*	anhedral
TUV-10-03	N 67° 51' 13.9"	E 20° 18' 57.0"	Surface	Rhyodacite: *ksp, qtz ±amph, tit*	anhedral

Appendix I. (continued)

Sample	Latitude	Longitude	Elevation (m)	Rock type: mineralogy	Magnetite texture
ELL-14-02	S 23° 49' 5.9"	W 67° 29' 40.2"	4814	Andesite (host): *plag, cpx, ±qtz, mag*	anhedral, micro-ilmenite exsolution in BSE
ELL-14-04	S 23° 15' 14.4"	W 67° 29' 22.2"	5404	Vuggy ore: *mag, keno-mag ±mar*	massive, euhedral lining voids, extensive alteration to keno-mag, porous cores with growth zoning
ELL-14-05	S 23° 15' 14.4"	W 67° 29' 22.2"	5404	Vesicular ore*: mag ±mar*	massive and vesicular, euhedral lining voids, mag growth zoning
ELL-14-06	S 23° 50' 33.8"	W 67° 29' 22.2"	4653	Vein ore: *mag ±mar*	massive and subhedral-euhedral lining voids, extensive alteration to martite, mag growth zoning
LAS-14-07	S 23° 22'	W 67° 43'	base of volcano	Dacite (Volcanic ejecta): *plag, cpx, ±qtz, mag*	anhedral, some ilmenite exsolution in BSE

Notes: KRN/K: Kiirunavaara, REK: Rektorn, NUK: Nukutusvaara, TUV: Tuollavaara, FW: footwall, HW: hanging wall; ELL: El Laco volcano, Laco Sur deposit; LAS: Láscar volcano*;*

Mineral abbreviations: *mag*=magnetite, hem=hematite, mar=martite, keno-mag=kenomagnetite, *ap*=apatite, *bt*=biotite*, qt*= quartz*, plag*=plagioclase*, ksp*=k-feldspar*, act*=actinolite*, hbl*=hornblende*, amph*=amphib*ole, ilm*=ilmenite*, tit*=titanite*, cc*=calcium carbonate*, ser*=sericite*, chl*=chlorite, *zr*=zircon, *cpx*=clinopyroxene

Appendix II. Summarized methods for EPMA Fe analysis and LA-ICPMS trace element analyses of magnetite.

EPMA	
Model	JEOL JXA-8230 Superprobe
Voltage	15kV
Current	100nA
Spot size	3μm
Peak counting time	10s
Background counting time	20s
Primary standard	Astimex magnetite
Secondary standards used:	Balmat, Mud Tank, and BC-28 natural magnetite
Element X-ray line	Fe (K_α)
Analyzing crystal	LiFH
LA-ICPMS	
Model	Thermo-Finnigan ELEMENT XR coupled with a GeoLas 193 nm Excimer laser system
Pulse frequency	8 Hz
Energy density	3 J/cm^2
Spot size	30-59μm depending on sample and trace element concentration.
Gas blank	30s
Signal	60s
Internal standard	Fe (EPMA)
Primary reference material	NIST-610
Secondary reference material	BCR-2G; Balmat, Mud Tank, BC-28 natural magnetite

Appendix III. Average (mean) LA-ICP-MS (ppm) and EPMA (Fe wt %) results for trace elements used in plots from Kiruna and El Laco/Láscar magnetite samples. Minimum level of detection (LOD) calculated by Iolite reported for each analysis session.

	Kiruna	**KRN-10-02**	**K-1**	**K-2**	**KRN-11-01**	**KRN-11-03**	**KRN-11-04**	**KRN-11-05**	**KRN-12-02**
	Min LOD	N=6	N=7	N=9	N=7	N=5	N=7	N=2	N=3
Fe	EPMA	69.7	69.6	70.0	70.2	70.3	70.3	69.9	69.7
^{24}Mg	8.20	764	249	78.4	54.4	64.8	89.5	<LOD	43.3
^{27}Al	16.59	38.0	263	39.4	569	97.3	92.3	83.0	44.0
^{29}Si	496.60	3620	1530	947	2590	850	908	1600	850
^{31}P	16.49	175	38.0	132	297	20.3	<LOD	31.0	36.0
^{44}Ca	254	860	<LOD	440	<LOD	<LOD	660	<LOD	330
^{47}Ti	31.6	61.0	77.0	63.5	209	<LOD	68.3	<LOD	50.0
^{51}V	2.21	1439	1526	886	1264	772	986	176	1744
^{52}Cr	19.9	70.0	63.0	46.7	105	79.2	79.7	101	73.5
^{55}Mn	2.25	378	362	321	400	615	376	280	275
^{59}Co	0.37	95.5	118	66.0	35.8	34.6	43.4	23.3	36.9
^{60}Ni	12.8	256	261	163	<LOD	<LOD	35.9	<LOD	54
^{63}Cu	1.48	<LOD	<LOD	<LOD	<LOD	<LOD	<LOD	<LOD	<LOD
^{66}Zn	1.47	21.0	17.3	16.0	15.6	28.4	17.2	6.45	16.2
^{71}Ga	0.20	5.52	1.70	11.7	3.40	17.0	10.0	6.94	13.8
^{88}Sr	0.24	1.52	1.16	1.28	<LOD	2.2	1.16	<LOD	1.39
^{89}Y	0.03	1.72	0.25	0.27	<LOD	0.56	<LOD	1.09	0.17
^{93}Nb	0.06	0.30	0.68	<LOD	1.22	0.09	<LOD	<LOD	<LOD
^{118}Sn	0.48	1.86	1.02	<LOD	3.55	<LOD	0.53	<LOD	<LOD
^{140}Ce	0.001	7.57	0.58	2.67	0.31	0.24	0.23	0.10	0.21
^{178}Hf	0.001	0.02	0.00	0.00	<LOD	0.01	0.00	1.91	<LOD
^{181}Ta	0.001	<LOD	0.08	<LOD	<LOD	<LOD	<LOD	0.04	<LOD
^{208}Pb	0.03	1.63	0.38	0.39	0.14	0.40	0.18	0.11	0.31
^{232}Th	0.001	1.23	0.11	0.57	0.02	0.01	0.05	0.10	0.01

Appendix III. (continued)

Element or isotope	KRN-12-03 mag N=7	KRN-12-05 mag N=2	TUV-10-01 mag N=6	TUV-10-03 mag N=2	NUK-10-03 mag N=6	NUK-12-02 mag N=6	REK-10-04 mag N=3	REK-10-04 hem N=3	REK-12-02 mag N=6
Fe	70.1	70.1	70.0	70.6	70.2	70.0	67.4	67.3	70.3
^{24}Mg	58.6	39	14	221	55.0	103	72.5	16.6	71.2
^{27}Al	116	166	43	167	142	160	310	120	<LOD
^{29}Si	2140	1130	<LOD	1055	1060	1373	1700	1845	<LOD
^{31}P	36.5	196	<LOD	34.5	29.0	52.0	53.0	37.2	<LOD
^{44}Ca	430	1050	<LOD	<LOD	<LOD	580	400	<LOD	<LOD
^{47}Ti	123	<LOD	<LOD	<LOD	853	2164	12419	4648	1120
^{51}V	964	324	605	549	1075	940	1327	605	232
^{52}Cr	93.0	431	47	<LOD	120	115	64.0	92.5	53.0
^{55}Mn	428	94.6	240	388	149	62.5	56.6	16.5	38.9
^{59}Co	43.1	10.0	76.9	121	130	127	6.33	2.86	70.9
^{60}Ni	<LOD	<LOD	76	207	301	176	278	<LOD	78.6
^{63}Cu	<LOD	13.9	<LOD	<LOD	9.40	<LOD	136	5.21	<LOD
^{66}Zn	32.2	11.0	6.10	9.70	21.6	19.6	4.43	<LOD	5.29
^{71}Ga	4.36	10.7	14	28	22.7	5.91	19.6	3.59	1.74
^{88}Sr	0.68	<LOD	<LOD	1.23	0.87	3.99	2.68	1.07	<LOD
^{89}Y	0.55	0.43	<LOD	0.17	1.04	0.63	0.89	1.37	<LOD
^{93}Nb	0.32	<LOD	<LOD	<LOD	0.32	2.42	0.73	1.21	1.03
^{118}Sn	<LOD	<LOD	<LOD	<LOD	1.43	<LOD	4.73	2.146	<LOD
^{140}Ce	0.46	2.78	0.05	0.34	23.7	3.19	4.76	5.17	0.10
^{178}Hf	6.70	<LOD	0.01	0.02	<LOD	0.01	0.06	0.91	<LOD
^{181}Ta	<LOD	<LOD	<LOD	<LOD	<LOD	0.14	0.10	0.24	<LOD
^{208}Pb	0.57	0.27	0.62	0.21	0.61	2.32	1.09	2.66	0.26
^{232}Th	0.93	0.07	0.06	0.09	1.33	0.31	0.78	0.70	0.02

Appendix III. (continued)

	El Laco and Láscar Min LOD	ELL-14-02	ELL-14-04	ELL-14-05	ELL-14-06	LAS-14-07	LAS-14-07	Balmat	BC-28
		N=17	N=14	N=18	N=20	N=9	N=9	N=18	N=14
Fe	EPMA	63.6	69.4	68.9	68.1	68	60.4	68.7	57.2
^{24}Mg	13.6	2560	6615	9626	5157	3606	14440	129	8175
^{27}Al	39.1	6335	1642	1437	109	117	12599	91.0	12294
^{29}Si	1349	4363	4178	7161	4890	2784	9500	1240	2700
^{31}P	36.5	741	158	200	417	482	1188	26.4	188
^{44}Ca	749	<LOD	<LOD	2510	1817	1130	4407	<LOD	<LOD
^{47}Ti	59.6	65920	288	275	517	459	83000	66	70656
^{51}V	5.82	2947	1882	996	586	604	4574	408	10111
^{52}Cr	21.2	710	100	54.5	72.4	35	822	134	1409
^{55}Mn	4.75	4125	276	402	271	221	4093	346	2370
^{59}Co	1.32	119	119.11	151	111	107	248	18.7	223
^{60}Ni	19.5	200	438	434	275	269	353	n.d.	450
^{63}Cu	3.66	28.4	<LOD	22.4	36.0	52.5	52.5	n.d.	126
^{66}Zn	9.76	1651	51.5	49.8	51.8	1254	1254	22101	337
^{71}Ga	0.33	49.1	6.31	2.06	1.14	64.9	64.9	35.6	55.6
^{72}Ge	9.74	<LOD	<LOD	<LOD	<LOD	<LOD	<LOD	440	n.d.
^{88}Sr	0.32	1.83	1.59	1.83	3.01	0.32	0.32	0.66	2.66
^{89}Y	0.00	1.61	1.11	0.97	5.04	0.00	0.00	n.d.	n.d.
^{93}Nb	<LOD	19.2	1.54	2.32	12.1	0.00	0.00	n.d.	1.30
^{95}Mo	1.87	<LOD	3.60	9.57	<LOD	1.87	1.87	322	<LOD
^{118}Sn	2.50	8.37	14.5	12.8	13.6	27.4	27.4	52.4	1.82
^{140}Ce	<LOD	6.64	1.66	7.81	36.1	17.9	17.9	0.07	0.19
^{181}Ta	<LOD	0.58	0.51	0.30	0.25	1.51	1.51	n.d.	0.08

Note: N=total number of analysis; <LOD= below level of detection; n.d.,=not determined

Appendix IV. EPMA Fe results. Spot locations are shown on BSE images of magnetite grains in Appendix VI.

Analysis I.D.	Sample I.D.	Ablation Analysis	FeO wt. %	Fe wt. %	Avg. Spot Analysis
a	KRN-10-02	ap22a08	89.9	69.9	69.8
b	KRN-10-02	ap22a08	89.9	69.9	
c	KRN-10-02	ap22a08	89.5	69.6	
e	KRN-10-02	ap22a09	89.9	69.9	69.8
f	KRN-10-02	ap22a09	90.0	69.9	
g	KRN-10-02	ap22a09	89.5	69.6	
h	KRN-10-02	ap22a10	89.9	69.9	69.7
i	KRN-10-02	ap22a10	89.4	69.5	
j	KRN-10-02	ap22a10	89.7	69.8	
k	KRN-10-02	ap22a11	89.5	69.6	69.7
l	KRN-10-02	ap22a11	89.6	69.7	
n	KRN-10-02	ap22a11	89.8	69.8	
o	KRN-10-02	ap22a12	89.7	69.7	69.1
p	KRN-10-02	ap22a12	88.0	68.4	
q	KRN-10-02	ap22a13	89.7	69.7	69.6
r	KRN-10-02	ap22a13	89.5	69.6	
s	KRN-10-02	ap22a13	89.5	69.6	
a	K-1	ap22a14	89.7	69.7	69.7
b	K-1		89.9	69.9	
c	K-1	ap22a16	89.7	69.7	69.7
d	K-1	ap22a17	89.6	69.6	69.6
e	K-1	ap22a17	89.3	69.4	
f	K-1	ap22a17	89.6	69.6	
g	K-1	ap22a25	89.3	69.4	69.4
h	K-1	ap22a25	89.1	69.2	
i	K-1	ap22a25	89.4	69.5	
j	K-1	ap22a26	89.5	69.6	69.7
k	K-1	ap22a26	89.7	69.7	
l	K-1	ap22a26	89.7	69.7	
m	K-1	ap22a27	89.6	69.6	69.6
n	K-1	ap22a27	89.7	69.7	
o	K-1	ap22a27	89.3	69.4	
p	K-1	ap22a28	89.9	69.8	69.7
q	K-1	ap22a28	89.7	69.7	
r	K-1	ap22a28	89.4	69.5	
a	K-2	ap22a30	89.8	69.8	69.8
b	K-2	ap22a30	89.9	69.9	
c	K-2	ap22a30	89.8	69.8	
d	K-2	ap22a29	89.9	69.9	69.8
e	K-2	ap22a29	89.7	69.7	
f	K-2	ap22a29	89.8	69.8	

Appendix IV. (Cont.)

Analysis I.D.	Sample I.D.	Ablation Analysis	FeO wt. %	Fe wt. %	Avg. Spot Analysis
g	K-2	ap22a31	90.1	70.0	70.3
h	K-2	ap22a31	90.5	70.3	
i	K-2	ap22a31	90.7	70.5	
j	K-2	ap22a32	90.3	70.2	70.1
k	K-2	ap22a32	90.2	70.1	
l	K-2	ap22a32	89.9	69.8	
m	K-2	ap22a33	90.5	70.4	70.3
n	K-2	ap22a33	90.3	70.2	
o	K-2	ap22a33	90.4	70.2	
p	K-2	ap22a34	90.4	70.2	70.3
q	K-2	ap22a34	90.5	70.3	
r	K-2	ap22a34	90.6	70.4	
s	K-2	ap22a42	89.8	69.8	69.7
t	K-2	ap22a42	89.8	69.8	
u	K-2	ap22a42	89.6	69.6	
v	K-2	ap22a43	90.0	70.0	69.4
w	K-2	ap22a43	89.8	69.8	
x	K-2	ap22a43	87.9	68.4	
y	K-2	ap22a44	89.6	69.7	69.9
z	K-2	ap22a44	89.8	69.8	
zz	K-2	ap22a44	90.2	70.1	
a	KRN-11-01	ap22a46	86.8	67.4	69.3
b	KRN-11-01	ap22a46	90.4	70.3	
c	KRN-11-01	ap22a46	90.4	70.3	
d	KRN-11-01	ap22a47	90.0	70.0	70.1
e	KRN-11-01	ap22a47	90.3	70.2	
f	KRN-11-01	ap22a47	90.2	70.1	
g	KRN-11-01	ap22a48	90.4	70.2	70.2
h	KRN-11-01	ap22a48	90.2	70.1	
i	KRN-11-01	ap22a48	90.2	70.1	
j	KRN-11-01	ap22a49	90.2	70.1	70.1
k	KRN-11-01	ap22a50	90.2	70.1	70.1
l	KRN-11-01	ap22a51	90.6	70.4	70.4
m	KRN-11-01		89.5	69.6	
n	KRN-11-01	ap22a60	90.2	70.1	70.1
o	KRN-11-01		90.8	70.6	
a	KRN-11-03	ap22a80	90.5	70.4	70.2
b	KRN-11-03	ap22a80	90.4	70.2	
c	KRN-11-03	ap22a80	90.2	70.1	
d	KRN-11-03	ap22a81/82	90.2	70.1	70.4
e	KRN-11-03	ap22a81/82	90.7	70.5	

Appendix IV. (Cont.)

Analysis I.D.	Sample I.D.	Ablation Analysis	FeO wt. %	Fe wt. %	Avg. Spot Analysis
f	KRN-11-03	ap22a81/82	90.7	70.5	
g	KRN-11-03		89.6	69.6	
h	KRN-11-03		90.0	70.0	
i	KRN-11-03		90.1	70.1	
j	KRN-11-03	ap22a83/84	90.5	70.3	70.2
k	KRN-11-03	ap22a83/84	90.4	70.3	
l	KRN-11-03	ap22a83/84	90.1	70.1	
a	KRN-11-04	ap22a85	90.4	70.3	70.3
b	KRN-11-04	ap22a85	90.3	70.2	
c	KRN-11-04		91.0	70.7	
d	KRN-11-04	ap22a86	90.7	70.5	70.5
e	KRN-11-04	ap22a86	90.8	70.6	
f	KRN-11-04	ap22a86	90.7	70.5	
g	KRN-11-04	ap22a87	90.8	70.6	70.6
h	KRN-11-04	ap22a87	90.8	70.6	
i	KRN-11-04	ap22a87	90.8	70.6	
j	KRN-11-04	ap23a05	90.4	70.3	70.1
k	KRN-11-04	ap23a05	90.3	70.2	
l	KRN-11-04	ap23a05	89.9	69.9	
m	KRN-11-04	ap23a06	90.4	70.3	70.2
n	KRN-11-04	ap23a06	90.2	70.1	
o	KRN-11-04	ap23a07	90.6	70.4	70.1
p	KRN-11-04	ap23a07	90.1	70.1	
q	KRN-11-04	ap23a07	89.9	69.9	
r	KRN-11-04	ap23a08	90.0	70.0	70.1
s	KRN-11-04	ap23a08	90.4	70.2	
t	KRN-11-04	ap23a08	90.0	70.0	
a	KRN-11-05	ap23a10	89.4	69.5	69.6
b	KRN-11-05	ap23a10	89.6	69.6	
c	KRN-11-05	ap23a10	89.7	69.7	
d	KRN-11-05		89.8	69.8	
e	KRN-11-05		88.9	69.1	
f	KRN-11-05		89.7	69.7	
g	KRN-11-05	ap23a09	90.4	70.3	70.1
h	KRN-11-05	ap23a09	90.1	70.1	
i	KRN-11-05	ap23a09	90.1	70.1	69.8
a	KRN-12-02	ap23a12	90.0	70.0	
b	KRN-12-02	ap23a12	90.1	70.0	
c	KRN-12-02	ap23a12	89.5	69.6	70.0
d	KRN-12-02	ap23a11	90.3	70.2	
e	KRN-12-02	ap23a11	89.9	69.9	

Appendix IV. (Cont.)

Analysis I.D.	Sample I.D.	Ablation Analysis	FeO wt. %	Fe wt. %	Avg. Spot Analysis
f	KRN-12-02	ap23a11	89.9	69.9	69.8
g	KRN-12-02	ap23a13	89.9	69.9	
h	KRN-12-02	ap23a13	90.0	70.0	
i	KRN-12-02	ap23a13	89.6	69.7	70.0
a	KRN-12-03	ap23a25	90.0	70.0	
b	KRN-12-03		90.4	70.3	70.0
c	KRN-12-03	ap23a26	90.1	70.0	70.1
d	KRN-12-03	ap23a14	90.3	70.2	
e	KRN-12-03	ap23a14	90.0	70.0	
f	KRN-12-03	ap23a14	90.2	70.1	70.2
g	KRN-12-03	ap23a27	90.4	70.3	
h	KRN-12-03	ap23a27	90.5	70.4	
i	KRN-12-03	ap23a27	90.1	70.0	70.1
j	KRN-12-03	ap23a28	90.2	70.1	
k	KRN-12-03	ap23a28	90.3	70.2	
l	KRN-12-03	ap23a28	90.2	70.1	70.4
m	KRN-12-03	ap23a29	90.9	70.7	
n	KRN-12-03	ap23a29	90.7	70.5	
o	KRN-12-03	ap23a29	90.2	70.1	70.3
p	KRN-12-03	ap23a30	90.4	70.3	
q	KRN-12-03	ap23a30	90.6	70.4	
r	KRN-12-03	ap23a30	90.1	70.0	70.0
a	KRN-12-05	ap23a31	90.3	70.2	
b	KRN-12-05	ap23a31	89.9	69.9	
c	KRN-12-05	ap23a31	90.0	69.9	70.1
e	KRN-12-05	ap23a40	90.2	70.1	
f	KRN-12-05	ap23a40	90.0	69.9	
g	KRN-12-05	ap23a40	90.5	70.3	
h	KRN-12-05		90.2	70.1	
i	KRN-12-05		90.0	69.9	
j	KRN-12-05		90.3	70.2	
a	TUV-10-03		90.4	70.3	
b	TUV-10-03		90.0	69.9	
c	TUV-10-03		90.2	70.1	
d	TUV-10-03	ap23a61	90.2	70.1	70.0
e	TUV-10-03	ap23a61	89.7	69.8	
f	TUV-10-03	ap23a61	90.3	70.2	
g	TUV-10-03		90.4	70.3	
h	TUV-10-03		90.0	70.0	
i	TUV-10-03		88.3	68.6	
j	TUV-10-03	ap23a63	89.8	69.8	69.4

Appendix IV. (Cont.)

Analysis I.D.	Sample I.D.	Ablation Analysis	FeO wt. %	Fe wt. %	Avg. Spot Analysis
k	TUV-10-03	ap23a63	90.3	70.2	
l	TUV-10-03	ap23a63	89.8	69.8	
m	TUV-10-03	ap23a63	87.1	67.7	
a	TUV-10-01	ap22a67	90.5	70.4	70.3
b	TUV-10-01	ap22a67	90.3	70.2	
c	TUV-10-01	ap22a67	90.7	70.5	
d	TUV-10-01	ap22a68	90.7	70.5	70.5
e	TUV-10-01	ap22a68	90.6	70.4	
f	TUV-10-01	ap22a68	90.8	70.6	
g	TUV-10-01	ap22a69	91.2	70.9	70.5
h	TUV-10-01	ap22a69	90.5	70.4	
i	TUV-10-01	ap22a69	90.6	70.4	
j	TUV-10-01	ap22a77	90.9	70.7	70.7
k	TUV-10-01	ap22a77	91.0	70.8	
l	TUV-10-01	ap22a77	91.1	70.8	
m	TUV-10-01		91.0	70.7	
n	TUV-10-01		90.5	70.4	
o	TUV-10-01		90.8	70.6	
a	NUK-10-03	ap23a41	90.0	70.0	70.0
b	NUK-10-03	ap23a41	89.6	69.7	
c	NUK-10-03	ap23a41	90.5	70.3	
d	NUK-10-03	ap23a42	90.6	70.4	70.6
e	NUK-10-03	ap23a42	90.8	70.6	
f	NUK-10-03	ap23a42	90.8	70.6	
g	NUK-10-03	ap23a43	90.1	70.0	70.1
h	NUK-10-03	ap23a43	90.3	70.2	
i	NUK-10-03	ap23a43	90.1	70.0	
j	NUK-10-03	ap23a44	89.1	69.3	69.9
k	NUK-10-03	ap23a44	90.3	70.2	
l	NUK-10-03	ap23a44	90.5	70.3	
m	NUK-10-03	ap23a45	90.3	70.2	70.2
n	NUK-10-03		90.5	70.4	
o	NUK-10-03	ap23a46	90.1	70.1	70.1
a	NUK-12-02	ap23a47	90.0	70.0	69.9
b	NUK-12-02	ap23a47	90.2	70.1	
c	NUK-12-02	ap23a47	89.6	69.7	
d	NUK-12-02	ap23a48	89.8	69.8	69.8
e	NUK-12-02	ap23a48	89.7	69.7	
f	NUK-12-02	ap23a48	89.9	69.9	
g	NUK-12-02	ap23a49	90.3	70.2	69.9
h	NUK-12-02	ap23a49	89.7	69.7	

Appendix IV. (Cont.)

Analysis I.D.	Sample I.D.	Ablation Analysis	FeO wt. %	Fe wt. %	Avg. Spot Analysis
i	NUK-12-02	ap23a49	89.7	69.7	
j	NUK-12-02	ap23a59	90.2	70.1	70.1
k	NUK-12-02		90.1	70.0	
l	NUK-12-02	ap23a58	90.3	70.2	70.2
m	NUK-12-02	ap23a60	90.2	70.1	70.2
n	NUK-12-02	ap23a60	90.1	70.0	
o	NUK-12-02	ap23a60	90.5	70.3	
a	REK-10-01	ap23a64	86.8	67.5	67.4
b	REK-10-01	ap23a64	86.7	67.4	
c	REK-10-01	ap23a64	86.7	67.4	
d	REK-10-01	ap23a65	86.7	67.4	67.5
e	REK-10-01	ap23a65	87.1	67.7	
f	REK-10-01	ap23a65	86.6	67.3	
g	REK-10-01	ap23a66	86.3	67.1	67.0
h	REK-10-01	ap23a66	86.2	67.0	
i	REK-10-01	ap23a66	85.9	66.8	
j	REK-10-01	ap23a67	86.6	67.3	67.2
k	REK-10-01	ap23a67	86.6	67.3	
l	REK-10-01	ap23a67	86.4	67.1	
m	REK-10-01	ap23a68	86.4	67.2	67.3
n	REK-10-01	ap23a68	86.8	67.5	
o	REK-10-01	ap23a68	86.7	67.4	
a	REK-10-04	ap22a61	84.3	65.5	64.6
b	REK-10-04	ap22a61	82.1	63.8	
c	REK-10-04	ap22a62	82.1	63.9	64.8
d	REK-10-04	ap22a62	84.6	65.7	
e	REK-10-04	ap22a63	89.5	69.6	68.5
f	REK-10-04	ap22a63	85.0	66.1	
g	REK-10-04	ap22a63	89.9	69.9	
h	REK-10-04	ap22a64	90.3	70.2	70.3
i	REK-10-04	ap22a64	90.5	70.4	
j	REK-10-04	ap22a64	90.6	70.4	
k	REK-10-04	ap22a66	90.6	70.4	70.4
l	REK-10-04	ap22a65	91.2	70.9	68.6
m	REK-10-04	ap22a65	85.3	66.3	
n	REK-10-04	ap22a66	90.0	70.0	70.0
o	REK-10-04	ap22a65	84.7	65.9	
a	REK-12-02	ap23a76	90.7	70.5	70.5
b	REK-12-02	ap23a76	90.7	70.5	
c	REK-12-02	ap23a76	90.7	70.5	
d	REK-12-02	ap23a77	90.0	70.0	70.0

Appendix IV. (Cont.)

Analysis I.D.	Sample I.D.	Ablation Analysis	FeO wt. %	Fe wt. %	Avg. Spot Analysis
e	REK-12-02	ap23a77	90.2	70.1	
f	REK-12-02	ap23a77	89.9	69.9	
g	REK-12-02	ap23a78	90.4	70.2	70.3
h	REK-12-02	ap23a78	90.6	70.4	
i	REK-12-02	ap23a78	90.2	70.1	
j	REK-12-02	ap23a79	90.5	70.3	70.2
k	REK-12-02	ap23a79	90.1	70.1	
l	REK-12-02	ap23a79	90.4	70.3	
m	REK-12-02	ap23a81	90.6	70.4	70.4
n	REK-12-02	ap23a80	90.9	70.6	70.6

Appendix IV. (Cont.)

Analysis I.D.	Sample I.D.	Ablation Analysis	FeO wt. %	Fe wt. %	Avg. Spot Analysis
1	ELL-14-02	no05b09	83.4	64.9	62.6
2	ELL-14-02	no05b09	75.4	58.6	
3	ELL-14-02	no05b09	82.9	64.5	
4	ELL-14-02	no05b10	79.1	61.5	61.5
5	ELL-14-02	no05b10	80.7	62.7	
6	ELL-14-02	no05b10	77.6	60.3	
7	ELL-14-02	no05b11	81.3	63.2	62.8
8	ELL-14-02	no05b11	80.2	62.4	
9	ELL-14-02	no05b11	81.0	63.0	
10	ELL-14-02	no05b12	85.0	66.0	65.6
11	ELL-14-02	no05b12	85.4	66.4	
12	ELL-14-02	no05b12	82.8	64.4	
13	ELL-14-02	no05b15	85.0	66.1	65.3
14	ELL-14-02	no05b15	84.6	65.8	
15	ELL-14-02	no05b15	82.5	64.1	
16	ELL-14-02	no05b16	81.0	63.0	63.4
17	ELL-14-02	no05b16	83.8	65.1	
18	ELL-14-02	no05b16	79.8	62.0	
19	ELL-14-02	no05b17	82.2	63.9	64.1
20	ELL-14-02	no05b17	79.7	61.9	
21	ELL-14-02	no05b17	85.4	66.4	
22	ELL-14-02	no05b18	83.0	64.5	63.9
23	ELL-14-02	no05b18	82.1	63.8	
24	ELL-14-02	no05b18	81.6	63.4	
25	ELL-14-02	no05b21	80.6	62.6	64.2
26	ELL-14-02	no05b21	80.4	62.5	
27	ELL-14-02	no05b21	86.8	67.4	
28	ELL-14-02	no05b22	67.8	52.7	59.4
29	ELL-14-02	no05b22	80.7	62.7	
30	ELL-14-02	no05b22	80.9	62.9	
31	ELL-14-02	no05b23	78.4	60.9	62.4
32	ELL-14-02	no05b23	81.6	63.4	
33	ELL-14-02	no05b23	80.7	62.7	
34	ELL-14-02	no05b24	81.5	63.3	64.2
35	ELL-14-02	no05b24	85.5	66.5	
36	ELL-14-02	no05b24	80.6	62.7	
37	ELL-14-02	no05b26/27	81.2	63.1	62.5
38	ELL-14-02	no05b26/27	79.5	61.8	
1	ELL-14-04	no05d05	83.0	64.5	65.9
2	ELL-14-04	no05d05	86.6	67.3	
3	ELL-14-04	no05d06	87.0	67.6	66.9
4	ELL-14-04	no05d06	85.3	66.3	

Appendix IV. (Cont.)

Analysis I.D.	Sample I.D.	Ablation Analysis	FeO wt. %	Fe wt. %	Avg. Spot Analysis
5	ELL-14-04	no05d07	89.7	69.7	68.1
6	ELL-14-04	no05d07	85.7	66.6	
7	ELL-14-04	no05d07	87.4	67.9	
8	ELL-14-04	no05d08	90.2	70.1	70.0
9	ELL-14-04	no05d08	89.4	69.5	
10	ELL-14-04	no05d08	90.5	70.3	
11	ELL-14-04	no05d09	90.1	70.0	69.7
12	ELL-14-04	no05d09	88.5	68.8	
13	ELL-14-04	no05d09	90.6	70.4	
14	ELL-14-04	no05d10	90.0	69.9	70.1
15	ELL-14-04	no05d10	90.3	70.2	
16	ELL-14-04	no05d11	90.9	70.6	70.0
17	ELL-14-04	no05d11	90.2	70.1	
18	ELL-14-04	no05d11	89.1	69.2	
19	ELL-14-04	no05d12	90.2	70.1	70.1
20	ELL-14-04	no05d12	90.0	69.9	
21	ELL-14-04	no05d12	90.4	70.3	
22	ELL-14-04	no05d13	90.6	70.4	70.1
23	ELL-14-04	no05d13	89.7	69.8	
24	ELL-14-04	no05d13	90.4	70.2	
25	ELL-14-04	no05d14	90.2	70.1	70.2
26	ELL-14-04	no05d14	90.5	70.3	
27	ELL-14-04	no05d14	90.5	70.3	
30	ELL-14-04	no05d17	90.5	70.3	69.9
31	ELL-14-04	no05d17	89.9	69.9	
32	ELL-14-04	no05d17	89.5	69.6	
33	ELL-14-04	no05d18	90.0	69.9	69.2
34	ELL-14-04	no05d18	89.2	69.3	
35	ELL-14-04	no05d18	88.1	68.5	
36	ELL-14-04	no05d19	90.2	70.1	69.9
37	ELL-14-04	no05d19	90.4	70.2	
38	ELL-14-04	no05d19	89.0	69.2	
39	ELL-14-04	no05d20	90.7	70.5	70.4
40	ELL-14-04	no05d20	90.5	70.3	
41	ELL-14-04	no05d20	90.4	70.3	
1	ELL-14-05	no05c08	89.1	69.2	69.6
2	ELL-14-05	no05c08	89.4	69.5	
3	ELL-14-05	no05c08	90.1	70.0	
4	ELL-14-05	no05c09	87.4	68.0	68.4
5	ELL-14-05	no05c09	88.1	68.5	
6	ELL-14-05	no05c09	88.4	68.7	
7	ELL-14-05	no05c10	85.7	66.6	69.1
8	ELL-14-05	no05c10	90.4	70.2	
9	ELL-14-05	no05c10	90.7	70.5	

Appendix IV. (Cont.)

Analysis I.D.	Sample I.D.	Ablation Analysis	FeO wt. %	Fe wt. %	Avg. Spot Analysis
1	ELL-14-06	no05a06	85.9	66.8	67.4
2	ELL-14-06	no05a06	86.4	67.1	
3	ELL-14-06	no05a07	86.0	66.8	67.2
4	ELL-14-06	no05a07	87.0	67.7	
5	ELL-14-06	no05a07	86.5	67.3	
6	ELL-14-06	no05a08	87.9	68.3	68.0
7	ELL-14-06	no05a08	86.9	67.6	
8	ELL-14-06	no05a08	87.6	68.1	
9	ELL-14-06	no05a09	88.3	68.6	67.8
10	ELL-14-06	no05a09	85.2	66.2	
11	ELL-14-06	no05a09	88.1	68.5	
12	ELL-14-06	no05a10	89.1	69.3	69.4
13	ELL-14-06	no05a10	89.4	69.5	
14	ELL-14-06	no05a10	89.3	69.4	
15	ELL-14-06	no05a11	88.7	68.9	68.5
16	ELL-14-06	no05a11	86.8	67.4	
17	ELL-14-06	no05a11	88.9	69.1	
18	ELL-14-06	no05a12	88.8	69.0	68.8
19	ELL-14-06	no05a12	88.8	69.0	
20	ELL-14-06	no05a12	87.9	68.3	
21	ELL-14-06	no05a13	88.8	69.0	67.9
22	ELL-14-06	no05a13	86.3	67.1	
23	ELL-14-06	no05a13	87.0	67.6	
24	ELL-14-06	no05a14	86.7	67.4	67.5
25	ELL-14-06	no05a14	86.9	67.6	
26	ELL-14-06	no05a14	86.9	67.5	
27	ELL-14-06	no05a15	87.3	67.9	67.2
28	ELL-14-06	no05a15	85.5	66.5	
29	ELL-14-06	no05a15	86.5	67.2	
30	ELL-14-06	no05a23	88.5	68.8	67.9
31	ELL-14-06	no05a23	86.4	67.2	
32	ELL-14-06	no05a23	87.3	67.8	
33	ELL-14-06	no05a24	87.3	67.8	68.9
34	ELL-14-06	no05a24	89.0	69.2	
35	ELL-14-06	no05a24	89.6	69.7	
36	ELL-14-06	no05a26	88.8	69.0	69.0
37	ELL-14-06	no05a26	88.5	68.8	
38	ELL-14-06	no05a26	89.1	69.2	
39	ELL-14-06	no05a27	87.5	68.0	68.0
40	ELL-14-06	no05a27	87.1	67.7	
41	ELL-14-06	no05a27	88.1	68.4	
42	ELL-14-06	no05a28	86.8	67.5	67.9
43	ELL-14-06	no05a28	87.4	67.9	
44	ELL-14-06	no05a28	88.0	68.4	

Appendix IV. (Cont.)

Analysis I.D.	Sample I.D.	Ablation Analysis	FeO wt. %	Fe wt. %	Avg. Spot Analysis
1	ELL-14-06	no05a06	85.9	66.8	67.4
2	ELL-14-06	no05a06	86.4	67.1	
3	ELL-14-06	no05a07	86.0	66.8	67.2
4	ELL-14-06	no05a07	87.0	67.7	
5	ELL-14-06	no05a07	86.5	67.3	
6	ELL-14-06	no05a08	87.9	68.3	68.0
7	ELL-14-06	no05a08	86.9	67.6	
8	ELL-14-06	no05a08	87.6	68.1	
9	ELL-14-06	no05a09	88.3	68.6	67.8
10	ELL-14-06	no05a09	85.2	66.2	
11	ELL-14-06	no05a09	88.1	68.5	
12	ELL-14-06	no05a10	89.1	69.3	69.4
13	ELL-14-06	no05a10	89.4	69.5	
14	ELL-14-06	no05a10	89.3	69.4	
15	ELL-14-06	no05a11	88.7	68.9	68.5
16	ELL-14-06	no05a11	86.8	67.4	
17	ELL-14-06	no05a11	88.9	69.1	
18	ELL-14-06	no05a12	88.8	69.0	68.8
19	ELL-14-06	no05a12	88.8	69.0	
20	ELL-14-06	no05a12	87.9	68.3	
21	ELL-14-06	no05a13	88.8	69.0	67.9
22	ELL-14-06	no05a13	86.3	67.1	
23	ELL-14-06	no05a13	87.0	67.6	
24	ELL-14-06	no05a14	86.7	67.4	67.5
25	ELL-14-06	no05a14	86.9	67.6	
26	ELL-14-06	no05a14	86.9	67.5	
27	ELL-14-06	no05a15	87.3	67.9	67.2
28	ELL-14-06	no05a15	85.5	66.5	
29	ELL-14-06	no05a15	86.5	67.2	
30	ELL-14-06	no05a23	88.5	68.8	67.9
31	ELL-14-06	no05a23	86.4	67.2	
32	ELL-14-06	no05a23	87.3	67.8	
33	ELL-14-06	no05a24	87.3	67.8	68.9
34	ELL-14-06	no05a24	89.0	69.2	
35	ELL-14-06	no05a24	89.6	69.7	
36	ELL-14-06	no05a26	88.8	69.0	69.0
37	ELL-14-06	no05a26	88.5	68.8	
38	ELL-14-06	no05a26	89.1	69.2	
39	ELL-14-06	no05a27	87.5	68.0	68.0
40	ELL-14-06	no05a27	87.0	67.7	
41	ELL-14-06	no05a27	88.1	68.4	
42	ELL-14-06	no05a28	86.8	67.5	67.9
43	ELL-14-06	no05a28	87.4	67.9	
44	ELL-14-06	no05a28	88.0	68.4	

Appendix IV. (Cont.)

Analysis I.D.	Sample I.D.	Ablation Analysis	FeO wt. %	Fe wt. %	Avg. Spot Analysis
10	ELL-14-05	no05c11	88.4	68.7	69.6
11	ELL-14-05	no05c11	90.7	70.5	
12	ELL-14-05	no05c11	89.6	69.7	
13	ELL-14-05	no05c12	90.0	70.0	69.5
14	ELL-14-05	no05c12	89.9	69.9	
15	ELL-14-05	no05c13	88.4	68.7	68.1
16	ELL-14-05	no05c13	86.6	67.3	
17	ELL-14-05	no05c13	87.7	68.2	
18	ELL-14-05	no05c14	88.1	68.5	68.6
19	ELL-14-05	no05c14	87.0	67.6	
20	ELL-14-05	no05c14	89.5	69.5	
21	ELL-14-05	no05c15	89.4	69.5	69.0
22	ELL-14-05	no05c15	89.2	69.3	
23	ELL-14-05	no05c15	87.5	68.0	
24	ELL-14-05	no05c16	88.7	68.9	69.1
25	ELL-14-05	no05c16	89.1	69.2	
26	ELL-14-05	no05c16	89.0	69.2	
27	ELL-14-05	no05c17	86.6	67.3	67.6
28	ELL-14-05	no05c17	88.3	68.6	
29	ELL-14-05	no05c17	85.9	66.7	
30	ELL-14-05	no05c18	85.3	66.3	67.9
31	ELL-14-05	no05c18	88.9	69.1	
32	ELL-14-05	no05c18	87.8	68.2	
33	ELL-14-05	no05c22	87.5	68.0	68.4
34	ELL-14-05	no05c22	88.1	68.5	
35	ELL-14-05	no05c22	88.2	68.6	
36	ELL-14-05	no05c23	88.2	68.5	68.8
37	ELL-14-05	no05c23	87.6	68.1	
38	ELL-14-05	no05c23	89.9	69.9	
39	ELL-14-05	no05c24	89.1	69.2	69.5
40	ELL-14-05	no05c24	88.8	69.0	
41	ELL-14-05	no05c24	90.3	70.2	
42	ELL-14-05	no05c25	89.3	69.4	69.4
43	ELL-14-05	no05c25	89.4	69.5	
44	ELL-14-05	no05c25	89.1	69.2	
45	ELL-14-05	no05c26	87.9	68.4	69.4
46	ELL-14-05	no05c26	89.8	69.8	
47	ELL-14-05	no05c26	90.0	70.0	
48	ELL-14-05	no05c27	88.8	69.0	69.2
49	ELL-14-05	no05c27	89.2	69.3	
50	ELL-14-05	no05c28	88.1	68.5	68.5
51	ELL-14-05	no05c28	88.2	68.5	

Appendix IV. (Cont.)

Analysis I.D.	Sample I.D.	Ablation Analysis	FeO wt. %	Fe wt. %	Avg. Spot Analysis
45	ELL-14-06	no05a18	89.9	69.9	69.4
46	ELL-14-06	no05a18	88.3	68.7	
47	ELL-14-06	no05a18	89.8	69.8	
48	ELL-14-06	no05a19	89.0	69.1	69.1
49	ELL-14-06	no05a19	89.0	69.2	
50	ELL-14-06	no05a19	89.0	69.0	
51	ELL-14-06	no05a20	85.6	66.5	67.4
52	ELL-14-06	no05a20	89.0	69.1	
53	ELL-14-06	no05a20	86.0	66.7	
54	ELL-14-06	no05a21	89.1	69.2	68.6
55	ELL-14-06	no05a21	86.6	67.3	
56	ELL-14-06	no05a21	89.1	69.3	
57	ELL-14-06	no05a22	85.6	66.5	66.8
58	ELL-14-06	no05a22	86.2	67.0	
59	ELL-14-06	no05a22	86.0	66.9	
1	LAS-14-07	no05d21	79.8	62.0	61.9
2	LAS-14-07	no05d21	79.6	61.9	
3	LAS-14-07	no05d21	79.4	61.7	
4	LAS-14-07	no05d22	79.7	61.9	61.8
5	LAS-14-07	no05d22	79.5	61.8	
6	LAS-14-07	no05d22	79.3	61.6	
7	LAS-14-07	no05d23	78.4	60.9	61.3
8	LAS-14-07	no05d23	78.8	61.3	
9	LAS-14-07	no05d23	79.4	61.7	
10	LAS-14-07	no05d24	79.3	61.6	61.9
11	LAS-14-07	no05d24	79.8	62.1	
12	LAS-14-07	no05d24	79.8	62.0	
13	LAS-14-07	no05d27	79.9	62.1	58.9
14	LAS-14-07	no05d27	79.2	61.5	
15	LAS-14-07	no05d27	68.3	53.1	
16	LAS-14-07	no05d30	79.5	61.8	61.5
17	LAS-14-07	no05d30	79.4	61.7	
18	LAS-14-07	no05d30	78.6	61.1	
19	LAS-14-07	no05d33	80.9	62.9	62.1
20	LAS-14-07	no05d33	80.1	62.3	
21	LAS-14-07	no05d33	78.7	61.2	
22	LAS-14-07	no05d34	80.0	62.1	62.3
23	LAS-14-07	no05d34	79.9	62.1	
24	LAS-14-07	no05d34	80.7	62.7	

Appendix V. LA-ICPMS spot analysis results. Fe (wt. %) is the mean concentrations of three or less EPMA analyses in the vicinity of LA-ICPMS spots. Spot locations are shown on BSE images of magnetite grains in Appendix VI.

Sample	Rock type	Grain #	LA-ICPMS spot	Fe wt. % (EPMA)	^{24}Mg	^{27}Al	^{29}Si	^{31}P	^{34}S	^{44}Ca	^{47}Ti	^{51}V	^{52}Cr	^{55}Mn	^{59}Co	^{60}Ni	^{63}Cu	^{66}Zn
KRN-10-02	high P ore	1	ap22a08	70	113				140			1464		352	94	269		15
		1	ap22a09	70	110				350			1454	33	365	94	244		15
		1	ap22a10	70	2490	38	5870		430			1422	90	384	97	247		21
		1	ap22a11	70	1340		2870					1417		369	95	259		15
		2	ap22a12	70	329		2120	312	940	860	61	1426	87	426	96	255		39
		2	ap22a13	70	202			38	310			1449		372	95	261		18
K-1	high P ore	1	ap22a14	70	840	420	2130					1531		364	120	270		22
		1	ap22a16	70	600	410	2840	42	320		106	1539	51	376	119	269		20
		1	ap22a17	70	18			34			49	1517		361	119	256		14
		1	ap22a25	69	24		940		260			1507	85	347	115	262		15
		2	ap22a26	70	31							1529		366	118	259		17
		2	ap22a27	70	87	124	940		300		76	1504	53	354	114	251		15
		2	ap22a28	70	143	99	800					1552		359	118	256		16
K-2	low P ore	1	ap22a29	70	47			158	180	440	44	884		315	64	166		13
		1	ap22a30	70	50	31	910		520			878	70	318	64	167		13
		1	ap22a31	70	106	43		106	430			892		337	69	163		19
		2	ap22a32	70	115		960		540			883	28	338	66	165		22
		2	ap22a33	70	42				170		74	901		327	67	159		15
		2	ap22a34	70	136	47	970		470		66	880	42	324	65	152		12
		3	ap22a42	70	68				410		70	873		306	66	150		17
		3	ap22a43	70	102				820			890		310	65	158		15
		3	ap22a44	70	39	35			150			889		313	63	181		14
KRN-11-01	high P ore	1	ap22a46	70	20				360		163	1283		379	33			15
		1	ap22a47	70	77	247	800					1284		387	34			18
		2	ap22a48	70	23	70			500			1277	69	467	34			20
		3	ap22a49	70							254	1227	140	377	37			11
		3	ap22a50	70					750			1250		369	37			
		3	ap22a51	70	95	139	4380	297	830			1265		452	37			12
		3	ap22a60	70					620			1260		366	35			16

Appendix V. (Cont.)

Sample	Rock type	Grain #	LA-ICPMS spot	^{71}Ga	^{75}As	^{88}Sr	^{89}Y	^{93}Nb	^{118}Sn	^{139}La	^{140}Ce	^{141}Pr	^{146}Nd	^{147}Sm	^{153}Eu	^{157}Gd	^{159}Tb
KRN-10-02	high P ore	1	ap22a08	5.1	0.7		0.4	0.1		0.4	1.2	0.1	0.6	0.2	0.0		
		1	ap22a09	5.0	1.5		1.0	0.2	0.8	1.0	2.5	0.3	1.4				0.1
		1	ap22a10	6.2	4.0	0.7	3.3	0.4	2.7	3.0	9.0	1.1	4.2	0.9			0.1
		1	ap22a11	5.2	0.9		0.8	0.2		0.4	1.2	0.1	0.4				
		2	ap22a12	5.8	3.8	3.1	4.0	0.8	2.0	11.0	19.3	2.2	7.5	1.4	0.2	1.3	0.2
		2	ap22a13	5.9	1.1	0.8	0.8	0.1		9.2	12.3	0.9	2.5	0.2			
K-1	high P ore	1	ap22a14	1.7			0.3	0.2		0.3	0.7	0.1	0.2				
		1	ap22a16	1.8	1.6	1.6	0.3	0.4	1.1	1.0	2.0	0.3	0.6	0.1			0.0
		1	ap22a17	1.5							0.1						0.0
		1	ap22a25	1.8		0.4				0.1	0.1	0.1	0.6				
		2	ap22a26	1.6							0.3						
		2	ap22a27	1.9			0.3	1.9	1.0	0.1	0.3	0.0	0.2	0.0			
		2	ap22a28	1.7		1.5	0.2	0.2		0.2	0.5		0.3	0.3			
K-2	low P ore	1	ap22a29	11.5		1.1	0.3			4.6	8.1	1.3	2.3	0.7	0.0		
		1	ap22a30	12.3	0.7	0.9	0.1			0.7	2.0	0.2	2.2				0.0
		1	ap22a31	11.7	0.9	3.1	0.4			2.3	2.6	0.2	1.4	0.2			0.1
		2	ap22a32	11.7		1.0	0.1			0.6	1.1	0.5	0.4				
		2	ap22a33	11.8	0.7	0.3	0.4			1.7	3.2	0.3	1.2	0.1			
		2	ap22a34	11.4		0.9	0.2			1.0	1.7	0.2	0.6	0.2			0.0
		3	ap22a42	12.6		1.0				0.3	2.5	0.1	0.3				
		3	ap22a43	11.7		2.9	0.3			1.2	2.2	0.2	0.8				
		3	ap22a44	10.7	0.6	0.3				0.2	0.6	0.1	0.1				
KRN-11-01	high P ore	1	ap22a46	3.1					0.9	0.1	0.2						
		1	ap22a47	2.9						0.3	0.5	0.0		0.1			
		2	ap22a48	3.2							0.0		0.0				0.0
		3	ap22a49	3.8				0.2	2.4		0.5	0.0					
		3	ap22a50	3.3							0.4						
		3	ap22a51	3.3				2.2	7.4					0.1			
		3	ap22a60	4.2													

Appendix V. (Cont.)

Sample	Rock type	Grain #	LA-ICPMS spot	^{163}Dy	^{165}Ho	^{166}Er	^{169}Tm	^{172}Yb	^{175}Lu	^{178}Hf	^{181}Ta	^{197}Au	^{205}Tl	^{208}Pb	^{232}Th	^{238}U
KRN-10-02	high P ore	1	ap22a08											0.2	0.2	0.1
		1	ap22a09	0.2	0.0	0.0		0.0		0.0				0.5	0.7	0.3
		1	ap22a10	0.5	0.1	0.2		0.1						3.7	2.2	0.4
		1	ap22a11	0.1	0.0					0.0				2.5	0.5	0.3
		2	ap22a12	0.7	0.1	0.3	0.0	0.1	0.0					2.2	1.9	1.0
		2	ap22a13	0.1	0.0									0.6	1.9	0.0
K-1	high P ore	1	ap22a14		0.0	0.0							0.0		0.0	0.1
		1	ap22a16				0.0	0.0		0.0	0.1			0.3	0.4	0.6
		1	ap22a17													0.0
		1	ap22a25									0.0		0.1	0.0	0.0
		2	ap22a26							0.0					0.0	0.1
		2	ap22a27			0.0		0.0			0.1				0.1	0.1
		2	ap22a28	0.0	0.0	0.0							0.0	0.7	0.1	0.2
K-2	low P ore	1	ap22a29	0.2		0.0		0.0						0.3	0.7	0.0
		1	ap22a30	0.0									0.0	0.4	0.5	
		1	ap22a31	0.1		0.0	0.0							0.3	0.4	0.1
		2	ap22a32	0.0				0.0						1.0	0.3	0.1
		2	ap22a33				0.0					0.0	0.0	0.5	1.4	0.1
		2	ap22a34	0.0						0.0				0.3	0.5	0.0
		3	ap22a42	0.0									0.0	0.4	0.3	0.0
		3	ap22a43					0.0						0.1	1.0	0.1
		3	ap22a44					0.0						0.2	0.2	0.0
KRN-11-01	high P ore	1	ap22a46	0.0												0.0
		1	ap22a47									0.0		0.2	0.0	0.0
		2	ap22a48											0.1	0.0	
		3	ap22a49													
		3	ap22a50													
		3	ap22a51	0.0			0.1	1.3					0.0			0.6
		3	ap22a60													

Appendix V. (Cont.)

Sample	Rock type	Grain #	LA-ICPMS spot	Fe wt. % (EPMA)	^{24}Mg	^{27}Al	^{29}Si	^{31}P	^{34}S	^{44}Ca	^{47}Ti	^{51}V	^{52}Cr	^{55}Mn	^{59}Co	^{60}Ni	^{63}Cu	^{66}Zn
KRN-11-03	andesite	1	ap22a80	70	41				250			803	85	585	35			29
	(LA-FW)	1	ap22a81	70	54							802	60	640	35			33
		1	ap22a82	70	94	106	730	20	360			790	96	600	35			33
		2	ap22a83	70	66	112	970					735	76	621	35			24
		2	ap22a84	70	69	74						731	79	627	33			23
KRN-11-04	andesite	1	ap22a85	70	90	33	810					977	52	370	42	52		20
	(A-FW)	1	ap22a86	71	31							996		383	45			15
		1	ap22a87	71	20		620		380			989	96	388	45	35		12
		1	ap23a05	70	15		820				50	986	91	364	44	41		15
		1	ap23a06	70	39						85	983		363	42	25		17
		2	ap23a07	70	112	64	1380		460	660	71	992		374	43	34		22
		2	ap23a08	70	320	180					67	976		391	43	30		20
KRN-11-05	rhyodacite	1	ap23a09	70		37	1600	31	390			167	101	288	23			7
	(HW)	2	ap23a10	70		129			250			185		272	24			6
KRN-12-02	aplite vein		ap23a11	70	56					330		1801		282	37	64		16
			ap23a12	70			850	36	430		50	1727	103	296	38	44		19
			ap23a13	70	31	44			220			1705	44	245	36	54		14
KRN-12-03	syenite	1	ap23a14	70	77	116	2970	37	670			885	83	341	41			24
		1	ap23a24	70					230			955		448	43			32
		1	ap23a25	70			1220		290			943	68	417	42			30
		2	ap23a27	70	19				260	360	42	966		438	43			36
		2	ap23a28	70	123		2230		490	500	204	967	128	443	44			35
		3	ap23a29	70								1023		440	44			33
		3	ap23a30	70	16							1012		472	44			36
KRN-12-05	granite	1	ap23a31	70			1130	355	1400	1050		296	437	87	12		23	13
		2	ap23a40	70	39	166		36	350			351	424	102	8		5	9
TUV-10-03	rhyodacite	1	ap23a61	70	15	43			260			654	47	228	70	84		5
	host	2	ap23a63	70	13				250			555		253	84	69		7

Appendix V. (Cont.)

Sample	Rock type	Grain #	LA-ICPMS spot	^{71}Ga	^{75}As	^{88}Sr	^{89}Y	^{93}Nb	^{118}Sn	^{139}La	^{140}Ce	^{141}Pr	^{146}Nd	^{147}Sm	^{153}Eu	^{157}Gd	^{159}Tb
KRN-11-03	andesite	1	ap22a80	17.8													
	(LA-FW)	1	ap22a81	18.4		0.5				0.1	0.3	0.0	0.7				
		1	ap22a82	18.5		5.7	0.2	0.1		0.3	0.1		0.0				0.3
		2	ap22a83	14.7		0.3				0.5	0.4			0.1			
		2	ap22a84	15.5			0.9			0.2	0.2	0.1					
KRN-11-04	andesite	1	ap22a85	9.7		1.0											
	(A-FW)	1	ap22a86	10.4						0.2							
		1	ap22a87	9.5							0.2		0.0				
		1	ap23a05	9.8					0.5								
		1	ap23a06	10.0		0.8				0.3	0.2	0.1			0.1		
		2	ap23a07	10.6		1.7				0.1	0.3	0.1	0.3	0.1			
		2	ap23a08	10.3							0.2	0.0					
KRN-11-05	rhyodacite	1	ap23a09	7.9							0.1	0.0					
	(HW)	2	ap23a10	6.0			1.1			0.1	0.1		0.2				
KRN-12-02	aplite vein		ap23a11	14.6		0.9					0.0		0.1	0.1			
			ap23a12	13.0		1.3				0.2	0.3		0.1				
			ap23a13	14.0		2.0	0.2			0.3	0.3		0.4				
KRN-12-03	syenite	1	ap23a14	4.8			0.2			0.7	0.3		0.2				
		1	ap23a24	4.5						0.1							
		1	ap23a25	4.2							0.1		0.1				
		2	ap23a27	4.1		0.7	0.1			0.1	0.1		0.1				
		2	ap23a28	4.3		0.8	2.2	0.3		0.4	1.7	0.1					0.1
		3	ap23a29	4.4		0.7	0.1				0.1						
		3	ap23a30	4.3		0.6	0.1			0.1							
KRN-12-05	granite	1	ap23a31	10.3			0.4			1.9	5.2	0.4	1.5		0.1		
		2	ap23a40	11.2						0.4	0.4						
TUV-10-03	rhyodacite	1	ap23a61	14.4							0.1		0.1				
	host	2	ap23a63	12.8						0.1							

Appendix V. (Cont.)

Sample	Rock type	Grain #	LA-ICPMS spot	^{163}Dy	^{165}Ho	^{166}Er	^{169}Tm	^{172}Yb	^{175}Lu	^{178}Hf	^{181}Ta	^{197}Au	^{205}Tl	^{208}Pb	^{232}Th	^{238}U
KRN-11-03	andesite	1	ap22a80											0.1	0.0	0.0
	(LA-FW)	1	ap22a81							0.0					0.0	0.0
		1	ap22a82											0.1	0.0	0.0
		2	ap22a83	0.0						0.0						0.0
		2	ap22a84											1.0	0.0	0.0
KRN-11-04	andesite	1	ap22a85											0.3		
	(A-FW)	1	ap22a86			0.0				0.0					0.0	0.0
		1	ap22a87												0.0	0.0
		1	ap23a05											0.1	0.0	
		1	ap23a06										0.0	0.1	0.0	0.0
		2	ap23a07				0.0					0.0	0.0	0.2	0.2	0.1
		2	ap23a08	0.0						0.0				0.2	0.0	0.0
KRN-11-05	rhyodacite	1	ap23a09											0.1		0.0
	(HW)	2	ap23a10	0.2	0.0	0.2		0.5	0.1	1.9	0.0			0.1	0.1	0.8
KRN-12-02	aplite vein		ap23a11											0.2	0.0	
			ap23a12	0.1											0.0	0.0
			ap23a13											0.5	0.0	0.0
KRN-12-03	syenite	1	ap23a14											0.4	0.0	0.1
		1	ap23a24		0.0											0.0
		1	ap23a25													0.0
		2	ap23a27											0.2	0.2	
		2	ap23a28	0.3	0.1	0.4	0.1	1.1	0.3	6.7				1.1	4.4	2.6
		3	ap23a29			0.0									0.0	0.0
		3	ap23a30		0.0			0.0							0.0	0.0
KRN-12-05	granite	1	ap23a31												0.1	
		2	ap23a40											0.3	0.0	
TUV-10-03	rhyodacite	1	ap23a61											0.9	0.0	0.0
	host	2	ap23a63							0.0				0.4	0.1	

Appendix V. (Cont.)

Sample	Rock type	Grain #	LA-ICPMS spot	Fe wt. % (EPMA)	^{24}Mg	^{27}Al	^{29}Si	^{31}P	^{34}S	^{44}Ca	^{47}Ti	^{51}V	^{52}Cr	^{55}Mn	^{59}Co	^{60}Ni	^{63}Cu	^{66}Zn
TUV-10-01	ore	1	ap22a67	70	195	224	1190	35	730			543		402	119	206		9
		1	ap22a68	71	191	366	920	36	530			553		366	122	213		4
		1	ap22a69	71	214	126		32	190			557		407	122	212		12
		2	ap22a77	71	228	81			260			550		405	120	214		13
		2	ap22a78	71	193	70			350			547		372	119	203		9
		2	ap22a79	71	305	132			210			546		378	122	197		12
NUK-10-03	ore	1	ap23a41	70	36		1160	29	740			1080	59	140	128	309		15
		1	ap23a42	71	128	142			320		358	1093		147	126	301	9	26
		1	ap23a43	70	25		960		410		231	1072		145	128	299		20
		1	ap23a44	70					670		1970	1082	180	165	138	278		28
		2	ap23a45	70	31				420			1054		150	130	320		24
		2	ap23a46	70								1068		148	128	302		18
NUK-12-02	ore + host	1	ap23a47	70					340		321	937		59	123	160		14
		1	ap23a48	70	106	126					4380	942		61	128	166		17
		1	ap23a49	70	88	35	1660	52	660	580	2640	931	137	75	125	185		27
		2	ap23a58	70	92	106					1710	954	61	63	131	173		23
		2	ap23a59	70	138	490	1690		250		1770	946	118	62	128	185		20
		2	ap23a60	70	90	43	770					929	145	55	127	188		17
REK-10-01	rhyodacite	1	ap23a64	67		61	2220		600		4360	605	110	16	3			
		1	ap23a65	67		155		42			4532	607		16	3		7	
		1	ap23a66	67	17	155	1000	36			5150	616	75	22	3			
		2	ap23a67	67		107	720	34	420		5040	601		13	3		4	
		2	ap23a75	67			3440		870		4160	593		16	3			
REK-10-04	ore	1	ap22a61	64	87	109					29720	2001		77	12			3
		1	ap22a62	65	61	146			370		22250	1771	56	62	8			
		1	ap22a63	69	67	431	870	27	650		9550	1396		46	7	61	261	5
		2	ap22a64	70	186	700	2530	79	550	400	65	937	72	61	6	373	11	7
		3	ap22a65	66	21	166						896		40	3	338		
		3	ap22a66	70	13				250		510	960		54	2	339		3
REK-12-02	rhyodacite	1	ap23a76	70								229	56	34	70	81		5
		1	ap23a77	70					360		1120	233		36	70	74		6
		1	ap23a78	70	210				460			225		41	65	66		11
		2	ap23a79	70	23							228		40	77	72		3
		3	ap23a80	71	20				170			239	50	41	74	102		3
		3	ap23a81	70	31							236		42	69	76		3

Appendix V. (Cont.)

Sample	Rock type	Grain #	LA-ICPMS spot	^{71}Ga	^{75}As	^{88}Sr	^{89}Y	^{93}Nb	^{118}Sn	^{139}La	^{140}Ce	^{141}Pr	^{146}Nd	^{147}Sm	^{153}Eu	^{157}Gd	^{159}Tb
TUV-10-01	ore	1	ap22a67	27.2						0.1	0.0	0.0		0.1			
		1	ap22a68	27.7			0.2			0.2	0.2	0.3					
		1	ap22a69	28.1	1.4	2.0					0.3						
		2	ap22a77	28.5		0.5				0.3	1.0						
		2	ap22a78	27.0		0.5	0.2					0.1	1.6				
		2	ap22a79	28.6		2.0	0.1			0.2	0.3						
NUK-10-03	ore	1	ap23a41	20.5			0.3			0.1	0.4		0.3				
		1	ap23a42	22.8	1.0	0.4	1.9		0.9	1.5	3.9	0.4	1.9	0.3			
		1	ap23a43	21.2			0.1	0.2		0.1	0.3						
		1	ap23a44	28.2			1.9	0.4	2.0	95.0	137.0	7.4	18.1	2.1			0.2
		2	ap23a45	21.8		1.3				0.3	0.2						
		2	ap23a46	21.6						0.3	0.4	0.1					
NUK-12-02	ore + host	1	ap23a47	5.9		2.5	0.4	0.3		0.9	1.9	0.4	0.5				
		1	ap23a48	6.0	1.3	1.7	0.5	4.9		0.6	1.1	0.1	0.6				
		1	ap23a49	6.0	1.7	5.4	0.8	2.9		2.3	2.9	0.3	1.3	0.2	0.1		0.0
		2	ap23a58	6.3	1.3	5.4	0.9	1.7		3.0	6.5	0.4	1.8	0.3			
		2	ap23a59	6.1	1.1	3.9	0.8	2.2		2.3	4.4	0.5	1.0				0.1
		2	ap23a60	5.2		5.1	0.3			1.2	2.4	0.3	1.1	0.2			0.0
REK-10-01	rhyodacite	1	ap23a64	4.2	15.0		1.0	0.8	2.5	4.1	5.4	0.4	0.9				
		1	ap23a65	3.6	15.9	1.0	1.9	1.1	2.1	5.2	5.4	0.5	1.3	0.2			
		1	ap23a66	3.3	36.9	1.0	2.2	2.2	1.8	5.5	6.2	0.5	1.6	0.4	0.2	0.7	0.1
		2	ap23a67	3.6	2.9		0.3	0.4	1.7	4.8	4.3	0.6	1.0	0.2			
		2	ap23a75	3.3	27.3	1.2	1.5	1.6	2.6	3.3	4.5	0.6	0.7				0.1
REK-10-04	ore	1	ap22a61	9.6			0.1	0.5	6.0	0.3	0.3			0.1			
		1	ap22a62	10.4		1.7	0.2	0.8	4.8	0.3	0.7	0.1	0.6				
		1	ap22a63	16.7	3.2	2.2	1.2	1.3	3.4	2.2	3.8	0.4	1.4	0.2			
		2	ap22a64	30.1	2.2	4.2	2.4			17.0	21.8	2.3	5.7	1.2	0.3	0.7	0.1
		3	ap22a65	23.5						0.1	0.5						
		3	ap22a66	27.3			0.5	0.2		0.6	1.4	0.2	0.6				
REK-12-02	rhyodacite	1	ap23a76	1.7													
		1	ap23a77	1.7				1.0					0.2				
		1	ap23a78	1.5						0.2	0.1						
		2	ap23a79	1.7							0.1						
		3	ap23a80	1.8													
		3	ap23a81	2.1													

Appendix V. (Cont.)

Sample	Rock type	Grain #	LA-ICPMS spot	^{163}Dy	^{165}Ho	^{166}Er	^{169}Tm	^{172}Yb	^{175}Lu	^{178}Hf	^{181}Ta	^{197}Au	^{205}Tl	^{208}Pb	^{232}Th	^{238}U
TUV-10-01	ore	1	ap22a67	0.0				0.0							0.0	0.0
		1	ap22a68											0.1	0.1	0.1
		1	ap22a69		0.0					0.0				0.3	0.0	0.0
		2	ap22a77											0.3	0.1	0.0
		2	ap22a78					0.0						0.3	0.1	0.0
		2	ap22a79											0.1	0.3	0.1
NUK-10-03	ore	1	ap23a41				0.0							0.1	0.1	
		1	ap23a42	0.2		0.3		0.3						0.4	0.4	0.2
		1	ap23a43											0.7	0.2	0.1
		1	ap23a44	0.5	0.1									2.2	7.2	1.2
		2	ap23a45											0.1	0.1	0.0
		2	ap23a46										0.0	0.1	0.0	0.0
NUK-12-02	ore + host	1	ap23a47	0.3	0.0			0.0						1.1	0.1	0.2
		1	ap23a48								0.2		0.0	0.7	0.3	1.9
		1	ap23a49	0.2	0.0	0.1					0.2			3.6	0.6	1.0
		2	ap23a58	0.3	0.0					0.0	0.1			4.2	0.4	0.8
		2	ap23a59	0.3		0.1					0.1			3.1	0.2	0.5
		2	ap23a60		0.0	0.1				0.0				1.3	0.3	0.2
REK-10-01	rhyodacite	1	ap23a64		0.1					0.1				1.7	0.4	8.4
		1	ap23a65	0.3	0.1	0.2	0.0	0.3		2.7	0.3		0.0	3.2	0.8	11.6
		1	ap23a66	1.0	0.1	0.4		0.2		0.0	0.4			4.1	1.5	50.9
		2	ap23a67			0.0				0.1	0.1			1.0	0.2	1.0
		2	ap23a75	0.4	0.1					1.6				3.3	0.6	14.1
REK-10-04	ore	1	ap22a61								0.0	0.0			0.1	0.8
		1	ap22a62			0.0				0.1				0.1	0.1	0.5
		1	ap22a63	0.2		0.1		0.2	0.0		0.1			2.0	1.4	5.1
		2	ap22a64	0.4	0.1	0.2		0.1						2.6	2.9	1.3
		3	ap22a65						0.0				0.0	0.1	0.0	0.1
		3	ap22a66	0.1	0.0	0.1								0.7	0.1	1.6
REK-12-02	rhyodacite	1	ap23a76					0.0						0.1		0.0
		1	ap23a77											0.3	0.0	0.1
		1	ap23a78					0.0						0.4	0.0	0.0
		2	ap23a79		0.0											
		3	ap23a80			0.0										
		3	ap23a81			0.0										0.0

Appendix V. (Cont.)

Sample	rock type	Grain #	LA-ICPMS spot	Fe wt. % (EPMA)	^{24}Mg	^{27}Al	^{29}Si	^{31}P	^{34}S	^{44}Ca	^{47}Ti	^{51}V	^{52}Cr	^{55}Mn
ELL-14-02	andesite host	1	no05b09	63	2403	6050		85			62100	3168	664	3723
		1	no05b10	61	3310	6370	4100				62100	3050	775	4690
		1	no05b11	66	2088	5040					56500	3167	839	3360
		2	no05b12	66	2410	5210		142	680		59800	3122	842	3570
		2	no05b13	66	4690	5420		1600			70900	2990	590	4210
		2	no05b14	65	3430	4840	6060		1370		64600	2951	748	5040
		3	no05b15	63	1438	3730					56300	2809	700	3523
		3	no05b16	64	3250	4600	2930				91000	2721	630	5060
		3	no05b17	64	2147	9340		1860	2500		57300	3160	837	3786
		4	no05b18	64	2516	1027					66100	3241	772	3915
		4	no05b19	59	2220	8870			390		57400	2926	739	3484
		4	no05b20	62	2089	8980					64000	3010	718	3839
		4	no05b21	64	2030	5270		470			70600	2616	646	4372
		5	no05b22	64	2162	5490					80100	2708	503	4839
		5	no05b23	62	2219	5550		287			70000	2571	642	4465
ELL-14-04	vuggy ore	1	no05d05	66	745	1681	4580	240			405	1929		53.9
		1	no05d06	67	842	1543			470		273	1938		43.2
		1	no05d07	69	438	1526	3600	253			285	1944		23.7
		2	no05d08	70	8580	1808					234	1934		321
		2	no05d09	70	8040	1572		100			284	1947		385.5
		2	no05d10	70	7960	1601					278	1871		351
		3	no05d11	70	7250	1638	3060	106	1260		239	1873	100	310
		3	no05d12	70	7770	1737		137			349	1967		354
		3	no05d13	70	7790	1626		124			307	1961		417
		3	no05d14	70	7070	1613		100			224	1804		306
		4	no05d17	70	8170	1645					301	1810		234.5
		4	no05d18	69	7860	1611					209	1771		333.5
		4	no05d19	70	11440	1733	6440	182			366	1760		313
		4	no05d20	70	8660	1653	3210	182	470		281	1843		412

Appendix V. (Cont.)

Sample	rock type	Grain #	LA-ICPMS spot	^{59}Co	^{60}Ni	^{63}Cu	^{66}Zn	^{71}Ga	^{72}Ge	^{75}As	^{88}Sr	^{89}Y	^{93}Nb	^{95}Mo
ELL-14-02	andesite host	1	no05b09	127.7	223	23.5	847	52.3				1.72	14.2	
		1	no05b10	123.5	241	25.5	2210	48.7				1.23	13.59	
		1	no05b11	123	305	31.4	1251	53.5				1.22	15.1	
		2	no05b12	121.5	281	35.8	1212	50.6				1.21	11.99	
		2	no05b13	128.4	274		1103	51.5			3.1	2.33	17	
		2	no05b14	124.4	196	96.1	1691	49.6			1.03	1.26	24.5	
		3	no05b15	107.2	152	24.2	844	45.2				0.98	19.79	
		3	no05b16	114.7	155	23.9	1164	44.6			0.69	1.44	31.1	
		3	no05b17	127.4	226	24	3060	57			3.29	4.2	8.9	
		4	no05b18	131.1	188	19.6	1659	51.3				1.65	11.44	
		4	no05b19	118.9	176	23.1	2780	50.7				1.05	9.57	
		4	no05b20	126.2	174	17.8	1666	46.8				1.55	10.7	
		4	no05b21	101.4	132	17.6	1468	45.2			1.23	1.53	30.9	
		5	no05b22	101.9	139	16.9	1850	44.3				1.4	37	
		5	no05b23	101.4	140	18.3	1967	44.6			1.66	1.32	32.7	
ELL-14-04	vuggy ore	1	no05d05	21.2	572			6.75		27.3				
		1	no05d06	23.1	427			6.45						
		1	no05d07	16.3	430			6.55		17.5			0.52	3.6
		2	no05d08	147.3	469		56	6.22			1.35		0.81	
		2	no05d09	149.4	414		53.5	6.04						
		2	no05d10	146.2	435		37.3	6.12					0.007	
		3	no05d11	143.7	409		46.5	5.86					0.44	
		3	no05d12	150.3	443		62.5	5.99					1.58	
		3	no05d13	146.7	456		57.8	5.65					0.42	
		3	no05d14	147.1	381		50	5.49					0.55	
		4	no05d17	144	418		60.5	7.1					0.19	
		4	no05d18	144.3	463		53.8	6.11					0.27	
		4	no05d19	143	424		42.5	7.84			1.52	1.99	8.27	
		4	no05d20	144.9	397		46.4	6.23			1.9	0.23	3.92	

Appendix V. (Cont.)

Sample	rock type	Grain #	LA-ICPMS spot	^{107}Ag	^{115}In	^{118}Sn	^{121}Sb	^{138}Ba	^{140}Ce	^{181}Ta	^{184}W	^{197}Au	^{205}Tl	^{208}Pb	^{232}Th
ELL-14-02	andesite	1	no05b09			6.93			2.57	0.46					
	host	1	no05b10			6.8		13.2	7.22	0.39	1.87			1.79	0.51
					0.20										
		1	no05b11		1	10.2			3.24	0.72	0.125		0.015		0.136
		2	no05b12	0.013		10.4			2.69	0.32	0.024			0.48	0.044
		2	no05b13			17.8		20.1	9.6		0.32			1	0.061
		2	no05b14			6.34		24.8	10	0.6	4.39		0.02	3.48	1.38
		3	no05b15			5.95			3.01	0.5				0.52	
		3	no05b16			6.77		12.4	16.8	0.84	2.6			3.06	0.93
		3	no05b17						11.9	0.79					0.056
		4	no05b18			6.51			1.82	0.6					
		4	no05b19			7.8			3.08	0.39	0.121				0.178
		4	no05b20			7.5			0.72	0.33					
		4	no05b21			8.9		2.35	8.3	0.71	0.23		0.016		0.4
		5	no05b22			6.9		1.12	8.51	0.93	0.24			1.18	0.4
		5	no05b23					11.6	10.2		0.57		0.008	1.89	0.84
ELL-14-04	vuggy	1	no05d05			17.7		5.1	0.61		4.02			0.57	0.018
	ore	1	no05d06			14.4		2.77	0.082				0.009		
		1	no05d07			15.5		2.32	0.56		4.2				0.026
		2	no05d08			15.2		2.01	1.28						0.83
		2	no05d09			11.6									0.165
		2	no05d10			14.8					0.07				0.051
		3	no05d11			12.4			0.151						
		3	no05d12			13.8			0.64						0.49
		3	no05d13			14							0.022		0.054
		3	no05d14			16.4			0.36						0.03
		4	no05d17			13									0.015
		4	no05d18			15.6									0.0059
		4	no05d19			15.9		3.03	7.85	0.7			0.006		1.78
		4	no05d20			13.3		1.86	3.41	0.32				0.56	0.57

Appendix V. (Cont.)

Sample	rock type	Grain #	LA-ICPMS spot	Fe wt. % (EPMA)	^{24}Mg	^{27}Al	^{29}Si	^{31}P	^{34}S	^{44}Ca	^{47}Ti	^{51}V	^{52}Cr	^{55}Mn
ELL-14-05	vesicular ore	1	no05c08	70	13740	1796	9700	124	410			1002		481
		1	no05c09	68	14420	2209	13500			2520	215	1045		532
		1	no05c10	69	12900	1715	9300			2070	239	1030		485
		1	no05c11	70	9110	1099					162	960		403
		2	no05c12	70	9580	2240	8000	365	350			999		245
		2	no05c13	68	9640	1470						1068		388
		2	no05c14	69	9060	1586	7560	199	700			1045	55	433
		2	no05c15	69	10970	1474	5720					1059		470
		3	no05c16	69	8980	1326	4000				149	878		407
		3	no05c17	68	7800	1337	3920	162			238	898		288
		3	no05c18	68	8700	1478	4400				113	873		325
		4	no05c22	68	12400	1771	11700			2940	373	1016		494
		4	no05c23	69	9270	1460	7710		420		424	939		462
		4	no05c24	69	10170	1343					580	1032		485
		4	no05c25	69	8970	1092	4170				332	1056		463
		5	no05c26	69	5720	891	3410	170			204	1032	54	307
		5	no05c27	69	6450	746						1000		304.2
		5	no05c28	68	5390	838		182				996		267
ELL-14-06	vein ore	1	no05a06	67	3400	167		297	720		350	614	65	261
		1	no05a07	67	2640	206	4110	843	320		270	630		209
		1	no05a08	68	5420	106	2720	417	650			602		260.6
		1	no05a09	68	7610	77	6750	318		1730	460	553		362
		1	no05a10	69	8840		6390	171	640	1980		561	132	406.7
		1	no05a11	68	6150			132				578		311.5
		1	no05a12	69	7220		6470	330	780	1780		586	57	340
		1	no05a13	68	5820	79	4910	253	680			638		315.8
		1	no05a14	67	422	83	2120	96	1380		460	774		39.3
		1	no05a15	67	4040			295	1140			666	54	304.3

Appendix V. (Cont.)

Sample	rock type	Grain #	LA-ICP -MS spot	^{59}Co	^{60}Ni	^{63}Cu	^{66}Zn	^{71}Ga	^{72}Ge	^{75}As	^{88}Sr	^{89}Y	^{93}Nb	^{95}Mo
ELL-14-05	vesicular ore	1	no05c08	176	426			1.7			1.4	1.2	3.6	
		1	no05c09	162	416		63	2.7			2.9	1.6	3.7	
		1	no05c10	163	446		52.6	2.3			1.6	1.2	3.4	
		1	no05c11	160	483		36.8	1.9					0.02	
		2	no05c12	159	447	39	38.9	1.7			2.4		1.9	8.5
		2	no05c13	168	462		58	3.4				0.7	2.1	
		2	no05c14	163	441	23	67	3.2			2.3	2.8	3.2	
		2	no05c15	149	419		49.9	1.7				0.46	1.6	
		3	no05c16	141	408		31.8	1.5				0.47	1.6	
		3	no05c17	153	414	31	40.1	1.7			1.7	0.69	2.8	
		3	no05c18	149	459	14	34.5	2.1			1.2	0.93	1.9	
		4	no05c22	133	400		66	2.2			2.0	1.43	3.5	
		4	no05c23	138	434		65	1.7			1.2	0.94	3.5	
		4	no05c24	129	409							0.52	2.1	
		4	no05c25	131	421		55					0.53	1.1	
		5	no05c26	155	467	14	39.2	1.4			1.8	0.42	1.1	10
		5	no05c27	136	451			1.9					1.7	
		5	no05c28	143	403	13		1.7			1.9	0.55	2.2	9.8
ELL-14-06	vein ore	1	no05a06	113	290	13	55					0.73	0.36	
		1	no05a07	95	281		54.8			11	1.9	6.2	10	
		1	no05a08	107	291	15	38.9					0.6	1.54	
		1	no05a09	122	256		60.4	1.4		31	4.3	9.96	21.2	
		1	no05a10	126	273		52.3	0.9		26	4.0	8.23	17.7	
		1	no05a11	116	243		47.7			8.3	1.1	1.37	3.85	
		1	no05a12	120	263		58.7	1.26		22	3.4	6.63	13.0	
		1	no05a13	110	256		54	0.66		17	2.3	4.91	11.7	
		1	no05a14	64	265							0.41	1.99	
		1	no05a15	110	235		47	0.56				0.54	1.3	

Appendix V. (Cont.)

Sample	rock type	Grain #	LA-ICPMS spot	^{107}Ag	^{115}In	^{118}Sn	^{121}Sb	^{138}Ba	^{140}Ce	^{181}Ta	^{184}W	^{197}Au	^{205}Tl	^{208}Pb	^{232}Th
ELL-14-05	vesicular	1	no05c08			15.9		1.23	10.7	0.53					0.49
	ore	1	no05c09			13.7		2.13	11.49						1.25
		1	no05c10			14.4		1.63	8.1					0.76	0.54
		1	no05c11	0.1		13.9							0.009		
		2	no05c12			13.9		3.17	2.85				0.061	4.6	1.39
		2	no05c13			13.5		2.67	3.36					2.02	1.45
		2	no05c14			15.6		1.99	56.2					3.84	8.3
		2	no05c15			9.8			2.95						0.134
		3	no05c16			10			1.33						0.048
		3	no05c17			12.7		3.95	3.56					2.55	1.29
		3	no05c18			13.5		1.83	3.81					0.93	1.06
		4	no05c22			12.2		1.55	9.8						1.2
		4	no05c23			12.4		1.09	5.22						0.92
		4	no05c24	0.037			0.26		4.72	0.07				0.185	0.18
		4	no05c25			9.8			1.93						
		5	no05c26			10.6		3.93	2.88					8.9	0.5
		5	no05c27			15.9			0.78		0.16		0.012	4.65	0.9
		5	no05c28			10.3		2.74	3.04					5.8	1.34
ELL-14-06	vein ore	1	no05a06			12.7			17.4						0.034
		1	no05a07			13.9		2.58	24.2		0.53			0.31	13
		1	no05a08			13.3		0.94	6.8				0.007		1.53
		1	no05a09		0.211	13.22	3.86	5.17	68.9	0.36	0.8				35.7
		1	no05a10			11.7	4	4.23	53.9	0.17	0.65				29.8
		1	no05a11			11.9		1.55	13.7		0.075				6.74
		1	no05a12			12.84		3.42	55.2	0.27	0.48			0.197	22.14
		1	no05a13		0.17	13.11		2.54	30.5	0.15	0.45				15.6
		1	no05a14			12.84			2.44						0.292
		1	no05a15			14.01			4.72						0.157

Appendix V. (Cont.)

Sample	rock type	Grain #	LA-ICPMS spot	Fe wt. % (EPMA)	^{24}Mg	^{27}Al	^{29}Si	^{31}P	^{34}S	^{44}Ca	^{47}Ti	^{51}V	^{52}Cr	^{55}Mn
ELL-14-06	vein ore	2	no05a18	69	9200		7490	85	280	2750	1290	538.4		399.3
		2	no05a19	69	8160	56	6790	327		1570		521		348.4
		2	no05a20	67	5940		4800	220			280	545		291
		2	no05a21	69	4950	82	5950	404	730			555		234
		2	no05a22	67	2120	74	3300	500	970			541		149
		3	no05a23	68	2265	156	3350	920	500	1130	930	570		150.3
		3	no05a24	69	5440		2430	71			96	570		313.3
		3	no05a26	69	6700		5770	570	650	1780		550	54	303
		3	no05a27	68	1979	113		1262	1230			571		168.7
		3	no05a28	68	4820			830	800			557		250.1
LAS-14-07	pyroclastic dacite	1	no05d21	61	13430	13710		2140	650	5500	79800	4683	747	4345
		1	no05d22	61	13680	13350		2940	770	5960	79100	4605	811	4304
		1	no05d23	60	13450	13690		500	910	1760	79000	4496	773	4174
		1	no05d24	61	13790	13550		291	640		81600	4631	847	4309
		2	no05d27	57	15080	7650					11320	5250	795	3930
		3	no05d30	61	14780	10850		70			77800	4820	771	3907
		4	no05d33	61	15320	15000	9500				75900	4080	916	3816
		4	no05d34	61	15990	12990			550		77600	4030	914	3955

Appendix V. (Cont.)

Sample	rock type	Grain #	LA-ICPMS spot	^{59}Co	^{60}Ni	^{63}Cu	^{66}Zn	^{71}Ga	^{72}Ge	^{75}As	^{88}Sr	^{89}Y	^{93}Nb	^{95}Mo
ELL-14-06	vein ore	2	no05a18	117.1	299		63	1.12		24.2	4.24	7.42	17.8	
		2	no05a19	121.6	307		55.6	1.36		39.2	5.26	10.36	26.5	
		2	no05a20	112.6	301		38	1.97		28.2	3.35	7.34	15.5	
		2	no05a21	111	297			0.9		16.3	3.16	5.69	14.5	
		2	no05a22	103.9	250		49.7	0.93		19.4	1.98	5.47	15.6	
		3	no05a23	108.3	334		61	1.24		13.2	3.15	5.31	18	
		3	no05a24	159	279		54.2			6.5	1.42	2.55	5.84	
		3	no05a26	114.2	266.6	40	47.8	1.33		26.8	4.21	9.02	25.1	
		3	no05a27	68.1	249		50.6			9.9	1.73	3.42	9.22	
		3	no05a28	124	255	76	44			17	2.76	4.63	11.1	
LAS-14-07	pyroclastic	1	no05d21	264.3	496	54.6	1127	68			6.8	19.4	20.2	5.8
	dacite	1	no05d22	264.5	320	54.9	1151	70.4			8.6	26.1	20.1	
		1	no05d23	252.6	263	50.9	1087	63.9			4.2	5.8	19.3	
		1	no05d24	263.8	279	48.7	1009	67.8				1.06	20.5	4.9
		2	no05d27	214.8	340	50.1	1309	52.9				1.24	99.3	13.1
		3	no05d30	236	373	63.3	1665	66.4					5.35	6.7
		4	no05d33	246.6	368	51.3	1408	68.1			11		14.1	
		4	no05d34	242	382	46.2	1277	61.6					15.3	

Appendix V. (Cont.)

Sample	rock type	Grain #	LA-ICPMS spot	^{107}Ag	^{115}In	^{118}Sn	^{121}Sb	^{138}Ba	^{140}Ce	^{181}Ta	^{184}W	^{197}Au	^{205}Tl	^{208}Pb	^{232}Th
ELL-14-06	vein ore	2	no05a18			13.8		4.16	48.7	0.233	0.28				24.4
		2	no05a19		0.198	16.71	4.97	5.51	68.3	0.35	0.65				34.5
		2	no05a20			15.4		4.23	51		0.31				26.7
		2	no05a21			12.66	2.27	4.18	40.8	0.24	0.59			0.25	23.3
		2	no05a22		0.245	14.2		2.41	50.6		0.38		0.0025		24.2
		3	no05a23		0.149	17.2		6.3	48.4		0.42				21.8
		3	no05a24			10.5		1.61	17.07	0.164	0.081	0.06			9.09
		3	no05a26		0.153	12.8	3.44	5.71	57.7	0.31	0.47				31.5
		3	no05a27			14.8		3.43	25.2		0.08				12.14
		3	no05a28			13.8		3.81	36.7		0.3		0.005		18.26
LAS-14-07	pyroclastic dacite	1	no05d21			27.6			44.8	0.81	0.32				3.49
		1	no05d22			27.4		1.57	61.8	0.78	0.36				4.63
		1	no05d23			25			13.9	0.91	0.58				0.99
		1	no05d24			25.2			3	1	0.52				0.34
		2	no05d27		0.9	41		1.46	0.52	5.92	1.36				1.41
		3	no05d30			26.2			0.68	0.26			0		0.061
		4	no05d33		0.6	24.2		51	0.65	0.86	0.24			1.81	0.24
		4	no05d34		0.57	22.2				1.54	0		0		0.13

Appendix VI. LA-ICPMS and EPMA spot analysis locations on BSE images for Kiruna and El Laco magnetite

KRN-10-02 map

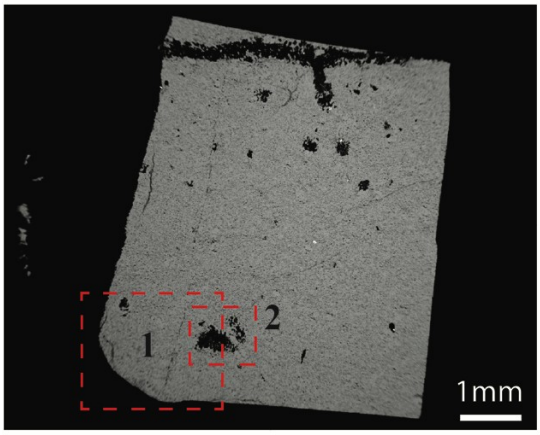

KRN-10-02(1)

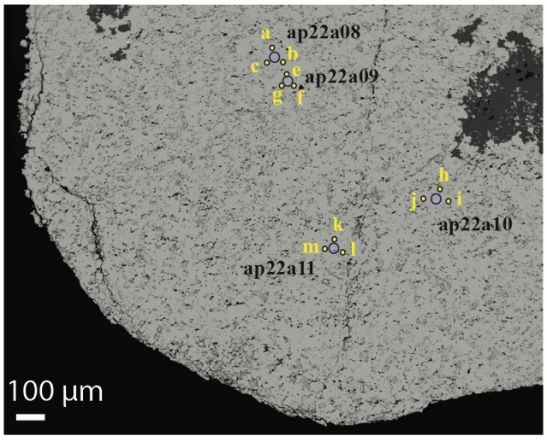

KRN-10-02(2)

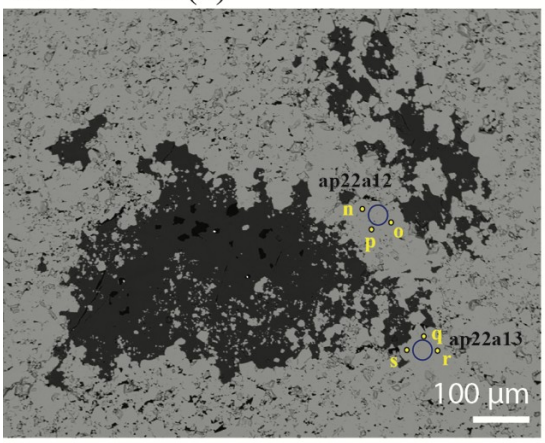

K-1 map

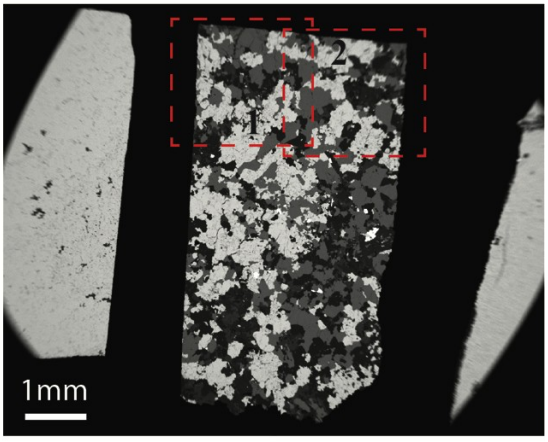

K-1(1)

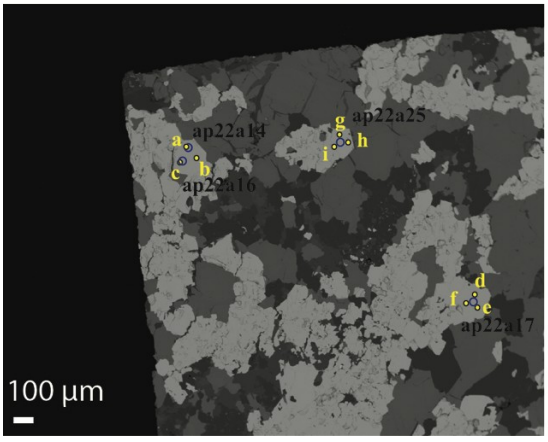

K-1(2)

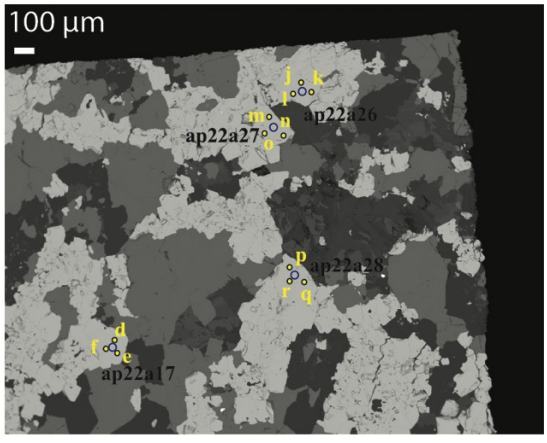

Appendix VI. (Cont.)

K-2 map

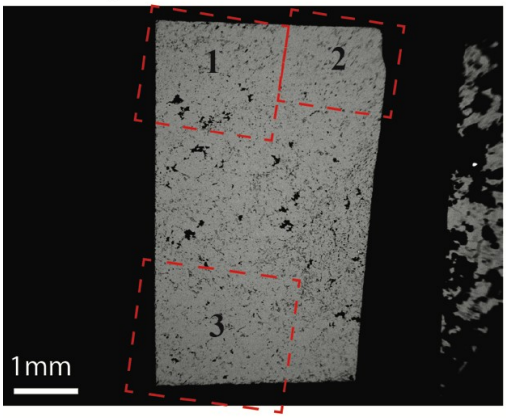

K-2(1)

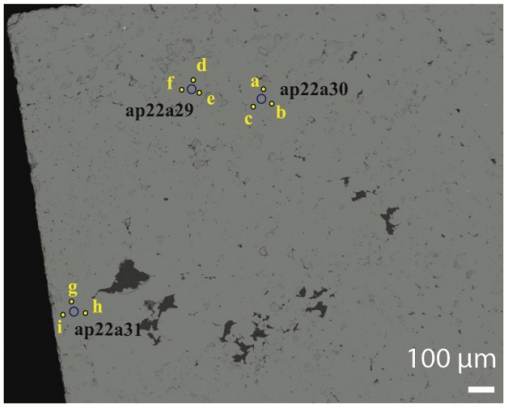

K-2(2)

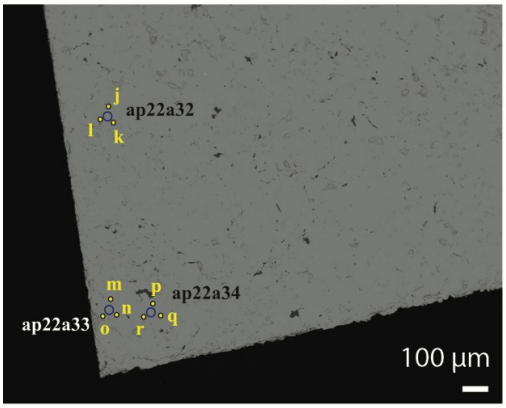

K-2(3)

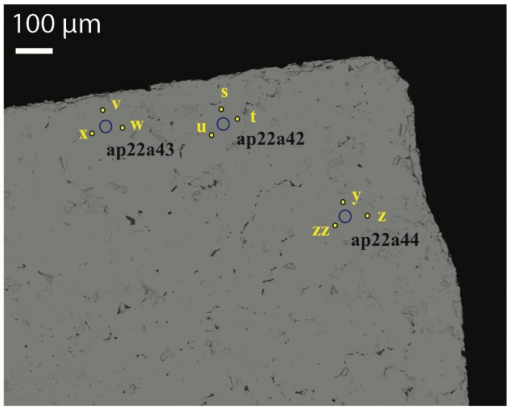

Appendix VI. (Cont.)

KRN-11-01 map

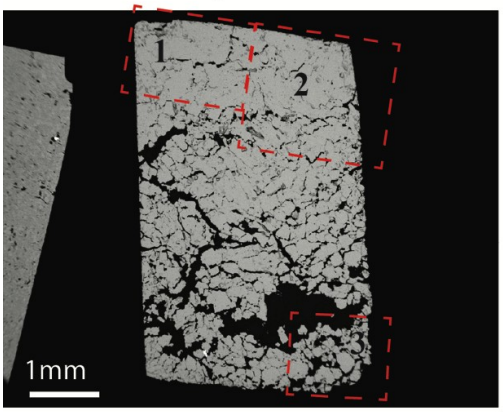

KRN-11-01(1)

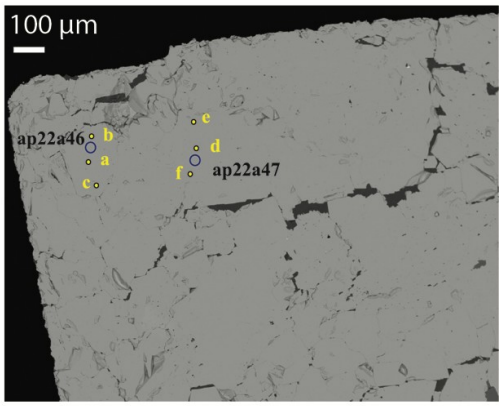

KRN-11-01(2)

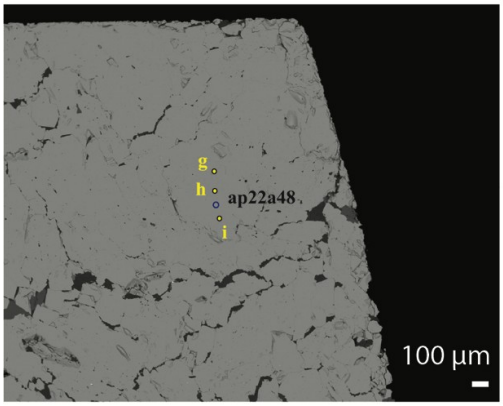

KRN-11-01(3)

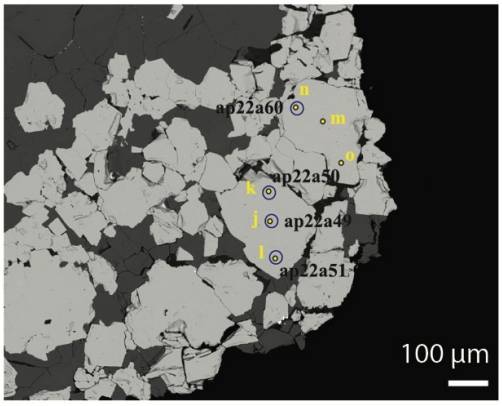

Appendix VI. (Cont.)

KRN-11-03 map

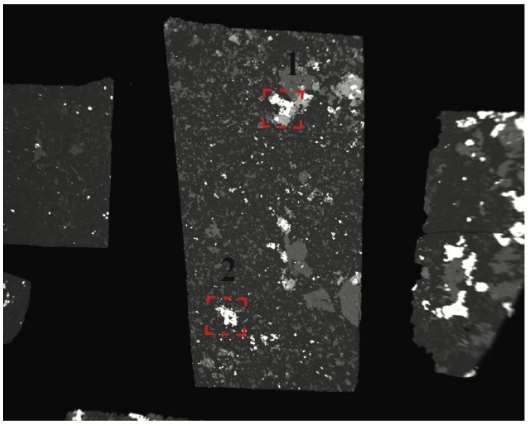

KRN-11-03(1)

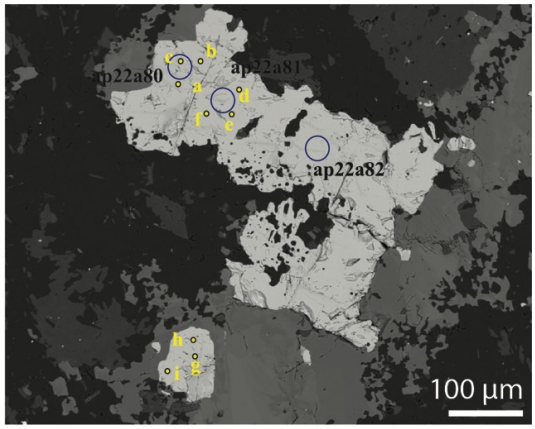

KRN-11-03(2)

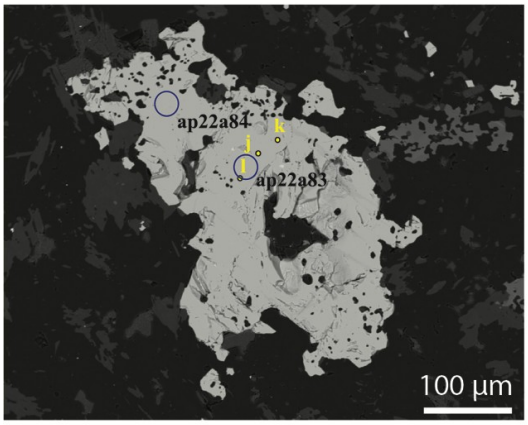

KRN-11-04 map

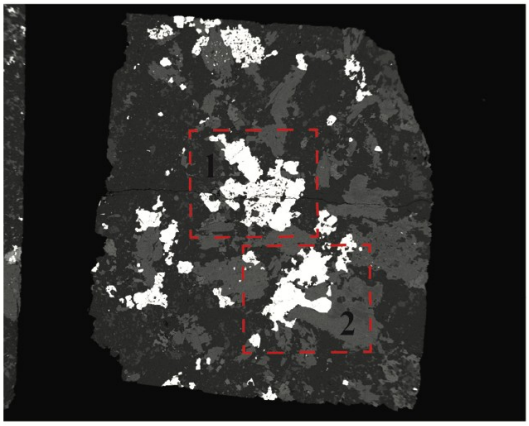

KRN-11-04(1)

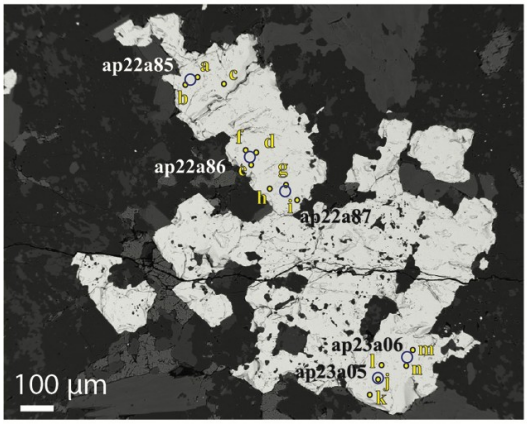

KRN-11-04(2)

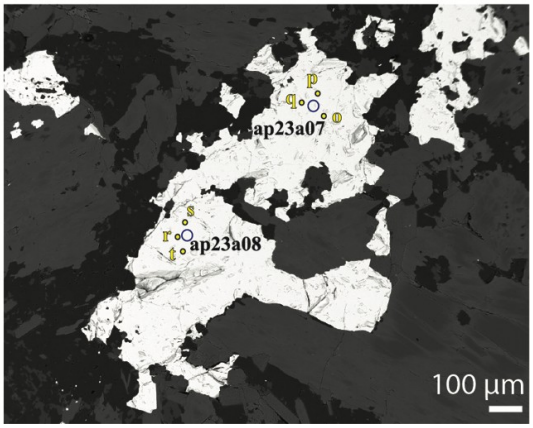

Appendix VI. (Cont.)

KRN-11-05 map

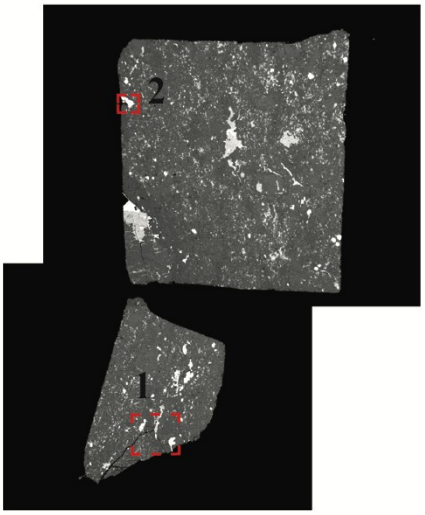

KRN-11-05(1)

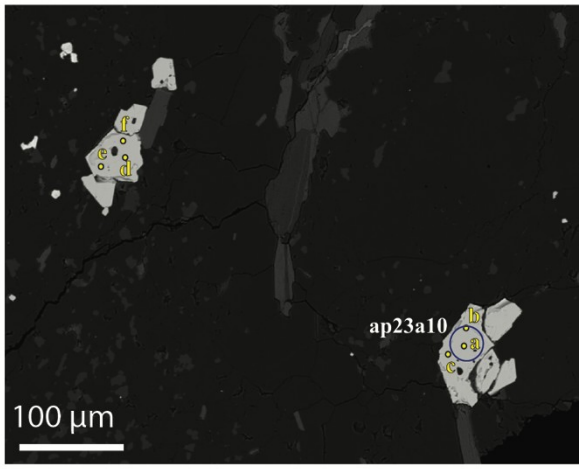

KRN-11-05(2)

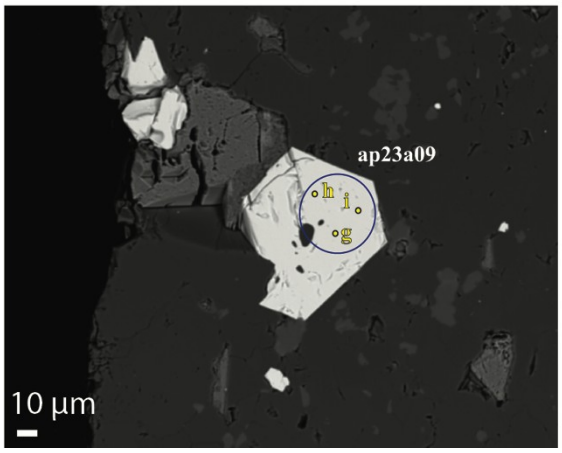

Appendix VI. (Cont.)

KRN-12-02 map

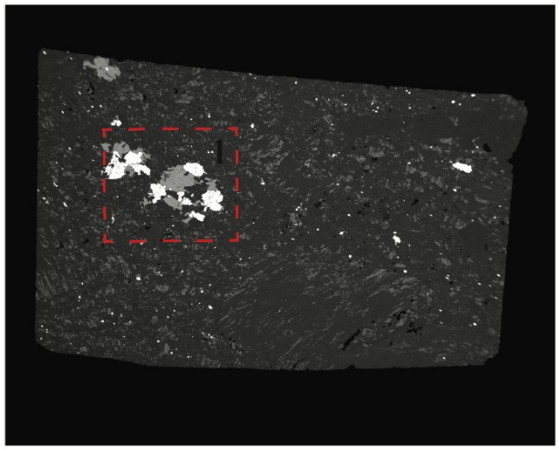

KRN-12-02

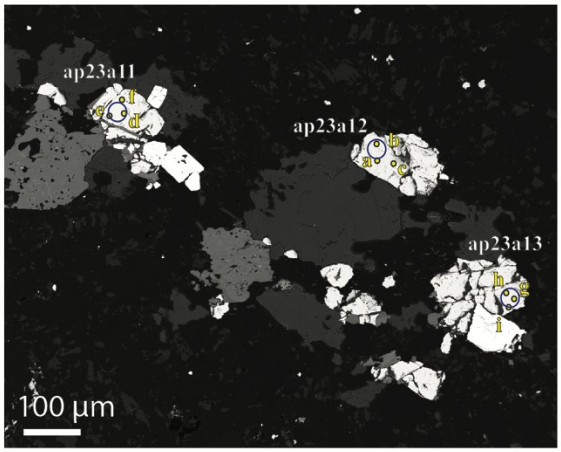

KRN-12-03 map

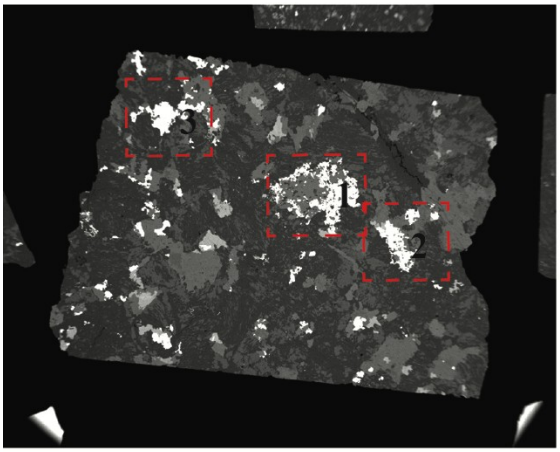

KRN-12-03(1)

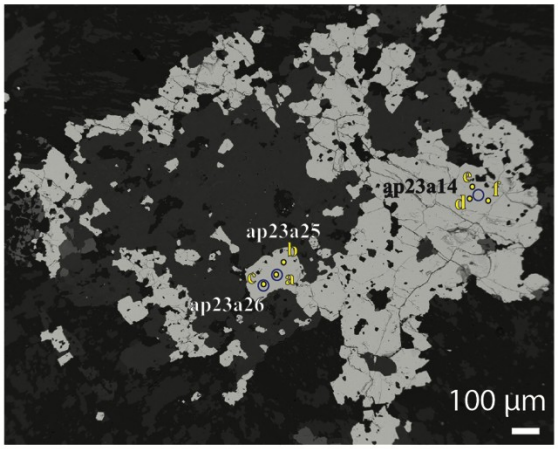

KRN-12-03(2)

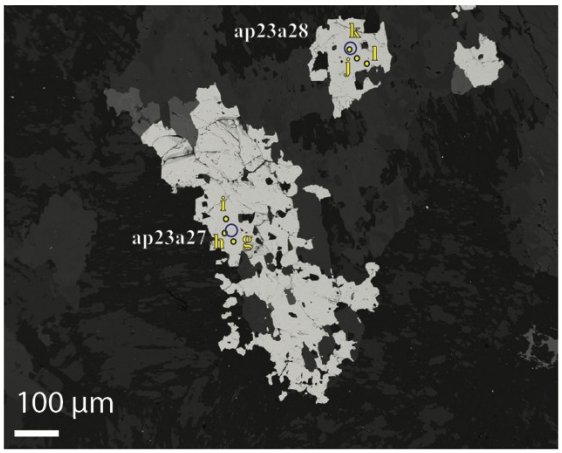

KRN-12-03(3)

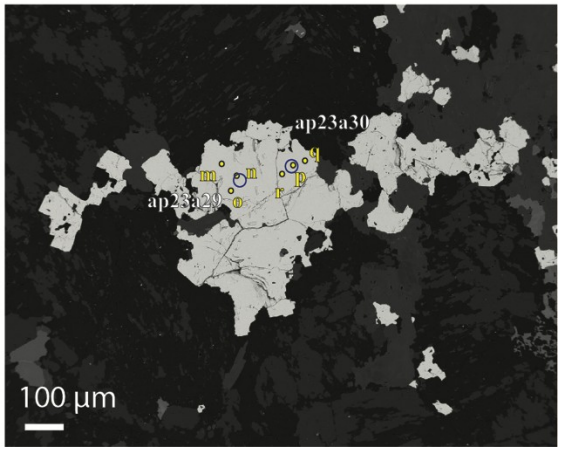

Appendix VI. (Cont.)

KRN-12-05 map

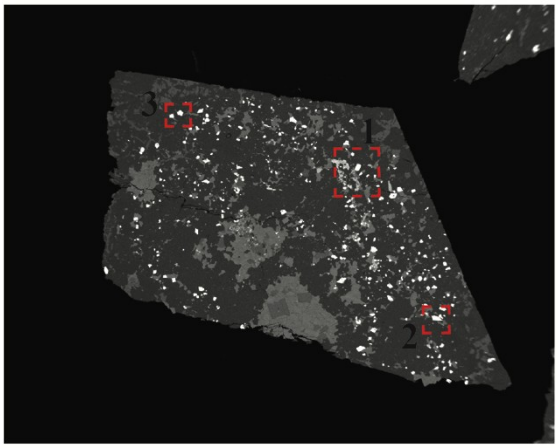

KRN-12-05(1)

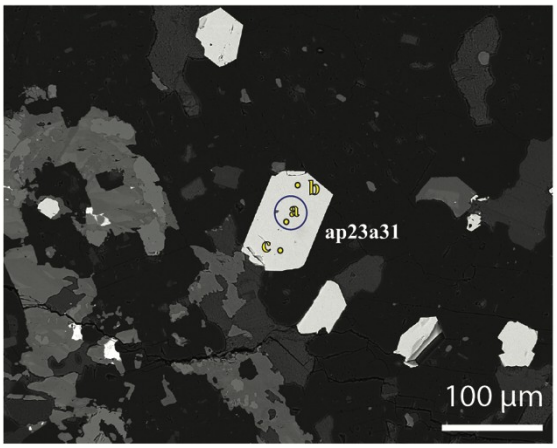

KRN-12-05(2)

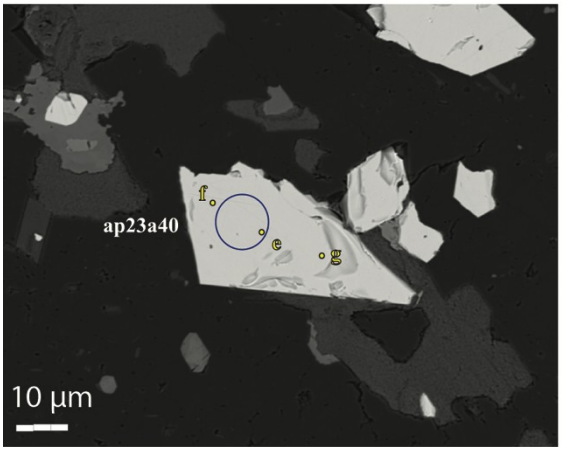

KRN-12-05(3)

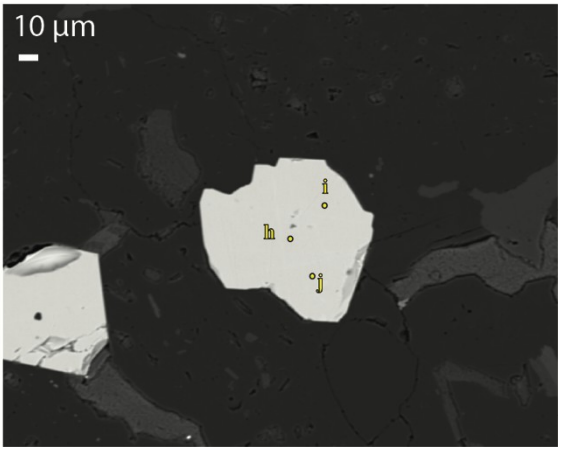

Appendix VI. (Cont.)

TUV-10-03_map(1)

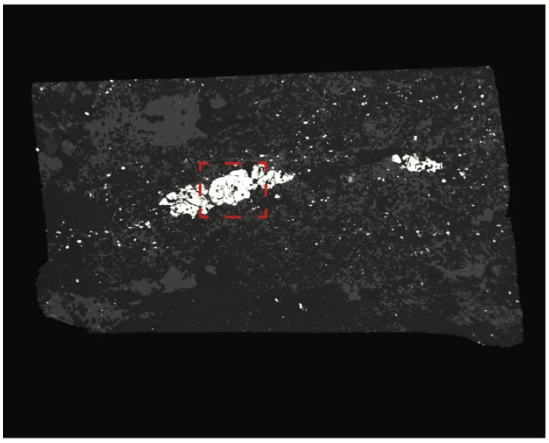

TUV-10-03_map(2)

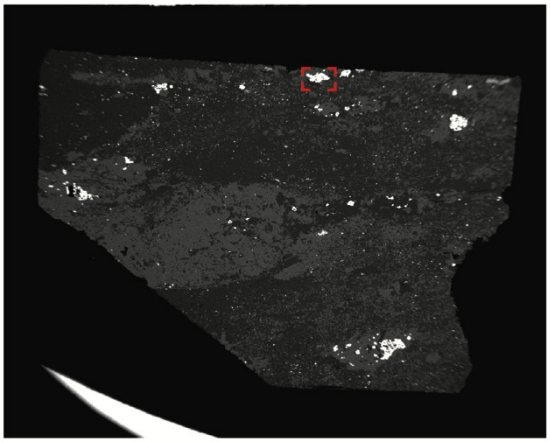

TUV-10-03(1)

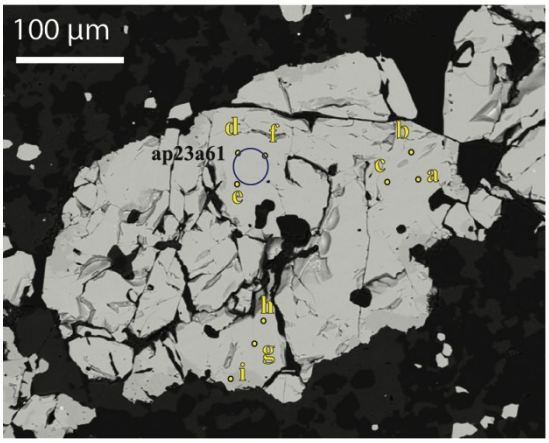

TUV-10-03(2)

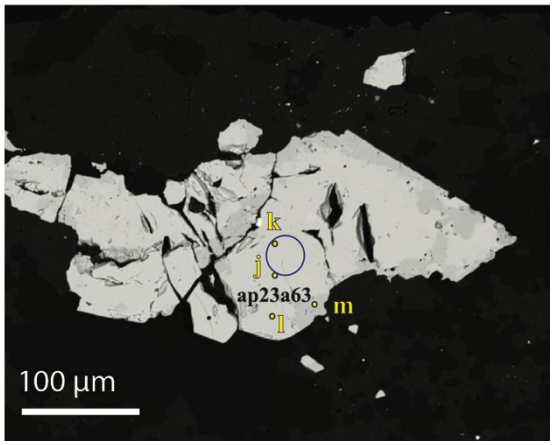

Appendix VI. (Cont.)

TUV-10-01 map

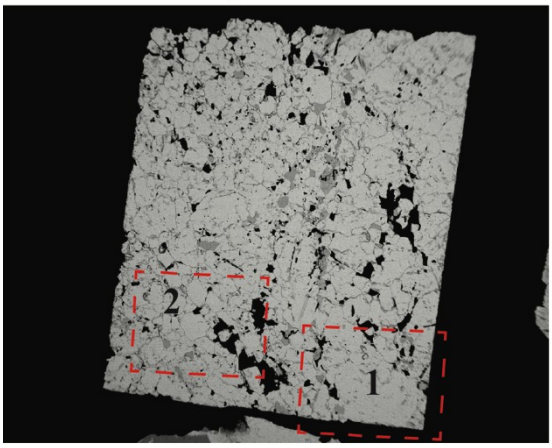

TUV-10-01(1)

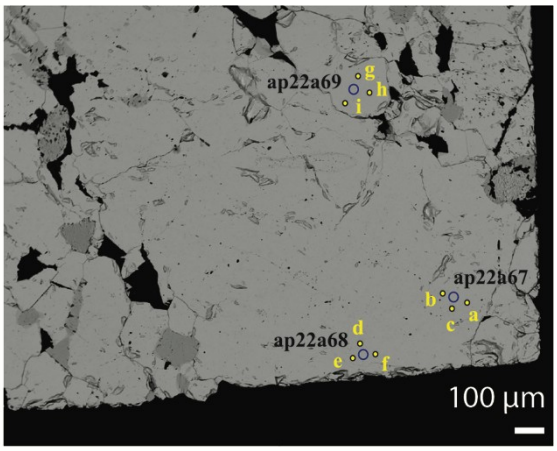

TUV-10-01(2)

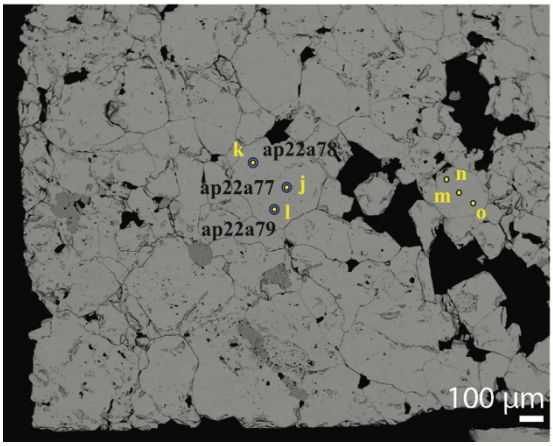

Appendix VI. (Cont.)

NUK-10-03 map

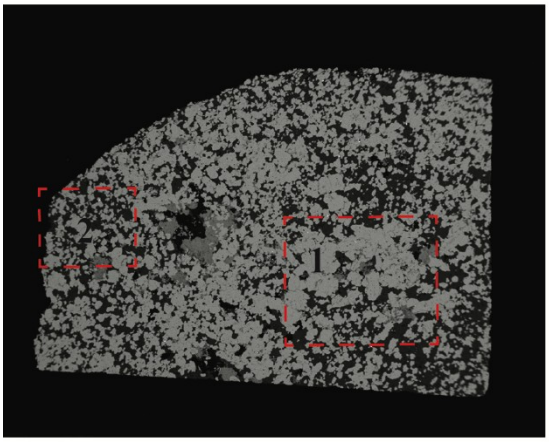

NUK-10-03(1)

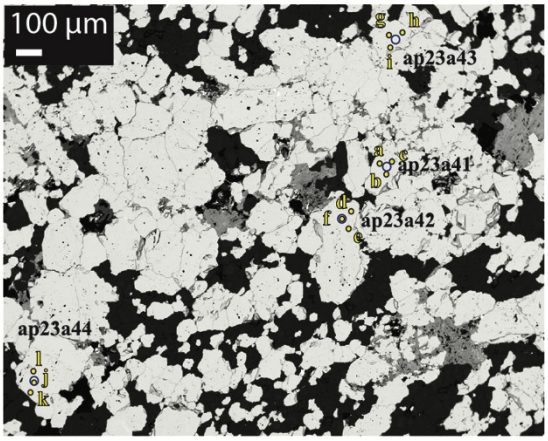

NUK-10-03(3)

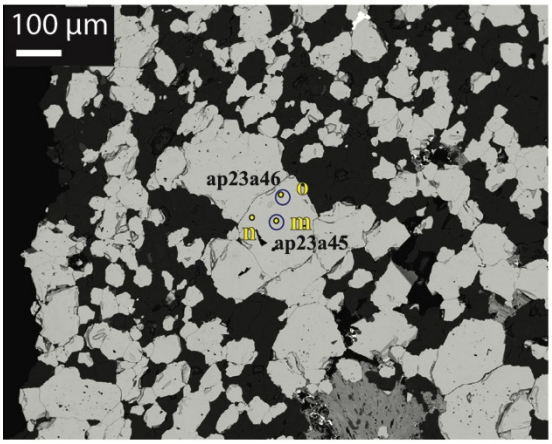

NUK-12-02 map

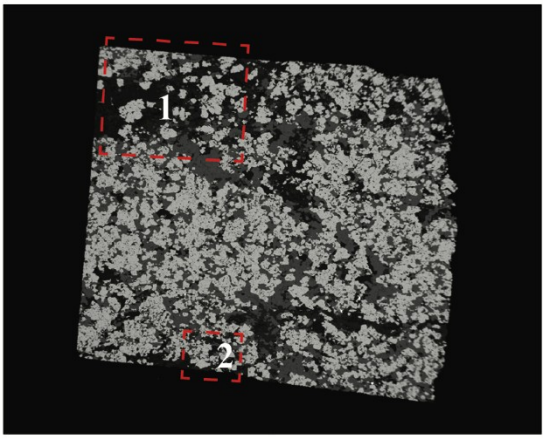

NUK-12-02(1)

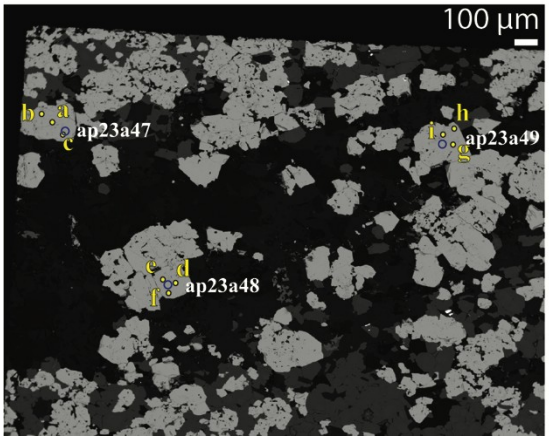

NUK-12-02(2)

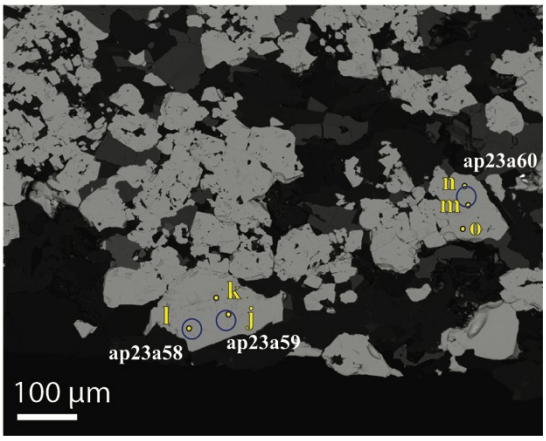

Appendix VI. (Cont.)

REK-10-01 map

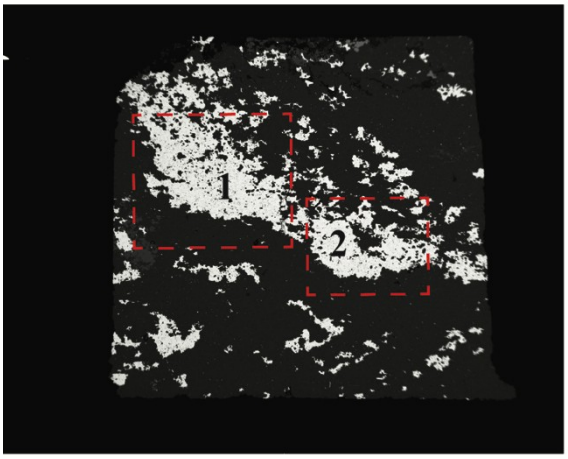

REK-10-01(1)

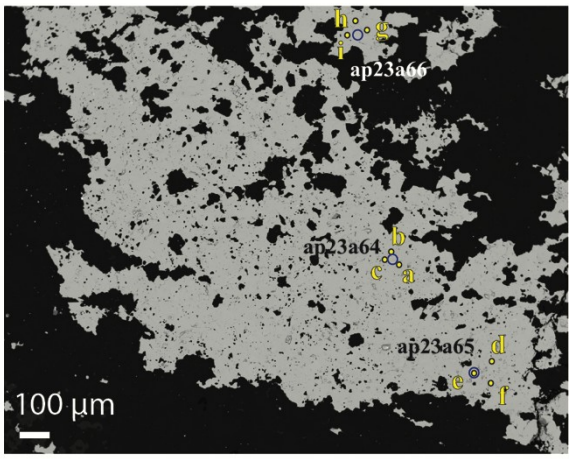

REK-10-01(2)

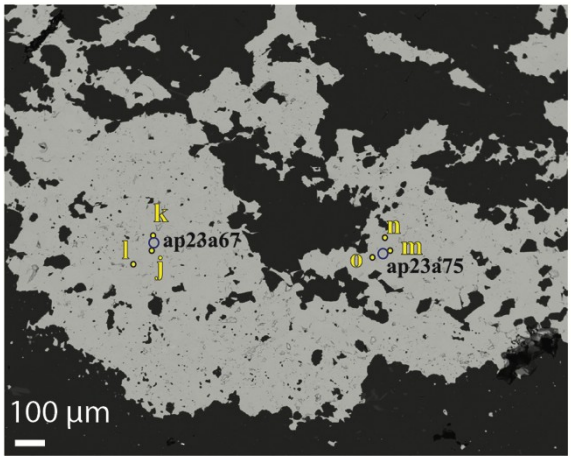

Appendix VI. (Cont.)

REK-10-04 map

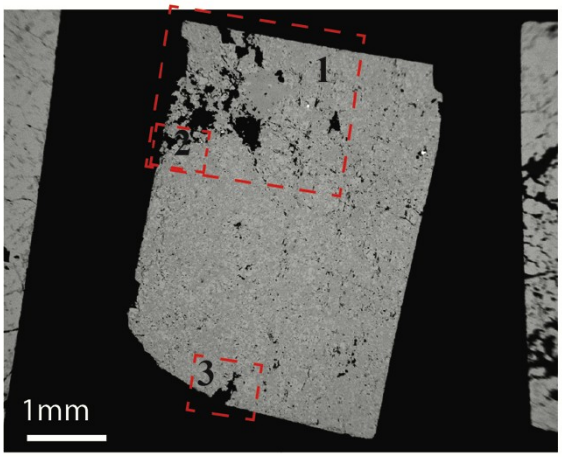

REK-10-04(1)

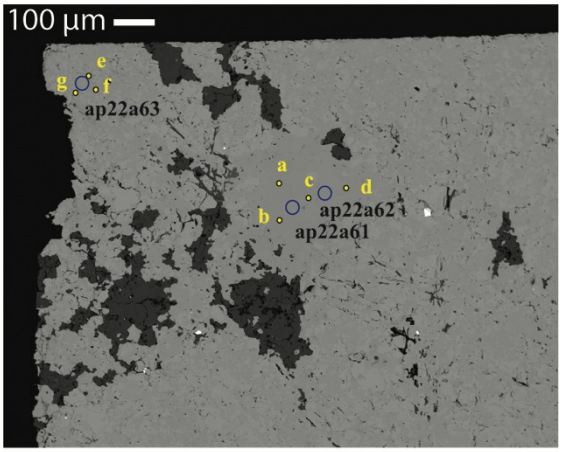

REK-10-04(2)

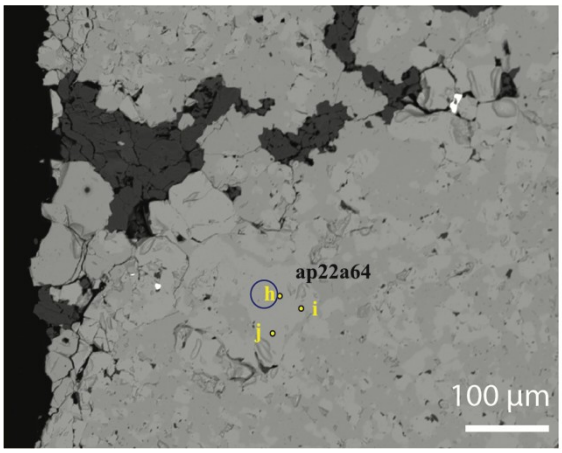

REK-10-04(3)

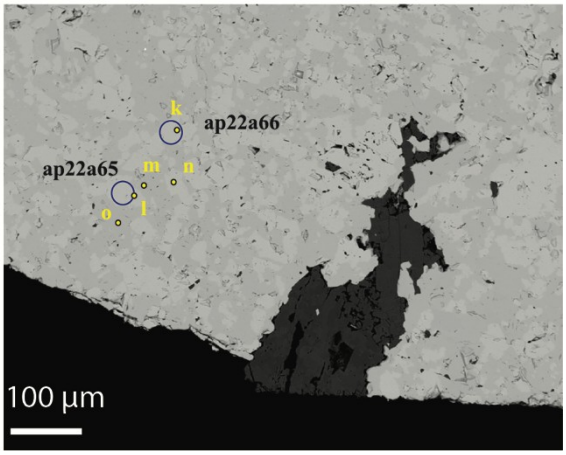

Appendix VI. (Cont.)

REK-12-02 map

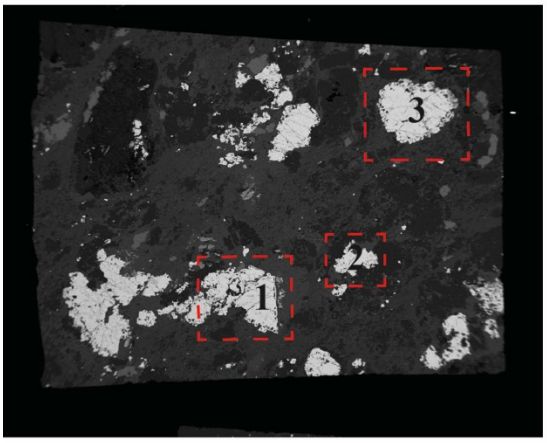

REK-12-02(1)

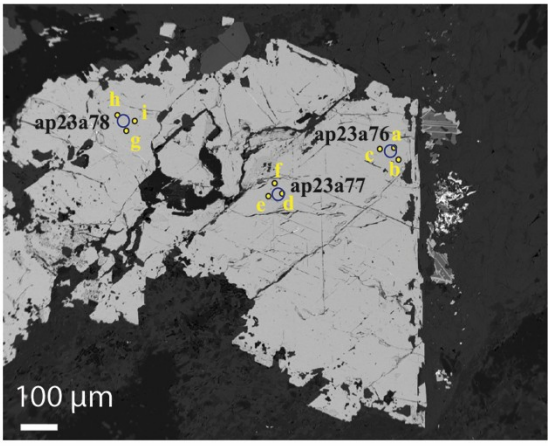

REK-12-02(2)

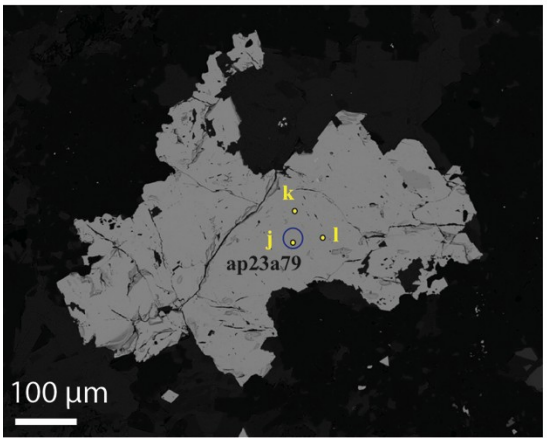

REK-12-02(3)

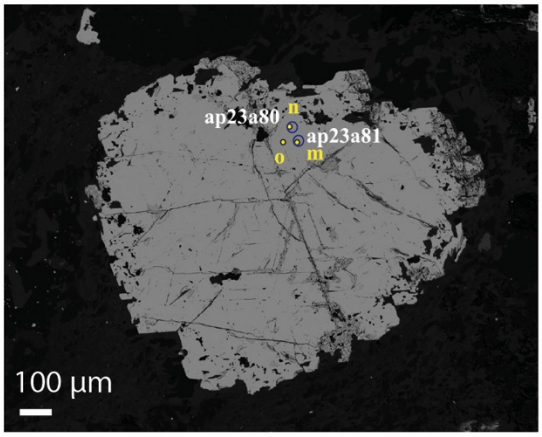

Appendix VI. (Cont.)

ELL-14-02 map

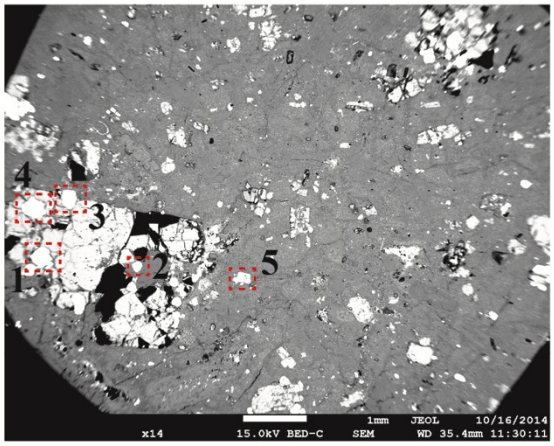

ELL-14-02 (1)

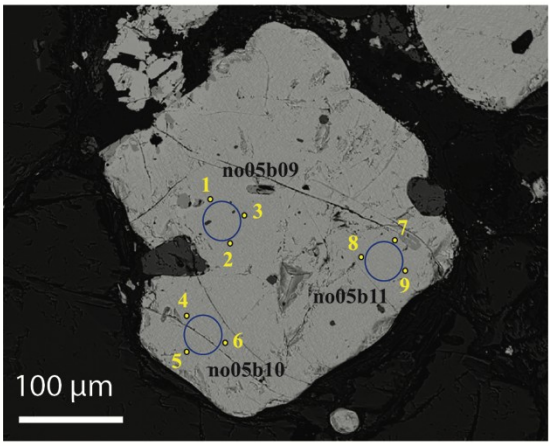

ELL-14-02 (2)

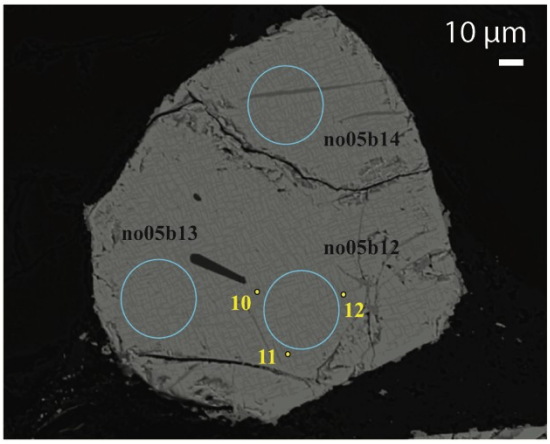

ELL-14-02 (3)

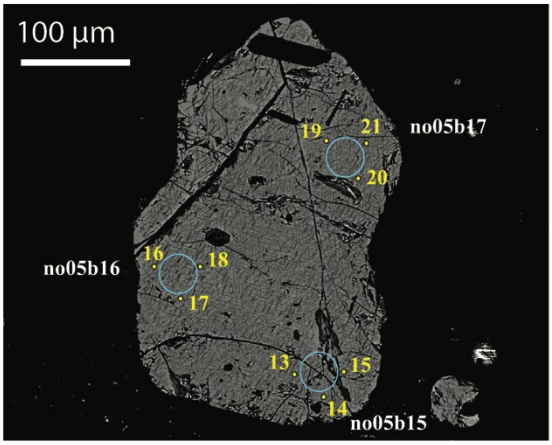

ELL-14-02 (4)

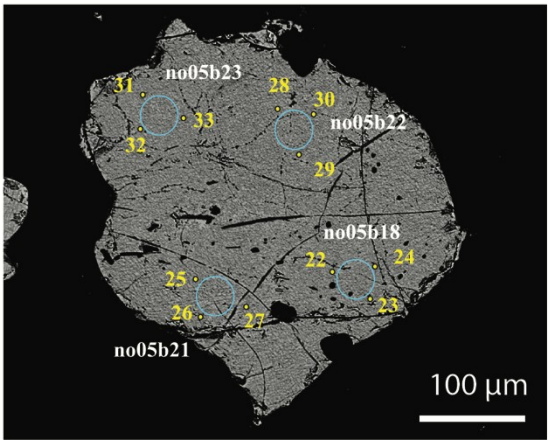

ELL-14-02 (5)

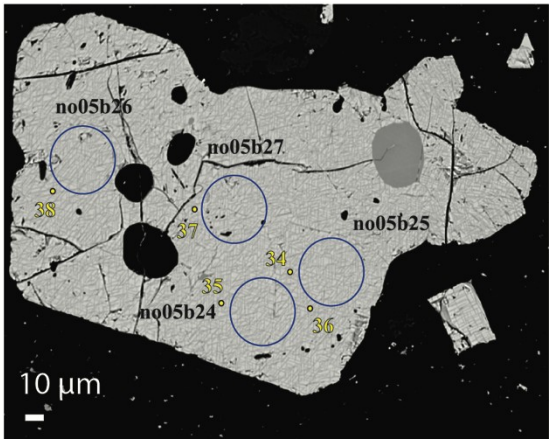

Appendix VI. (Cont.)

ELL-14-04 map

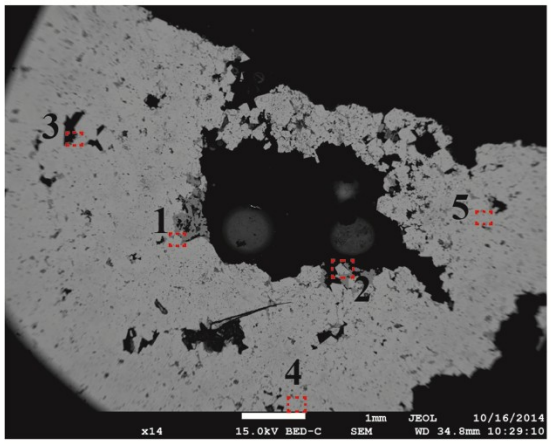

ELL-14-04 (1)

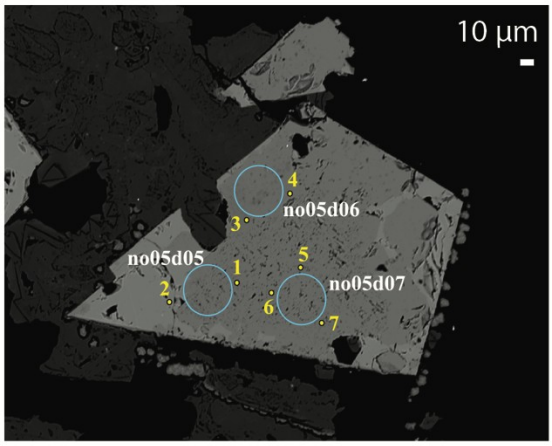

ELL-14-04 (2)

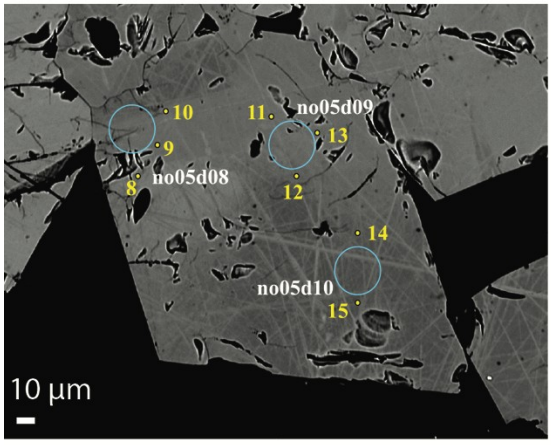

ELL-14-04 (3)

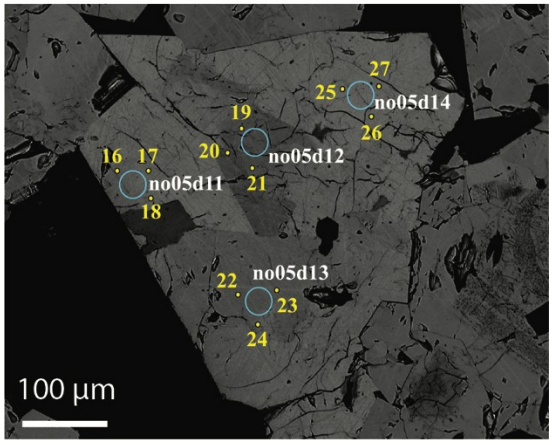

ELL-14-04 (4)

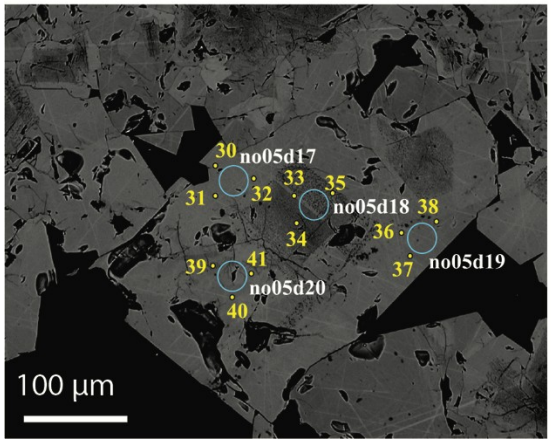

Appendix VI. (Cont.)

ELL-14-05 map

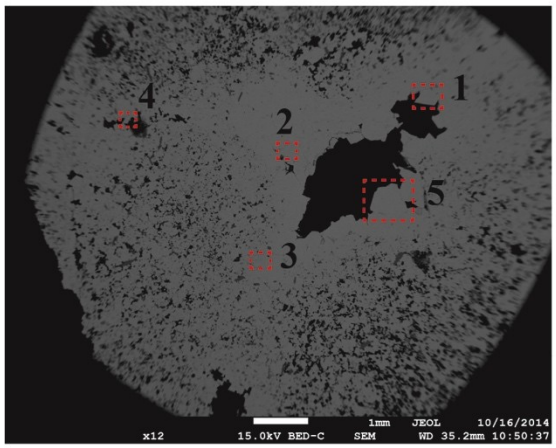

ELL-14-05 (1)

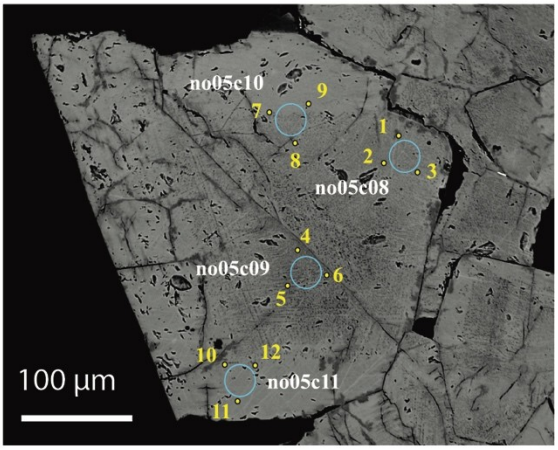

ELL-14-05 (2)

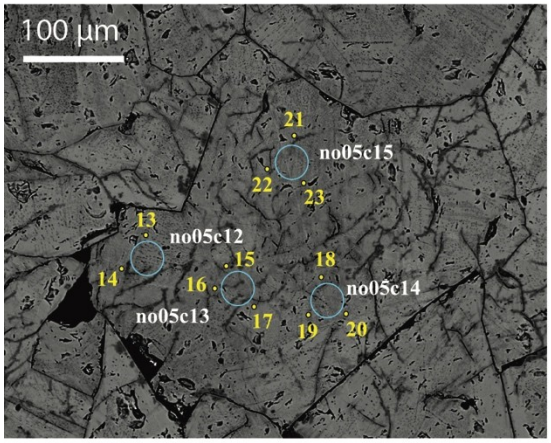

ELL-14-05 (3)

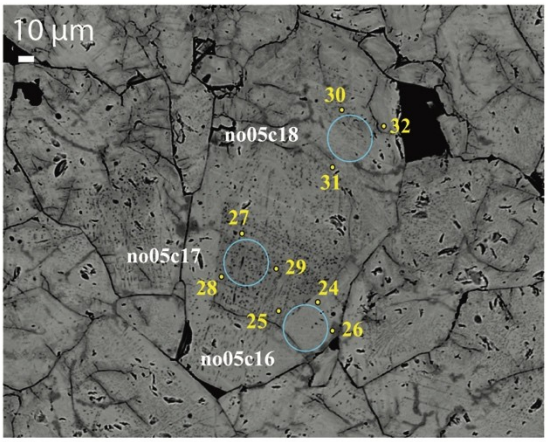

ELL-14-05 (4)

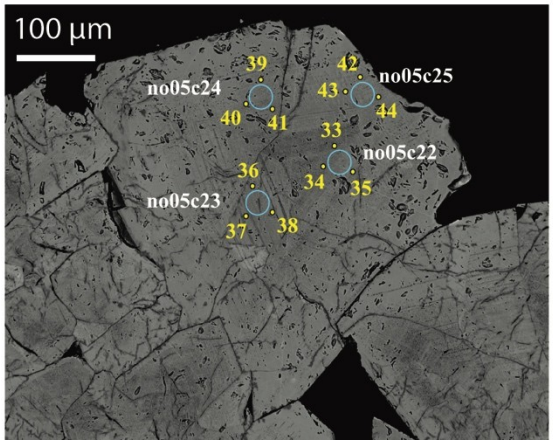

ELL-14-05 (5)

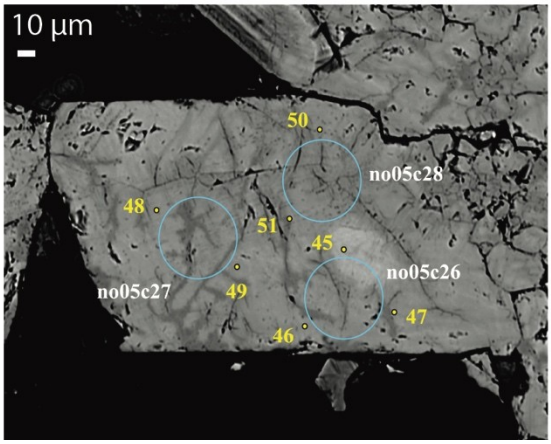

Appendix VI. (Cont.)

ELL-14-06 map

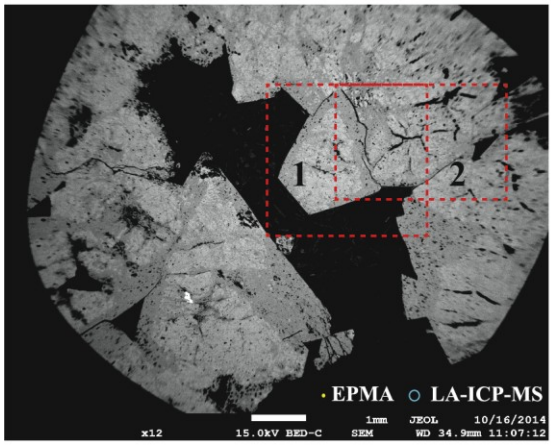

ELL-14-06 (1)

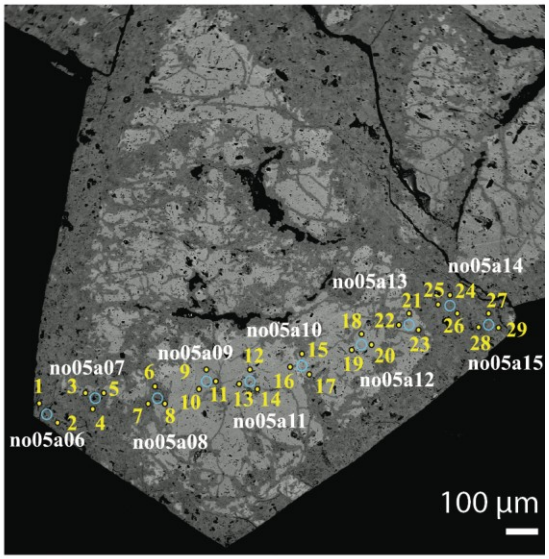

ELL-14-06 (2)

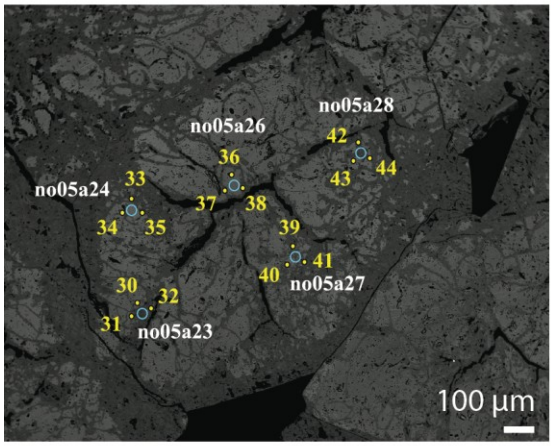

ELL-14-06 (3)

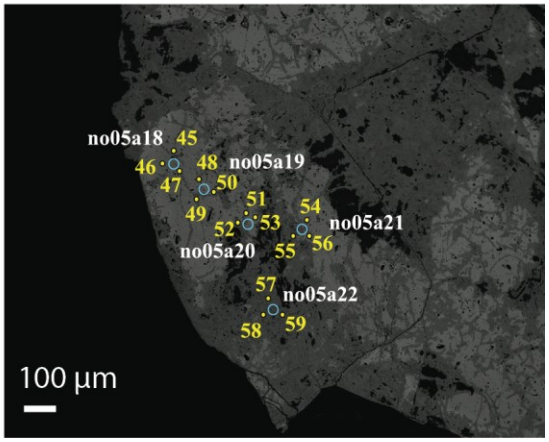

Appendix VI. (Cont.)

LAS-14-07 map

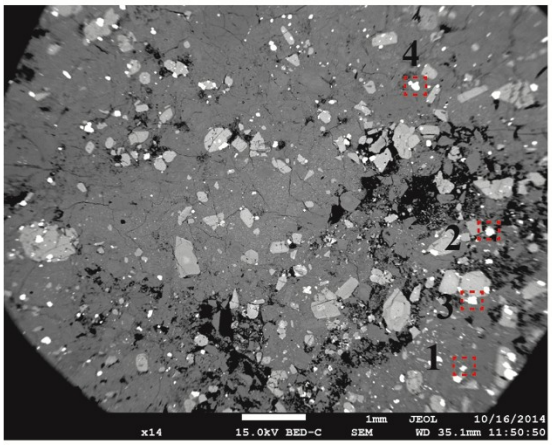

LAS-14-07 (1)

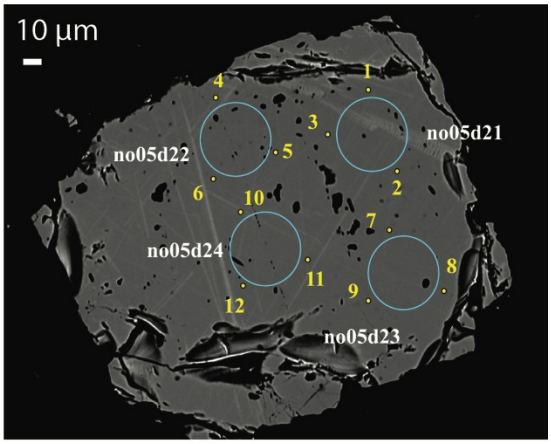

LAS-14-07 (2)

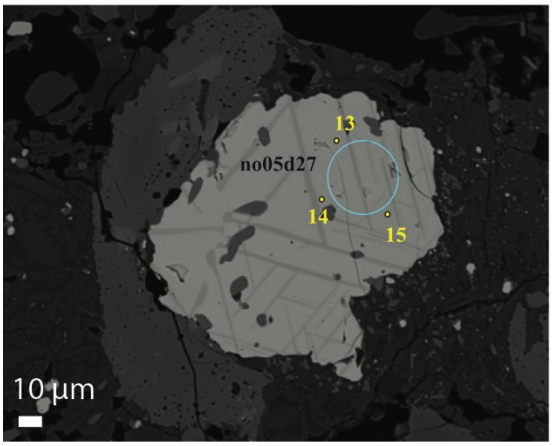

LAS-14-07 (3)

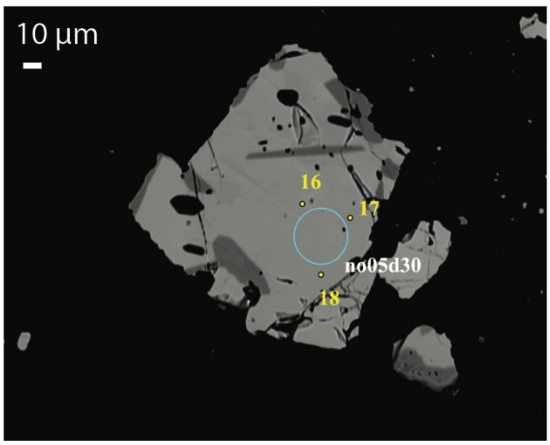

LAS-14-07 (4)

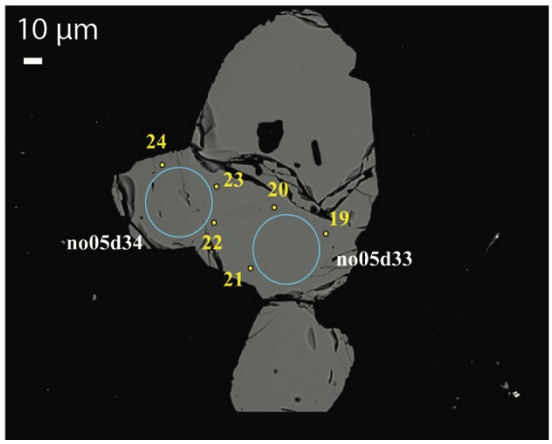

Appendix VII. LA-ICPMS spot analysis results for Mud Tank, Balmat and Bushveld magnetite. Fe (wt%) is the mean concentrations of three or less EPMA analyses in the vicinity of LA-ICPMS spots.

Sample	Rock Type	Fe wt.% (EPMA)	^{24}Mg	^{27}Al	^{29}Si	^{31}P	^{34}S	^{44}Ca	^{47}Ti	^{51}V	^{52}Cr	^{55}Mn	^{59}Co	^{60}Ni	^{63}Cu	^{66}Zn
Mudtank	Carbonatite Mag	68	1017	789	980	47	550		2109	14170	193	276	124	657	4.4	407
		68	966	760	280	35	90		2194	13960	87	289	123	664	11.5	365
		68	1002	699	240	7	100		2213	13890	137	277	121	615	0.21	377
		68	962	716	230	10	450	100	2245	13710	94	276	118	611		358
		68	941	737	230	14	290		2229	13700	71	273	124	655	3.1	397
		68	901	708	1220	19	840		2098	13740	168	260	121	630	1.8	376
		68	907	657	160		640		1789	13450	83	242	119	624		331
		68	915	714	790	8.4	560	40	2017	13730	156	252	118	623		354
		67	1138	672	530	9	420	100	3690	12640	112	426	117	606		408
		68	1162	713	20	4	250	10	4760	13130	45	455	120	617	0.05	406
		67	1136	727	940		250		3662	13170	202	416	125	647		512
		67	1096	688	110	24	210		3310	13240	83	381	122	635		475
		67	1100	724	610	8	520	140	3470	13120	94	401	123	637		551
		68	44.1		340	20	400	220	80	548	123	373	17			25060
Balmat	MVT Zn Vein Mag	69	70		710	19	370	140	65	594	134	350	19			23480
		68	40		240	10	180	140	45	592	57	353	18			24850
		68	47		230	7.9	230		34	638	89	289	17			22820
		69	37		1330	26	830	120	48	593	216	251	17			22570
		69	44		140	2	20		45	635	33	304	18			23700
		69	33		1040	15	860	90	2	288	158	217	16			20980

Appendix VII. (Cont.)

Sample	Rock Type	Fe wt.% (EPMA)	^{24}Mg	^{27}Al	^{29}Si	^{31}P	^{34}S	^{44}Ca	^{47}Ti	^{51}V	^{52}Cr	^{55}Mn	^{59}Co	^{60}Ni	^{63}Cu	^{66}Zn
Balmat	MVT Zn Vein	68	46		820	6	700	200	64	443	84	615	21			27890
	Mag	69	44		310	16	510	70	12	4		435	22			25420
		69	50		80	12	260		54	372	70	549	20			27090
		69	750	91	1920	27	490	190	23	220	267	434	20			22820
		69	44		970	26	350	140	17	280	185	445	19			22480
		69	198		1120	23	280	30	37	289	199	456	20			24240
Bushveld	layered mafic	57	6770	9100	3200	84	1960	290	70000	10530	1458	2381	182	326	99	262
(BC-28)	intrusion Mag	58	5280	9430	200	188	600	130	85900	14280	1670	2690	230	318	477	307
		57	7770	4810	1360	21	1860	220	69100	9760	1498	2395	180	458	72	193
		57	6650	4980	1800	14	2260	320	75600	11730	1660	2540	178	261	89	242
		58	7930	5220		35	1930		74600	11210	1282	2717	394	112	102	268
		57	7230	4920	1660	9	1580	100	73100	10110	1494	2423	105	395	175	214
		57	5050	4500	2170	31	810	30	73100	10430	1396	2362	193	389	101	150
		57	5140	5550	4180	65	1010		73600	11610	1502	2605	166	326	5	287
		58	11020	21140	1250	18	590		64900	8410	1277	1986	290	572		475
		56	10490	20910	120	15	320		63500	8430	1237	1959	286	549		451
		57	10380	19030	390	7	300		66800	8820	1274	2312	307	596	10	425
		58	9870	20030	330	15	180		67390	8680	1355	2318	309	578		460
		57	11050	23320	130	19	230		64700	8600	1312	2182	297	567	0	540
		57	9820	19170	590	20	170	70	66890	8950	1313	2306	290	570	7	443

Appendix VII. (Cont.)

Sample	Rock Type	^{71}Ga	^{75}As	^{88}Sr	^{89}Y	^{93}Nb	^{118}Sn	^{139}La	^{140}Ce	^{141}Pr	^{146}Nd	^{147}Sm	^{153}Eu	^{157}Gd
Mudtank	Carbonatite Mag	28	0.82	0.86	0.14	0.15	7	0.41	1.43	0.04	0.31	0.03	0.07	0.33
		26	0.07	2.40	0.16	0.11	7	0.34	0.55	0.07	0.13	0.01	0.08	0.36
		26	0.16	0.03	0.06	0.01	7	0.07	0.14	0.06	0.01		0.02	0.35
		26		1.10	0.01	0.09	7	0.04	0.11	0.02	0.10	0.02	0.06	0.40
		28	0.05	1.70	0.16	0.31	8	0.47	0.49	0.13	0.11	0.06	0.04	0.56
		26	0.13	0.60	0.11	1.32	8	0.34	0.38	0.05	0.13	0.01	0.02	0.56
		26		0.45	0.03		7	0.10	0.18	0.06	0.03	0.09	0.07	0.52
		27	0.01			0.01	7	0.12	0.07	0.01	0.15	0.10	0.07	0.25
		25	0.12		0.06	0.03	10	0.02	0.04	0.02	0.02	0.02	0.03	0.03
		26	0.00		0.04	0.04	10	0.04	0.02	0.03	0.04	0.01	0.03	
		27	0.42	0.09	0.08	0.03	10	0.04	0.00	0.02	0.01	0.02	0.05	0.22
		27	0.24	0.09	0.02	0.02	9	0.01	0.06	0.02	0.05	0.02	0.03	
		27				0.03	9		0.01	0.02	0.03		0.03	
Balmat	MVT Zn Vein	47	0.26	0.08	0.02	0.09	64	0.04	0.01		0.03	0.03	0.03	0.08
	Mag	47	2.28	0.20	0.02	0.05	61	0.08	0.02	0.02	0.05		0.01	0.16
		46	0.07	0.04	0.09	0.03	65	0.07	0.04	0.05	0.18	0.01	0.02	0.08
		35	0.60	0.05	0.04	0.02	71	0.08	0.06	0.01	0.09	0.03	0.03	0.35
		36	0.51	0.13	0.06	0.05	70	0.07	0.00	0.03	0.15	0.01	0.02	0.35
		34	0.62		0.05	0.08	71	0.06	0.00	0.03		0.01	0.03	0.54
		32	1.11	0.02	0.02	0.09	46	0.05	0.01	0.00	0.03	0.47	0.03	0.27

Appendix VII. (Cont.)

Sample	Rock Type	^{71}Ga	^{75}As	^{88}Sr	^{89}Y	^{93}Nb	^{118}Sn	^{139}La	^{140}Ce	^{141}Pr	^{146}Nd	^{147}Sm	^{153}Eu	^{157}Gd
Balmat	MVT Zn Vein Mag	31	3.33		0.06	0.05	63	0.03	0.07	0.02	0.01	0.00	0.08	
		19	0.59		0.08	0.05	7	0.05	0.03	0.07	0.02		0.02	
		36	0.12	0.90	0.03	0.02	53	0.02	0.02	0.04	0.09		0.08	
		53	3.16	0.41		0.05	46	0.06	0.03	0.01		0.05	0.02	
		44	0.43	0.16		0.03	48	0.02	0.02	0.05	0.07		0.04	
		49	3.78			0.04	51		0.02	0.06	0.00	0.01	0.02	
Bushveld (BC-28)	layered mafic intrusion Mag	52	0.09	2.93	0.17	1.29	2	0.20	0.12	0.09			0.02	0.33
		68		6.00	0.17	2.37	2	0.22	0.27	0.07			0.17	1.80
		54		1.09	0.02	1.30	1	0.07	0.03	0.01		0.02	0.03	0.44
		66		2.16	0.02	1.69	2	0.09	0.20	0.04	0.05	0.06	0.07	0.77
		66		3.23		1.39	1	0.16	0.08	0.07	0.03	0.11	0.09	0.40
		65		1.93	0.04	1.33	1	0.00	0.04	0.09	0.01	0.01	0.08	0.28
		51	0.21	1.19	0.02	1.52	2	0.05	0.05	0.02	0.03	0.13	0.02	0.04
		67		2.93	0.11	1.47	2	0.16	0.27	0.04	0.23		0.03	1.07
		47	0.25	1.40	0.08	1.05	2	0.02	0.01	0.04	0.07	0.01	0.02	
		47	0.15	3.60	0.03	1.01	2	0.36	0.12	0.06	0.02	0.02	0.04	
		48	0.11	0.37	0.07	0.92	2	0.08	0.04	0.04	0.09	0.02	0.03	
		48	0.07		0.05	0.85	2	0.06	0.05	0.08	0.32		0.02	0.12
		50	0.01	1.30	0.02	1.01	2	0.11	0.01	0.06	0.15	0.01	0.09	0.25
		49		4.20	0.02	1.00	2	0.08	0.06	0.06	0.03	0.01	0.01	0.28

Appendix VII. (Cont.)

Sample	Rock Type	^{159}Tb	^{163}Dy	^{165}Ho	^{166}Er	^{169}Tm	^{172}Yb	^{175}Lu	^{178}Hf	^{181}Ta	^{197}Au	^{205}Tl	^{208}Pb	^{232}Th	^{238}U
Mudtank	Carbonatite Mag	0.02	0.00	0.00	0.00	0.00	0.00			0.01		0.01	0.71	0.06	0.04
		0.00	0.04	0.00	0.01	0.01		0.02		0.02		0.00	0.56	0.05	0.05
		0.00	0.01	0.00	0.01	0.03	0.01		0.01	0.01	0.05	0.01	0.06	0.11	
		0.00	0.04	0.00	0.00	0.01	0.00	0.01	0.01	0.00	0.02	0.01	0.11	0.12	0.00
		0.02	0.01	0.00	0.01	0.00	0.03	0.00	0.02	0.03	0.02		0.50	0.00	0.07
		0.01	0.00	0.00	0.00	0.01	0.03	0.02	0.00	0.07			0.39	0.33	0.11
		0.00	0.01	0.00		0.01	0.01	0.01	0.01	0.00		0.01	0.06		
		0.03	0.00	0.00	0.00	0.01	0.00	0.01	0.00	0.02		0.01	0.09	0.02	
		0.00		0.00	0.01	0.00	0.01	0.01	0.01	0.01	0.10		0.04		0.01
		0.03	0.00	0.00	0.01	0.01		0.01	0.02	0.01		0.00	0.03		
		0.05	0.01	0.00	0.02	0.01	0.02	0.01		0.02		0.00	0.05		
		0.02	0.01	0.01	0.01	0.01	0.02	0.01	0.01	0.03		0.00	0.03	0.01	
		0.01			0.00	0.02	0.01	0.01	0.00	0.04		0.00	0.04	0.00	0.00
Balmat	MVT Zn Vein	0.00	0.01	0.00		0.00		0.00	0.00	0.02			0.09	0.01	0.00
	Mag	0.02	0.01			0.01		0.00	0.01	0.01	0.02	0.01	0.91	0.01	
		0.03	0.00	0.00		0.01	0.01	0.00		0.01		0.00	0.06	0.26	
		0.02	0.02	0.00		0.01	0.00	0.00	0.00	0.02			0.25	0.02	0.00
		0.01	0.01	0.00				0.01	0.00	0.01			0.09		
		0.01	0.01		0.08		0.03			0.02	0.06		0.05	0.00	
		0.01	0.01	0.01	0.00	0.00	0.03	0.01	0.01	0.02		0.00	0.20	0.01	

Appendix VII. (Cont.)

Sample	Rock Type	^{159}Tb	^{163}Dy	^{165}Ho	^{166}Er	^{169}Tm	^{172}Yb	^{175}Lu	^{178}Hf	^{181}Ta	^{197}Au	^{205}Tl	^{208}Pb	^{232}Th	^{238}U
Balmat	MVT Zn Vein	0.01	0.03	0.00	0.00	0.00	0.00	0.01		0.01	0.02	0.02	0.83		
	Mag	0.03		0.00	0.01	0.02	0.00	0.00	0.01	0.01		0.01	0.05		
		0.01	0.02	0.00	0.00	0.01		0.01	0.00	0.01			0.03	0.00	0.00
		0.02	0.00	0.00		0.01	0.01	0.01		0.02	0.02	0.01	0.46	0.02	0.00
		0.02	0.01	0.02	0.00	0.01	0.01	0.00		0.01			0.05	0.01	0.00
		0.01		0.00	0.01	0.00	0.02	0.01	0.00	0.02		0.00	0.63	0.00	0.02
Bushveld	layered mafic			0.00			0.01		0.03	0.04	0.28	0.08	0.91		
(BC-28)	intrusion Mag	0.01		0.01	0.02	0.02	0.05	0.12	0.18	0.18	0.33	0.02	1.68		
				0.01		0.01	0.01		0.14	0.15		0.01	0.32		
		0.05		0.00	0.07	0.01			0.15	0.11	0.23	0.01	1.53		
		0.02	0.05	0.03		0.00	0.07	0.04	0.08	0.09		0.02	0.51		0.01
		0.01	0.01	0.00		0.01	0.03	0.01	0.32	0.09			0.37		0.00
			0.02	0.00		0.02	0.02	0.01	0.14	0.11			0.45		
		0.03	0.03	0.02		0.06	0.02	0.02	0.05	0.06		0.01	1.17		
		0.01	0.01	0.01	0.02	0.01		0.01	0.47	0.08		0.00	0.04	0.04	0.21
		0.02	0.02	0.00		0.02	0.03	0.02	0.61	0.05			0.07	0.03	0.02
		0.01	0.02	0.00	0.00	0.00	0.06	0.01	0.47	0.09			0.06	0.18	0.00
		0.02	0.02	0.00	0.01	0.01		0.01	0.63	0.07			0.02	0.00	0.00
		0.02	0.01	0.01		0.00	0.04	0.02	0.41	0.08		0.00	0.07	0.02	0.01
		0.00	0.04	0.02	0.01	0.01	0.01	0.01	0.53	0.05			0.10	0.05	

Appendix VIII. LA-ICPMS spot analysis results (ppm) for BCR-2G glass during the Kiruna and El Laco analyses.

Element	Kiruna	El Laco	MUN Long term	Element	Kiruna	El Laco	MUN Long term
^{24}Mg	19662	22984	17318	^{140}Ce	47.3		51.2
^{29}Si	2.55E+05	2.89E+05	2.54E+05	^{141}Pr	5.73		6.44
^{31}P	1175	1316	643.99	^{146}Nd	24.9		27.8
^{44}Ca	45972	54324	42317	^{147}Sm	5.75		6.30
^{47}Ti	12021	13740	35.58	^{153}Eu	1.79		1.87
^{51}V	405	457	15714	^{157}Gd	5.78		6.24
^{52}Cr	32.2	21.7	408	^{159}Tb	0.90		0.94
^{55}Mn	1586	1815		^{163}Dy	5.43		6.10
^{59}Co	37.1	42.3	1825	^{165}Ho	1.13		1.23
^{60}Ni	5.88	18.5	36.0	^{166}Er	2.99		3.43
^{63}Cu	17.1	19.3	12.0	^{169}Tm	0.44		0.49
^{66}Zn	131	153	26.0	^{172}Yb	2.85		3.38
^{75}As	1.10	1.06	156	^{175}Lu	0.43		0.48
^{88}Sr	304	360		^{178}Hf	4.35		4.57
^{89}Y	28.8	35.4	326	^{181}Ta	0.67	0.76	0.76
^{93}Nb	9.98	11.8	32.3	^{197}Au	0.58		
^{118}Sn	2.02	2.00	12.0	^{208}Pb	9.94	10.9	11.4
^{138}Ba		694		^{232}Th	5.31	6.39	5.80
^{139}La	23.2		24.6	^{238}U	1.65		1.62